UNIVERSIDADE FEDERAL DE SANTA CATARINA
CENTRO TECNOLÓGICO DE JOINVILLE
PROGRAMA DE PÓS-GRADUAÇÃO EM ENGENHARIA E CIÊNCIAS MECÂNICAS

Vanessa Batista

NUMERICAL ANALYSIS ON THERMAL HYDRAULIC PERFORMANCE OF A COMPACT HEAT EXCHANGER MANUFACTURED BY ADDITIVE MANUFACTURING

Joinville
2023

Vanessa Batista

NUMERICAL ANALYSIS ON THERMAL HYDRAULIC PERFORMANCE OF A COMPACT HEAT EXCHANGER MANUFACTURED BY ADDITIVE MANUFACTURING

Dissertação submetida ao Programa de Pós-Graduação em Engenharia e Ciências Mecânicas da Universidade Federal de Santa Catarina para a obtenção do título de Mestre em Engenharia e Ciências Mecânicas.

Orientadora: Profa. Talita Sauter Possamai, Dra.

Joinville

2023

Ficha de identificação da obra elaborada pelo autor,
através do Programa de Geração Automática da Biblioteca Universitária da UFSC.

Batista, Vanessa
Numerical analysis on thermal hydraulic performance of a compact heat exchanger manufactured by additive manufacturing / Vanessa Batista ; orientadora, Talita Sauter Possamai, 2023.
123 p.

Dissertação (mestrado) - Universidade Federal de Santa Catarina, Campus Joinville, Programa de Pós-Graduação em Engenharia e Ciências Mecânicas, Joinville, 2023.

Inclui referências.

1. Engenharia e Ciências Mecânicas. 2. CFD. 3. Trocador de calor. 4. Desempenho termo hidráulico. I. Sauter Possamai, Talita. II. Universidade Federal de Santa Catarina. Programa de Pós-Graduação em Engenharia e Ciências Mecânicas. III. Título.

Vanessa Batista

Numerical analysis on thermal hydraulic performance of a compact heat exchanger manufactured by additive manufacturing

O presente trabalho em nível de Mestrado foi avaliado e aprovado, em 09 de fevereiro de 2023, pela banca examinadora composta pelos seguintes membros:

Prof. Kleber Vieira de Paiva, Dr.
Universidade Federal de Santa Catarina

Prof. Paulo Sergio Berving Zdanski, Dr.
Universidade do Estado de Santa Catarina

Prof. Roberto Wolf Francisco Junior, Dr.
Universidade do Estado de Santa Catarina

Certificamos que esta é a **versão original e final** do trabalho de conclusão que foi julgado adequado para obtenção do título de mestre em Engenharia e Ciências Mecânicas.

ICP-Edu
Documento assinado digitalmente
Wagner Mauricio Pachekoski
Data: 04/04/2023 15:30:55-0300
CPF: ***.494.569-**
Verifique as assinaturas em https://v.ufsc.br

Prof. Wagner Maurício Pachekoski, Dr.
Coordenação do Programa de Pós-Graduação

ICP-Edu
Documento assinado digitalmente
Talita Sauter Possamai
Data: 04/04/2023 08:25:27-0300
CPF: ***.039.319-**
Verifique as assinaturas em https://v.ufsc.br

Profa. Talita Sauter Possamai, Dra.
Orientadora

Joinville, 2023.

AGRADECIMENTOS

A todos que colaboraram direta ou indiretamente no desenvolvimento deste trabalho.

A Universidade Federal de Santa Catarina (UFSC), Fundação de Estudos e Engenharia de Santa Catarina (FEESC) e PETROBRAS pelos recursos concedidos e apoio à pesquisa.

A professora Dra. Talita Sauter Possamai por sua paciência, dedicação e valiosa orientação.

Ao professor Dr. Renato Oba pelo conhecimento e contribuições ao trabalho.

Aos amigos que fiz no laboratório, Bruna, Damylle e Rodrigo, pela colaboração e amparo.

E, em especial, a minha família e amigos pelo incentivo e apoio incondicional durante todo o processo.

RESUMO

Permutadores de calor são amplamente utilizados em aplicações industriais e domésticas. Um tipo bastante empregado em plataformas *offshore* são os trocadores de calor compactos (CHE), devido à sua alta eficiência térmica, condições de operação elevadas e alta densidade de área. A constante busca por métodos de aprimoramento para a transferência de calor culminou no desenvolvimento de novos tipos de CHEs, como o trocador de calor de circuito impresso (PCHE) e posteriormente o trocador de calor manufaturado por fusão seletiva a *laser* (SLMHE), objeto de interesse do presente estudo. Este trabalho é divido em duas etapas, a primeira etapa consiste em analisar, empregando a dinâmica computacional dos fluidos (CFD), o desempenho termo hidráulico de um SLMHE, fabricado em aço inoxidável AISI 316L, de fluxo cruzado (água quente e ar em temperatura ambiente) com núcleo cúbico e mini canais circulares retos. Além disso, foi desenvolvido e avaliado um núcleo com mini canais semicirculares mantendo as proporções do protótipo (diâmetro hidráulico e área total de transferência de calor). Na segunda etapa, um conjunto de dois canais (quente e frio) com diferentes arranjos (circular reto, circular reto deformado e circular caótico) foram desenvolvidos e analisados de modo a estudar a influência do formato dos canais no desempenho termo hidráulico de trocadores de calor. As simulações foram realizadas com o auxílio do programa *ANSYS CFX* e validadas através de dados experimentais para o núcleo completo com canais circulares e pelo modelo numérico para o canal individual circular reto. A definição da melhor configuração de canais, foi realizada através da comparação dos resultados obtidos para a taxa de transferência de calor e a perda de carga em uma determinada faixa de *Re*. O núcleo completo com canais circulares apresentou resultados inferiores aos experimentais na taxa de transferência de calor no ramal quente, e superiores no ramal frio, com diferença média de 5% e 10%, respectivamente. Já na queda de pressão, o modelo numérico obteve resultados inferiores aos experimentais, com uma diferença média de 35% no ramal quente e 19% no ramal frio. O núcleo completo com canais semicirculares apresentou resultados similares ao de canais circulares, mostrando uma redução de 6% na taxa de transferência de calor, em ambos os ramais. Na queda de pressão, a redução de foi 12% e 15%, nos ramais quente e frio, respectivamente. Dentre os canais individuais, apesar do canal caótico apresentar os maiores resultados, foi o canal circular reto que exibiu a melhor combinação entre transferência de calor e queda de pressão.

Palavras-chave: trocador de calor; desempenho termo hidráulico; PCHE; SLMHE; CFD.

RESUMO EXPANDIDO

Introdução

Com o avanço tecnológico, é imprescindível um controle mais eficiente da temperatura em certos equipamentos e processos, tornando os permutadores de calor uma parte fundamental para o desenvolvimento da indústria. O presente trabalho tem como objeto de estudo um protótipo de trocador de calor compacto com canal circular reto fabricado por meio da fusão seletiva a *laser* (SLM), uma categoria do método de fusão em leito de pó a *laser* (L-PBF) do processo de manufatura aditiva (MA). Até à data desta dissertação, os estudos publicados analisando permutadores de calor fabricados por SLM são escassos, e o presente trabalho visa contribuir para uma melhor compreensão de seus efeitos na transferência de calor e na queda de pressão do equipamento. Para facilitar a nomenclatura, ao longo desta dissertação, o trocador de calor fabricado via SLM será denominado SLMHE.

Objetivos

O principal objetivo deste estudo é comparar o desempenho do permutador de calor SLMHE com outras configurações de canais por meio da análise numérica, com o intuito de investigar sua influência na eficiência termo hidráulica. Para atingir esse propósito, os seguintes objetivos específicos foram estabelecidos: (1) realizar uma revisão bibliográfica do SLMHE, dos diferentes arranjos de canais baseadas em PCHE e dos canais tridimensionais caóticos; (2) implementar um modelo numérico do protótipo de trocador de calor de fluxo cruzado (água quente e ar à temperatura ambiente) com mini canais circulares retos e validá-lo através de dados experimentais; (3) desenvolver um modelo numérico do SLMHE com canais de seção transversal semicircular reto, equivalentes à configuração de canais circulares, comparar e analisar os resultados de transferência de calor e queda de pressão de ambos os modelos; e (4) realizar um estudo dos efeitos da geometria da seção transversal do canal na transferência de calor e queda de pressão considerando canais retos com seção transversal circular e circular deformada, e canal caótico em forma de V inclinado com seção transversal circular.

Metodologia

A metodologia adotada neste trabalho envolve várias etapas distintas. Primeiramente, foram elaborados dois modelos numéricos para um permutador de calor compacto com mini canais retos. O primeiro modelo corresponde ao protótipo do SLMHE, possuindo canais com seção transversal circular, enquanto o segundo modelo é uma variação do primeiro substituindo os canais circulares por semicirculares, com diâmetro hidráulico e área de transferência de calor, equivalentes. Esta etapa tem como objetivo comparar os resultados da transferência de calor e queda de pressão entre os modelos de canal circular e canal semicircular. Posteriormente, três modelos numéricos foram desenvolvidos para canais individuais de diferentes geometrias, incluindo circular reto, circular deformado reto (depressão no topo do cilindro), e circular caótico em forma de V inclinado a 55° com a horizontal, todos com o mesmo diâmetro hidráulico e comprimento do canal do núcleo completo. O propósito desta etapa é realizar um estudo sobre os efeitos da geometria da seção transversal do canal na transferência de calor e queda de pressão.

Realizou-se o teste de independência da malha para os cinco modelos numéricos e a validação dos modelos com seção transversal circular foi efetuada por meio dos dados experimentais para o núcleo completo, e através do primeiro modelo numérico para o canal individual. O desempenho termo hidráulico dos modelos numéricos foi avaliado usando o programa *ANSYS CFX 18.2*, as geometrias foram modeladas com o *SolidWorks* e o módulo *DesignModeler* do *ANSYS* foi utilizado para realizar ajustes e simplificações geométricas (condição de simetria), e criar os domínios fluidos. As malhas hexagonais foram desenvolvidas através do *ANSYS*

ICEM, exceto no modelo do canal caótico que, por possuir geometria complexa, exigiu o método *MultiZone* do *ANSYS Meshing*. O *Shear Stress Transport* (SST) foi aplicado como modelo de turbulência e a convergência da análise é alcançada utilizando os critérios de convergência residual de 10^{-6} RMS e de equações da conservação de 0,01 (1%).
Neste estudo, apenas vinte e cinco dos testes experimentais foram reproduzidos numericamente devido ao custo computacional. O núcleo completo do trocador de calor de fluxo cruzado consiste em um cubo de arestas de 100 mm, com 171 e 190 canais para o ramal quente (água) e frio (ar), respectivamente, com diâmetros hidráulicos de 1,70 mm e 1,83 mm. A temperatura da água varia de 40 ºC a 80 ºC, com um incremento de 10 ºC, e sua vazão mássica é mantida constante ($\dot{m}_h$ = 0,264 kg/s) a cada temperatura. Para o ar há nove níveis de vazão mássica, de 0,085 a 0,051 kg/s (1.500 ≤ *Re* ≤ 10.000), e sua temperatura de entrada é mantida constante (à temperatura ambiente) durante os testes experimentais.
No estudo dos canais individuais, apenas os cinco casos centrais foram simulados para cada geometria de canal proposta de modo a reduzir o custo computacional. Cada canal foi examinado separadamente, tendo todos eles um comprimento desdobrado de 100 mm e um paralelogramo adicional de 45 mm nas extremidades para representar o escoamento do bocal. As condições de contorno empregadas são idênticas às do núcleo completo, com a exceção de que o fluxo de massa e a taxa de transferência de calor por unidade de área são divididos pelo número de canais presentes em cada ramal. Tais parâmetros foram obtidos a partir do estudo de Silva et al. (2021), que forneceu os dados necessários às condições de contorno.

Resultados e Discussões
O estudo de independência de malha para o núcleo completo foi realizado através da análise da taxa de transferência de calor e queda de pressão para ambas as configurações de canais. Para os canais circulares, uma malha com um total de 9.385.291 elementos (Malha 4) foi selecionada e para os canais semicirculares, foi escolhida uma malha com 5.441.188 elementos (Malha 2). Já para o caso dos canais individuais, a estabilização das propriedades avaliadas ocorre na primeira malha testada, com um total de: 2.703.417 (circular) e 2.703.417 (circular deformado) elementos para os canais retos e para o canal caótico com seção transversal circular um total de 3.532.146 (ramal quente) e 3.992.392 (ramal frio) elementos.
A validação do modelo numérico do núcleo completo com mini canais circulares ocorreu por meio da comparação com os dados experimentais de Silva et al. (2021), resultando em uma boa concordância entre eles. Na taxa de transferência de calor, o modelo numérico apresentou, em sua maioria, resultados inferiores aos experimentais no ramal quente e superiores no ramal frio. A diferença média entre eles foi de 5% para o ramal quente e 10% para o ramal frio. Já na queda de pressão, o modelo numérico apresenta resultados inferiores aos experimentais, em ambos os ramais. Os valores são constantes no ramal quente e apresentam uma diferença máxima de 41%, diminuindo com o aumento da temperatura da água, resultando em uma média de 35% em comparação com os dados experimentais. No ramal frio, a diferença média é de cerca de 19% e aumenta com o número de Reynolds, atingindo a máxima de 29% para *Re* > 7.000. Para verificar a discrepância entre os resultados numéricos e experimentais na queda de pressão, foi realizada uma comparação entre os três modelos: experimental, teórico e numérico. Essa comparação foi realizada apenas no ramal frio, uma vez que a queda de pressão no ramal quente é constante. Em sua maioria, os dados experimentais apresentaram os maiores resultados, seguido pelo modelo teórico e por fim o modelo numérico. O modelo teórico também foi desenvolvido por Silva et al. (2021) e apresentou uma diferença de até 26% para *Re* > 6.000 e inferiores a 15% para o regime laminar em comparação com o experimental. Por outro lado, na comparação entre os resultados teóricos e numéricos, as menores diferenças ocorreram para *Re* > 6.000 (diminuindo com o crescimento de *Re*), com valores inferiores a 12%. Para o regime laminar os resultados foram semelhantes, ficando abaixo dos 20%. A grande concordância dos

modelos teórico e numérico para elevados números de Reynolds reforça a suspeita de que a deformação do canal interfere diretamente na queda de pressão, já que ambos consideram o canal circular com geometria constante. Ao contrário do protótipo que apresenta imperfeições geométricas no canal circular, decorrentes do processo de manufatura. Outras causas para a discrepância nos resultados finais estão relacionadas à má-distribuição do escoamento e à não uniformidade do diâmetro ao longo do canal.

Foi realizada a validação do modelo numérico para um canal individual com seção transversal circular, comparando seus resultados com o modelo de núcleo completo com canais circulares. O canal individual apresentou resultados menores que o núcleo completo, para o número de Nusselt (*Nu*) e a queda de pressão. Para *Nu*, a diferença média foi de 8% para o ramal quente e 5% para o ramal frio, apontando valores constantes em ambos os ramais. Na queda de pressão, o ramal quente exibiu uma diferença média de 10%, enquanto o ramal frio mostrou uma diferença média de 18%. No ramal quente os valores foram constantes e no ramal frio a diferença máxima foi de 24% no primeiro caso (T60C1). Uma causa provável para esse comportamento é que, no modelo de canal único, a vazão mássica é aplicada apenas na entrada do canal, enquanto no modelo do trocador de calor completo, a vazão mássica é aplicada na entrada do bocal. Desta forma, em cada canal do modelo de núcleo completo, há uma distribuição não uniforme de escoamento, o que resulta em uma vazão mássica distinta na entrada de cada canal. A não uniformidade do escoamento afeta principalmente a queda de pressão total no permutador de calor, que será baseada na maior queda de pressão encontrada.

Ao comparar os permutadores de calor completos com canais de seção transversal circular e semicircular, observou-se que os canais semicirculares exibiram resultados semelhantes devido ao mesmo diâmetro hidráulico e área de troca térmica. Os canais semicirculares apresentaram uma redução média de 6% na taxa de transferência de calor em comparação com os canais circulares, em ambos os ramais. Na queda de pressão, os canais semicirculares obtiveram uma redução de 12% e 15%, nos ramais quente e frio, respectivamente, em relação aos canais circulares. Estes resultados são consistentes com o fato de o arranjo semicircular ter a mesma área de transferência de calor que o circular, mas a área da seção transversal do seu canal ser maior, o que reduz a velocidade local do fluido e provoca uma menor taxa de transferência de calor e queda de pressão. Realizando um estudo mais aprofundado da queda de pressão total ao longo de todo o sistema (bocal entrada + núcleo + bocal saída), observou-se que a maior queda de pressão ocorreu no núcleo do trocador de calor, apresentando um valor médio de 83% e 73% para o núcleo com canais circulares nos ramais quente e frio, respectivamente. Já para o núcleo com canais semicirculares, a queda de pressão no núcleo foi de 82% para o ramal quente e 74% para o ramal frio. Estes resultados estão de acordo com os dados experimentais de Silva et al. (2021), que mostraram que o núcleo é responsável por aproximadamente 87% da queda de pressão total e as outras singularidades (bocais de entrada e saída, tê) são responsáveis pelos 13 % restantes.

Dentre as três configurações de canais individuais estudados, os canais circular deformado e caótico apresentaram resultados maiores em relação ao canal circular (validado), com o canal caótico exibindo os maiores valores para *Nu* e queda de pressão, seguido pelo canal deformado. Para *Nu*, o canal circular deformado obteve uma diferença média de 1% em ambos os ramais, com um valor máximo de 1% para o ramal quente e 2% para o frio. O canal caótico mostrou uma diferença de 95% no ramal quente e 71% no ramal frio. Em relação à queda de pressão, o canal circular deformado apresentou uma diferença média de 9% e 11% para os ramais quente e frio, respectivamente. Desta forma, a suspeita de que a circularidade do canal interfere diretamente nos resultados da queda de pressão é confirmada. Por fim, o canal caótico exibiu uma diferença média de 284% no ramal quente e 469% no ramal frio, com valores constantes para o ramal quente e uma diferença máxima de 497% para o ramal frio. Em suma, apesar do canal circular caótico apresentar um aumento significativo na troca térmica em relação ao canal circular reto, o aumento na queda de pressão foi muito maior, tornando esse arranjo desvantajoso para esta aplicação específica.

Conclusões

O estudo efetuou a análise numérica do desempenho termo hidráulico de dois SLMHE de fluxo cruzado com núcleo cúbico, um com mini canais circulares e outro com mini canais semicirculares retos. Adicionalmente, foi investigado um conjunto de dois canais (quente e frio) com diferentes configurações (circular reto, circular reto deformado e circular caótico) para estudar a influência do formato dos canais no desempenho termo hidráulico de trocadores de calor. As simulações foram conduzidas utilizando o programa *ANSYS CFX* e validadas por meio dos dados experimentais e do primeiro modelo numérico com canais circulares.

A validação do modelo numérico do núcleo completo com canais circulares apresentou uma boa concordância com os dados experimentais, embora com algumas discrepâncias nos resultados de queda de pressão. O modelo numérico apresentou resultados menores aos experimentais na taxa de transferência de calor e na queda de pressão, em ambos os ramais. A comparação entre os modelos, experimental, teórico e numérico revelou que os dados experimentais apresentaram os maiores resultados, seguido pelo modelo teórico e o modelo numérico. Entre os modelos, nota-se a grande concordância entre o numérico e o teórico para números elevados de Reynolds, uma vez que ambos consideram o canal circular com geometria constante, ao contrário do protótipo real que apresenta imperfeições geométricas no canal circular, decorrentes do processo de manufatura.

O resultado da validação do canal individual por meio do modelo de núcleo completo circular apresentou valores menores para o canal individual na troca térmica e na queda de pressão, em ambos os ramais. A causa dessa diferença é a má-distribuição do escoamento nos canais do núcleo completo, o que resulta em uma vazão mássica distinta na entrada de cada canal e afeta principalmente a queda de pressão total no permutador de calor.

O núcleo completo com canais de seção transversal circular e semicircular apresentaram resultados semelhantes devido ao mesmo diâmetro hidráulico e à mesma área de troca térmica. Contudo, os canais semicirculares apresentaram uma ligeira vantagem em relação aos canais circulares, na proporção da transferência de calor com a queda de pressão. Ao analisar a queda de pressão ao longo dos ramais, observou-se que a maior queda ocorre no núcleo do permutador de calor. É possível aumentar a área de troca térmica na configuração semicircular aumentando o número de canais e camadas, preservando o tamanho do núcleo e dos bocais, de modo a melhorar o desempenho termo hidráulico do trocador de calor. No entanto, é importante considerar que aumentar o número de canais semicirculares pode impactar o comportamento estrutural do permutador de calor, que não foi analisado neste estudo. Além disso, um arranjo semicircular pode favorecer a incrustação devido aos cantos vivos.

A investigação da influência da forma da seção transversal do canal no desempenho termo hidráulico, realizada utilizando canais individuais, aponta que a forma da seção transversal do canal interfere diretamente na queda de pressão, porém, na troca térmica esta interferência é menos significativa. O canal circular caótico apresentou os maiores valores de Nu e queda de pressão, seguido pelo canal circular deformado e pelo canal circular. Esses resultados confirmam a suspeita de que a circularidade do canal afeta diretamente os resultados da queda de pressão e justifica as diferenças entre os resultados experimentais e numéricos do núcleo completo com canais circulares. Embora o canal circular caótico tenha apresentado um aumento significativo na troca térmica em relação ao canal circular reto, o aumento na queda de pressão foi muito maior, tornando o arranjo desfavorável para esta aplicação. Um estudo mais aprofundado sobre o tema deve ser desenvolvido com o propósito de entender a discrepância dos resultados com os dados da literatura, que indicam uma superioridade do canal caótico em relação ao canal reto.

Palavras-chave: trocador de calor; desempenho termo hidráulico; PCHE; SLMHE; CFD.

ABSTRACT

Heat exchangers have widely used in industrial and domestic applications. One type frequently employed in offshore platforms is compact heat exchangers (CHE) due to their high thermal efficiency, high operating conditions, and high-density area. The constant search for improved methods for heat transfer has culminated in the development of new types of CHEs, such as the printed circuit heat exchanger (PCHE) and later the heat exchanger manufactured by selective laser melting (SLMHE), the object of interest of the present study. This work is divided into two stages. The first stage involves analyzing an SLMHE thermal-hydraulic performance, made of AISI 316L stainless steel, with a cross-flow design (hot water and air at room temperature) with a cubic core and straight circular mini channels, using computational fluid dynamics (CFD). In addition, an entire core with semicircular mini channels was developed and evaluated, maintaining the proportions of the prototype (hydraulic diameter and total heat transfer area). In the second stage, a two-channel set (hot and cold) with different arrangements (straight circular, deformed circular, and chaotic circular) was developed and analyzed to study the influence of channel shape on the thermal-hydraulic performance of heat exchangers. The simulations were evaluated using ANSYS CFX software and validated using experimental data for the complete core with circular channels and the numerical model for the individual straight circular channel. The optimal channel configuration was determined by evaluating the heat transfer rate and pressure drop results within a specific range of Reynolds numbers. The complete core with circular channels presented inferior results compared to the experimental results for the hot branch heat transfer rate and superior results for the cold branch, with an average difference of 5% and 10%, respectively. In the pressure drop, the numerical model obtained inferior results compared to the experimental data, with an average difference of 35% on the hot branch and 19% on the cold branch. The entire core with semicircular channels presented similar results to the circular channels, with a reduction of 6% in heat transfer rate on both branches. The hot and cold branches experienced a 12% and 15% reduction in pressure drop, respectively. Amongst the individual channels, the chaotic circular channel showed the highest results, but the straight circular channel exhibited the best combination of heat transfer and pressure drop.

Keywords: heat exchanger; thermal-hydraulic performance; PCHE; SLMHE; CFD.

LIST OF FIGURES

Figure 1 – Printed circuit heat exchanger. (a) Flow channel, (b) diffusion bonded core, (c) comparison of the size of PCHE shell and tube heat exchanger (smaller size) with a conventional exchanger (bigger size) for similar duty. 21
Figure 2 – Examples of SLM manufacture. (a) Heat exchanger manufactured by Senai, (b) A recuperator produced by HiETA using additive manufacturing (longest side ≈ 40 cm), and (c) Heat exchanger structures in SLM from HiETA. 23
Figure 3 – Geometric parameter of the core (a) and schematic illustration of the axial configuration tests (b). 24
Figure 4 – Geometry manufactured by Electro-Optical Systems (EOS) (a) and L-PBF technique (b). Internal layout (c). 25
Figure 5 – Schematic diagram of flow arrangements and channels of PCHEs: (a) cross-flow; (b) parallel-flow; (c) counter-flow; (d) heat exchanger unit types. 27
Figure 6 – Velocity profiles for semicircular and circular channel shapes. 28
Figure 7 – Streamline schematic of PCHE with four different inlet headers (Re_{in} = 2.89×10^5). 29
Figure 8 – Geometries studied. 32
Figure 9 – Flowchart encapsulating the flow physics in CFD. 33
Figure 10 – Overview process of the computational solution procedure. 34
Figure 11 – A representation of structured and unstructured mesh for FVM (full symbols denote element vertices, and open symbols at the center of the control volumes denote computational nodes). 35
Figure 12 – Hierarchy of turbulence models. 36
Figure 13 – Typical velocity profile for a turbulent boundary layer. 41
Figure 14 – CFD methodology flowchart. 45
Figure 15 – Geometric parameter of the core with circular (a) and semicircular (b) channels, and nozzle (c) (all dimensions are in mm). 47
Figure 16 – Heat exchanger model. 51
Figure 17 – Heat exchanger model with symmetry condition. 54
Figure 18 – Single channel geometries studied: circular (a), deformed circular (b), and inclined V-shaped chaotic circular (c). 55
Figure 19 – Representation of the hot branch of the chaotic channel in a V-shape with 55° inclination to the horizontal and circular cross-section. 56

Figure 20 – Mesh of circular (a) and semicircular (b) cross-section. 59
Figure 21 – Circular channel mesh independence study. 60
Figure 22 – Circular channel, y^+ region. 61
Figure 23 – Semicircular channel mesh independence study. 62
Figure 24 – Semicircular channel, y^+ region. 63
Figure 25 – Mesh of circular (a), deformed circular (b), and chaotic channels with circular cross-sections (c). 64
Figure 26 – Single channel mesh independence study: circular (a), deformed circular (b), and chaotic channels with circular cross-sections (c). 65
Figure 27 – Semicircular channel, y^+ region of circular (a), deformed circular (b), and chaotic channels with circular cross-sections (c). 66
Figure 28 – Heat transfer rate comparison of experimental and numerical results for the heat exchanger with the circular channel: (a) as heat transfer rate and (b) as a function of Re_{cold}. 68
Figure 29 – Pressure drops comparison of experimental and numerical results: (a) as pressure drop and (b) as a function of Re_{cold}. 70
Figure 30 – Theoretical model comparison for the cold branch. 72
Figure 31 – Complete core and single channel comparison of Nusselt number for the heat exchanger of circular cross-section: (a) as Nu and (b) as a function of Re_{cold}. 74
Figure 32 – Complete core and single channel comparison of pressure drop for the heat exchanger of circular cross-section: (a) as pressure drop and (b) as a function of Re_{cold}. 75
Figure 33 – Temperature range for circular (a) and semicircular (b) cross-section of complete geometry for case T60C5. 76
Figure 34 – Circular vs semicircular heat transfer rate: (a) as heat transfer rate and (b) as a function of Re_{cold}. 78
Figure 35 – Streamline of circular (a) and semicircular (b) cross-section for complete geometry to case T60C5. 79
Figure 36 – Pressure range of circular (a) and semicircular (b) cross-section for complete geometry to case T60C5. 80
Figure 37 – Circular vs semicircular pressure drop: (a) as pressure drop and (b) as a function of Re_{cold}. 82
Figure 38 – Positioning planes along the system (a) and analysis of the pressure drop of the circular and semicircular cross-section for complete geometry to case T60C5 (b). 83
Figure 39 – Nusselt number comparison of the single channel geometries: (a) as Nu and (b) as a function of Re_{cold}. 86

Figure 40 – Pressure drop comparison of the single channel geometries: (a) as pressure drop and (b) as a function of Re_{cold}. 87
Figure 41 – Chaotic channels studied. 101
Figure 42 – Location of the planes to calculate *Nu* and *f*. 101
Figure 43 – Average Nusselt number (a) and average Poiseuille number (b) along the channels. 104
Figure 44 – Average *Nu* distribution for *Re* = 200 for the different channel configurations. 105

LIST OF TABLES

Table 1 – SLMHE geometry specifications. 48
Table 2 – Diameter calculation for channels with semicircular cross-section. 49
Table 3 – Boundary conditions. 52
Table 4 – Material Properties. 53
Table 5 – Boundary conditions for the single channels. 57
Table 6 – Experimental and numerical heat transfer rate for the heat exchanger with a circular channel. 67
Table 7 – Experimental and numerical comparison of pressure drop for the heat exchanger of circular channel. 69
Table 8 – Model Comparison. 71
Table 9 – Complete core and single channel comparison of Nusselt number for the heat exchanger of circular cross-section. 73
Table 10 – Complete core and single channel comparison of pressure drop for the heat exchanger of circular cross-section. 74
Table 11 – Circular vs semicircular heat transfer rate. 77
Table 12 – Circular vs semicircular pressure drop. 81
Table 13 – Nusselt number comparison of the single channel geometries. 85
Table 14 – Pressure drop comparison of the single channel geometries. 87
Table 15 – Representative thermo-hydraulic performance studies of straight-channel PCHEs. 96
Table 16 – Summary of heat transfer correlations for straight channel PCHEs 99
Table 17 – Geometric features and boundary conditions. 102
Table 18 – Numerical model validation result. 103
Table 19 – Data on the thermo-hydraulic behavior of the studied channels. 104
Table 20 – Experimental data used in the numerical study. 106
Table 21 – Circular channel mesh characteristics. 108
Table 22 – Semicircular channel mesh characteristics. 109
Table 23 – Single channels mesh characteristics. 110
Table 24 – The numerical result of the complete core with circular channels. 111
Table 25 – The numerical result of the complete core with semicircular channels. 112

Table 26 – Pressure drop by plane of the hot branch for complete core with circular channels. 113
Table 27 – Pressure drop by plane of the cold branch for complete core with circular channels. 114
Table 28 – Pressure drop by plane of the hot branch for complete core with semicircular channels. 115
Table 29 – Pressure drop by plane of the cold branch for complete core with semicircular channels. 116

LIST OF ABREVIATIONS AND ACRONYMS

ARS	Algebraic Reynolds-Stress
AM	Additive Manufacturing
CFD	Computational Fluid Dynamics
CHE	Compact Heat Exchanger
DMLS	Direct Metal Laser Sintering
DNS	Direct Numerical Simulation
EBM	Electron Beam Melting
EBAM	Electron Beam Additive Manufacturing
EOS	Electro-Optical Systems
FDM	Finite-Difference Method
FVM	Finite-Volume Method
LAM	Laser Additive Manufacturing
LES	Large-Eddy Simulation
LMD	Laser Metal Deposition
L-PBF	Laser Powder Bed Fusion
PCHE	Printed Circuit Heat Exchanger
RANS	Reynolds-Averaged Navier Stokes
RMS	Root Mean Square
RST	Reynolds-Stress Transport
SHS	Selective Heat Sintering
SLM	Selective Laser Melting
SLMHE	Selective Laser Melting Heat Exchanger
SLS	Selective Laser Sintering
SST	Shear Stress Transport
TPMS	Triply Periodic Minimal Surfaces
T2F	Thermal Fluid Flow
WAAM	Wire and Arc Additive Manufacturing

LIST OF SYMBOLS

A_f	Free flow area	[m²]
A_p	Channel wall area	[m²]
A_s	Surface area	[m²]
A_{tot}	Total heat transfer area	[m²]
A_{st}	Fin cross-sectional area	[m²]
C	Coefficient for calculating friction factor correlation	[-]
c_p	Specific heat of fluid	[J/kg-K]
d	Diameter	[m]
D_h	Hydraulic diameter	[m]
d_{wall}	Channel wall distance	
e	Distance between layers	[m]
f	Fanning friction factor	[-]
f_D	Darcy's friction factor	[-]
f_l	Blending function	[-]
F_h	Height flow region	[m]
F_l	Length flow region	[m]
g	Gravity acceleration	[m/s^2]
h	Convective coefficient	[Wm^{-2}K^{-1}]
H	Height	[m]
k	Thermal conductivity	[W/m-K]
K	Turbulent kinetic energy	[m^{2}s^{-2}]
K_a	Von Karmann constant	[-]
L	Length	[m]
M	Mass molar	[g/mol]
$\dot{m}$	Mass flow rate	[kg/s]

N	Number of layers for each branch	[-]
n	Number of channels per layer	[-]
$\vec{n}$	Normal direction	[-]
Nu	Nusselt number	[-]
P	Pressure	[Pa]
Pr	Prandtl number	[-]
p	Distance between the center of the channels	[m]
q	Heat transfer rate	[W]
Ra	Average surface roughness	[μm]
Re	Reynolds number	[-]
S_l	Modulus of the average shear rate	[-]
$\bar{S}_{ji}$	Mean strain-rate tensor	[-]
t	Time	[s]
T	Temperature	[°C]
T_w	Tall averaged temperature	[°C]
T^+	Non-dimensional temperature	[-]
$\bar{u}$	Time-averaged velocity	[m/s]
u	Velocity	[m/s]
U	Centerline velocity	[m/s]
u^+	Non-dimensional velocity	[-]
u^*	Friction velocity	[m/s]
V	Total exchanger core volume	[m^3]
W	Width	[m]
y	Wall distance	[m]
y^+	Non-dimensional wall distance	[-]

Subscripts

c	*Cold*
h	*Hot*
i, j, w	*Refers to an axis [X, Y, Z]*
in	*Inlet*
m, avg	*Average*
out	*Outlet*

Greek Alphabet

ΔP	Pressure drop	[Pa]
ε	Turbulence energy dissipation rate	[m^2s^{-3}]
$k-\varepsilon$	ε Based turbulence model	[-]
$k-\omega$	ω Based turbulence model	[-]
λ	Thermal conductivity	[W/m-K]
μ	Fluid dynamic viscosity	[Nsm^{-2}]
μ_t	Turbulent viscosity	[Nsm^{-2}]
ρ	Density	[kgm^{-3}]
τ_{ij}^F	Reynolds-averaged turbulent stresses	[-]
τ_{ij}^R	Reynolds-stress tensor	[-]
ϕ	Area Enlargement Factor	[-]
$\O_1$, $\O_2$	Constants in SST model	[-]
φ	Heat flux	[W/m^2]
ω	Turbulence frequency	[Hz]

CONTENTS

1 INTRODUCTION 17

1.1 OBJECTIVES 18

1.1.1 Main Objective 18

1.1.2 Specific Objectives 18

1.2 JUSTIFICATIVE 19

1.3 STRUCTURE OF THE WORK 19

2 THEORETICAL BACKGROUND AND LITERATURE REVIEW 20

2.1 THEORETICAL BACKGROUND 20

2.1.1 Compact Heat Exchangers 20

2.1.1.1 Printed Circuit Heat Exchanger 20

2.1.1.2 Heat Exchanger Manufactured via SLM 22

2.2 LITERATURE REVIEW 24

2.2.1 SLMHE 24

2.2.2 PCHE 26

2.2.3 Chaotic Channels 31

3 NUMERICAL METHOD 33

3.1 DISCRETIZATION OF GOVERNING EQUATIONS 33

3.2 TURBULENCE MODELING 36

3.3 SHEAR STRESS TRANSPORT MODEL (SST) 38

3.4 WALL TREATMENT 40

3.5 GLOBAL PARAMETERS 43

4 METHODOLOGY 45

4.1 CIRCULAR AND SEMICIRCULAR CHANNEL GEOMETRIES 46

4.1.1 Computational Domain 46

4.1.2 Boundary Conditions and Solver Settings 50

4.1.3 Symmetry Condition 53

4.2 SINGLE CHANNEL GEOMETRIES 54

4.2.1 Computational Domain 54

4.2.2 Boundary Conditions and Solver Settings 56

5 RESULTS AND DISCUSSIONS 58

5.1 MESH INDEPENDENCE STUDY 58

5.1.1 Complete Core 58

5.1.2 Single Channel Geometries 63

5.2 NUMERICAL MODEL VALIDATION 67

5.2.1 Complete Core 67

5.2.1.1 Theorical Model Comparison 71

5.2.2 Single Channel Geometry 73

5.3 CIRCULAR VS. SEMICIRCULAR CROSS-SECTION 76

5.3.1 Heat Transfer Analysis in the Complete Heat Exchanger 76

5.3.2 Pressure Drop Analysis in the Complete Heat Exchanger 80

5.4 SINGLE CHANNEL GEOMETRIES 85

6 CONCLUSIONS 89

BIBLIOGRAPHY 92

APPENDIX A – Additional Literature Review Data 96

APPENDIX – Preliminary Study of the Chaotic Channels 100

APPENDIX C – Numerical Results 106

1 INTRODUCTION

With the advance in technology, better temperature control is required in certain equipment and processes making heat exchangers a fundamental part of the industry. Thereby different types of heat exchangers have been developed for a wide variety of applications such as power production, petrochemical and food industries, environmental engineering, process, manufacturing industry, electronics, waste heat recovery, air conditioning, refrigeration, and space applications.

Heat exchangers are devices that promote the transfer of thermal energy between two or more fluids at different temperatures and in thermal contact. This heat exchange can occur between a solid surface and a fluid (SHAH; SEKULIC, 2003). Existing models can be classified according to some main criteria, such as recuperators or regenerators; transfer processes (direct and indirect contact); geometry of construction (tubes, plates, and extended surfaces); heat transfer mechanisms (single-phase and two-phase); and arrangements (parallel flows, counter flows, and cross flows) (KAKAÇ; LIU; PRAMUANJAROENKIJ, 2012).

Among the categories of construction geometry is the printed circuit heat exchanger (PCHE), which is a plate-fin type compact heat exchanger with a complicated channel structure. It is the coupling of the complicated channel structure together with the drastic variations in the thermal properties of the working fluid that make the thermo-hydraulic characteristics of the PCHEs distinct from typical heat exchangers (LIU; HUANG; WANG; LIU, 2020). The use of a three-dimensional (3D) chaotic channel geometry in the heat exchangers significantly improves convective heat transfer over that of more common shapes of channels (LASBET; AUVITY; CASTELAIN; PEERHOSSAINI, 2007).

Currently, for some specialized applications and different forms of channels, several new manufacturing techniques are being developed such as selective laser melting (SLM), which is a category of laser powder bed fusion (L-PBF) method of additive manufacturing (AM) processes which melts or sinters the powdered material layer-by-layer to create a 3D solid structure. In this method, the process parameters and building orientation influence the surface roughness and this roughness can be beneficial for heat transfer enhancement applications (KAUR; SINGH, 2021).

A prototype of a compact heat exchanger manufactured by SLM with circular channels is the focus of this study, further details of these types of equipment are presented later in section 2.1.1. Up to the date of this work, very few studies have been published analyzing heat exchangers manufactured by this technology and the present study contributes to understanding more about its effects on the heat transfer and pressure drop of the equipment. To facilitate nomenclature, throughout this work, the heat exchanger manufactured by SLM will be called SLMHE.

1.1 OBJECTIVES

1.1.1 Main Objective

The main objective of this study is the numerical analysis of an SLMHE heat exchanger and the comparison of its thermal-fluid flow behavior with other channel configurations, aiming to determine the flow behavior and the influence of the channel geometry on thermal-hydraulic efficiency.

1.1.2 Specific Objectives

- Present a literature review of the main object of study (SLMHE), the different channel configurations based on PCHE and three-dimensional chaotic channels, aiming to investigate the flow behavior and numerical modeling applied for similar heat exchanger configurations;
- Implement a 3D numerical model cross-flow heat exchanger (hot water and air at room temperature) with circular straight, mini channels;
- Validate the numerical circular mini channels configuration model using experimental data;
- Investigate possible causes of discrepancies between the numerical model and experimental results;
- Develop a numerical model of the SLMHE core with a semicircular cross-section with straight channels equivalent to the circular channel configuration;
- Compare and analyze results of heat transfer and pressure drop from both models;
- Study of the effects of channel cross-section geometry on heat transfer and pressure drop (straight channels with circular and deformed circular cross-sections, and inclined V-shaped chaotic channel with circular cross-section).

1.2 JUSTIFICATIVE

Since additive manufacturing is a recent technology being used in the field of heat exchangers, published studies regarding compact heat exchangers manufactured by selective laser melting (SLMHE) are sparse in the literature. The scarcity of the topics covered in this dissertation highlights the need for more studies dedicated to SLMHE and the different channel structure possibilities applied to it. Furthermore, studies on channel configurations for Compact Heat Exchangers usually focus on a limited number of channels for hot and cold branches to represent the heat exchanger. However, the influence of the heat exchanger nozzle coupling is significant to understand the effects of pressure drop in the equipment as a whole. This study analyzes the heat exchanger in a whole configuration, comprising the inlet and outlet nozzles and its entire structure, making it possible to study the influence of these accessories on the flow. And lastly, the technology used to manufacture the heat exchanger in this study is subjected to manufacturing limits for a heat exchanger of mini channels as uncertainties in the diameters of the channels and superficial roughness are intrinsic to the method. Nevertheless, these effects are taken into account in this study when comparing the numerical results to experimental data.

1.3 STRUCTURE OF THE WORK

This dissertation is structured into five chapters. In Chapter 1, a brief introduction to the subject matter is provided, along with the study objectives. Chapter 2 describes the fundamentals of PCHE and SLMHE and presents a comprehensive review of experimental and numerical results relevant to the topic found in the literature. Mathematical models and numerical techniques are shown in Chapter 3. Chapter 4 outlines the methodology employed in this work. The results and subsequent discussions are detailed in Chapter 5. Finally, Chapter 6 compiles the research and presents the conclusions obtained.

2 THEORETICAL BACKGROUND AND LITERATURE REVIEW

For the development of the proposed study, it is necessary to approach the operation of the device studied, the physical and mathematical understanding of the problem, the tool chosen for the development of the analysis and present the works already done in the area by other authors. This section begins by presenting the theoretical background of compact heat exchangers and the fabrication utilizing the SLM technique addressed in this work. The chapter ends with a literature review focused on experimental and numerical studies done in SLMHE and PCHE, due to the resemblance of the latter to the former.

2.1 THEORETICAL BACKGROUND

2.1.1 Compact Heat Exchangers

As previously explained, a heat exchanger is a device that provides the transfer of heat between two or more fluids at different temperatures. Objectively, this study will address the heat exchangers known as recuperators where the thermal energy is transferred through a separating wall while the streams flow simultaneously (direct-transfer-type heat exchangers).

These types of equipment are often classified according to their construction characteristics. An important performance factor for heat exchangers is the *compaction factor* (measured in m^2/m^3), defined as the amount of heat transfer surface area within the heat exchanger volume. A compact heat exchanger (CHE) is defined as one which incorporates a heat transfer surface having a high area density, generally, greater than 700 m^2/m^3 (usually met by CHE with a hydraulic diameter ≈ 4 mm). A heat exchanger is referred to as a micro heat exchanger if the surface area density is above 10,000 m^2/m^3 (ZOHURI, 2017).

Within the class of compact heat exchangers is the PCHE, the precursor to the heat exchanger manufactured via the SLM process studied in this paper. Both are presented below.

2.1.1.1 Printed Circuit Heat Exchanger

The Printed Circuit Heat Exchanger (PCHE) was developed by the Heatric Division of Meggitt (UK) Ltd. for refrigeration applications. Its name is derived from the manufacturing process of the flat metal plates that make up the core of the heat exchanger. The plates are etched photochemically on one side to create the fluid passage, and then stacked and connected by diffusion to form a solid metal block with fluid flow passages. Multiple blocks can be welded together to create a single core with flow capacity at any level (see Figure 1), which is then welded to the headers and nozzles that direct the fluids to the appropriate sets of passages (ZOHURI, 2017). PCHEs are welded and connected by diffusion, eliminating the need for gaskets or brazing material. These materials can cause leakage, fluid incompatibility, and temperature limitations in other technologies, making PCHEs more reliable and durable (THULUKKANAM, 2013).

PCHEs are capable of multiple passes and multiple fluid streams in a single block. The passage shape may be corrugated or straight, depending on the heat load and pressure drop relationship, and the channels are typically semicircular. The low porosity of the exchanger results from the surface form, which typically increases the weight and lateral dimensions of the exchanger for similar hydraulic diameters. High surface area densities, ranging from 650 to 1300 m^2/m^3 can be achieved for operating pressures of 50 Pa to 10 MPa and temperatures of 150 to 800 °C (SHAH; SEKULIC, 2003) and (ZOHURI, 2017).

Figure 1 – Printed circuit heat exchanger. (a) Flow channel, (b) diffusion bonded core, (c) comparison of the size of PCHE shell and tube heat exchanger (smaller size) with a conventional exchanger (bigger size) for similar duty.

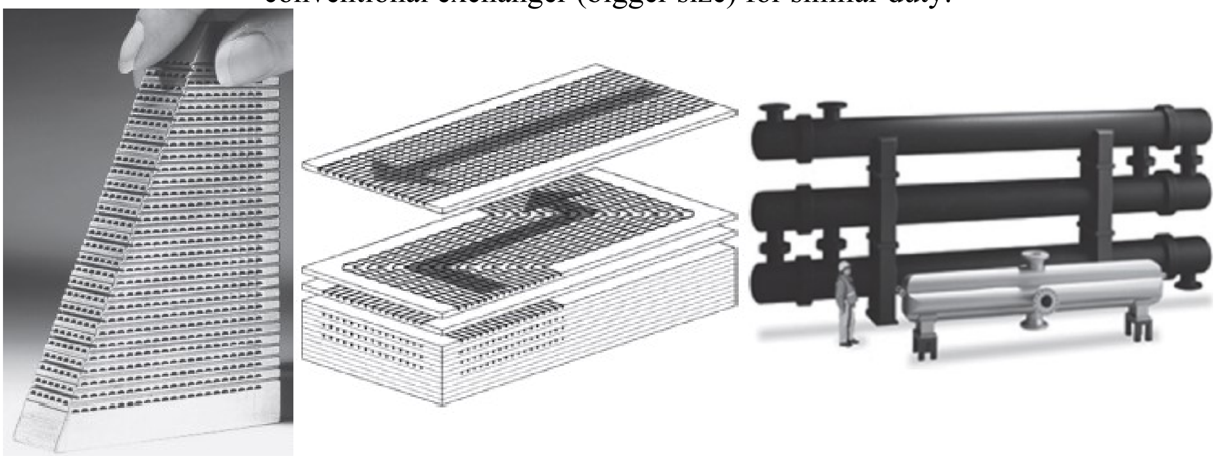

(a) (b) (c)

Source: Adapted from Thulukkanam (2013).

It has been used successfully with relatively clean gases, liquids, and phase-change fluids. They are used extensively in offshore oil platforms as compressor aftercoolers, gas coolers, and cryogenic processes to remove inert gases. Because it has a small channel size, the fluid pressure drop can be a constraint for low-to-moderate pressure applications. However, the main advantage of this exchanger is the high pressure/strength ratio, flexibility in design, and high effectiveness (in order of 98%) (SHAH; SEKULIC, 2003). A range of materials, including stainless steel such as SS 316L, SS 316, SS 304, SS 904L, titanium, copper, cupronickel, Monel, nickel, and super alloys Inconel 600, Incoloy 800, and 825, can be used (ZOHURI, 2017).

2.1.1.2 Heat Exchanger Manufactured via SLM

Additive manufacturing (AM) is a process of joining materials to make objects from 3D model data and can also be called rapid prototyping, layered manufacturing, solid fabrication free-form, and 3D printing. For metal, AM technology can be classified into three types: wire and arc additive manufacturing (WAAM), electron beam additive manufacturing (EBAM), and the most promising technology, laser additive manufacturing (LAM). The latter majorly contains two classes: laser metal deposition (LMD), which utilizes synchronous powder or wire feeding, and laser powder bed fusion (L-PBF), which employs a powder bed formation approach. The L-PBF method comprises several widely employed printing techniques, namely direct metal laser sintering (DMLS), electron beam melting (EBM), selective heat sintering (SHS), selective laser melting (SLM), and selective laser sintering (SLS). The SLM technique was developed on the base of SLS in the late 1980s and can be used for manufacturing precision parts of complex shapes (GONG et al., 2021).

In the SLM technique, granular powder of raw material is placed layer by layer where a positioned laser melts the powder with a scanning system in an oxygen-free atmosphere. This method needs less raw material and cycles than other additive manufacturing processes, allowing it to work with a range of materials. The most used is 316L stainless steel, due to its good corrosion and pitting resistance, compared with other traditional stainless steel materials (SILVA et al., 2021). Some examples can be seen in Figure 2.

The major advantages of SLM are the ability to produce lighter components with good mechanical quality, low surface roughness (using post treatments), mini channels, and complex geometries, increasing this way, the thermal performance. This offers great potential to at least relieve, if not overcome, the problems with metal (or carbon) foams, in that it is possible to design-in optimum structures when these can be fully defined (SILVA et al., 2021 and HESSELGREAVES; LAW; REAY, 2017). Another advantage is the ability to process nonferrous pure metals with a high density such as Ti, Al, and Cu, common in industry (GONG et al., 2021).

Some of the negative aspects of this process, are high cost and final product quality instability due to the high thermal gradients and the production per layer (stair-effect). This effect is responsible for low part accuracy, anisotropic mechanical properties, different grain microstructures, and high surface roughness obtained in the final product. However, some processes can considerably reduce roughness, reaching values of 1.4 μm (GONG et al., 2021 and SILVA et al., 2021).

Figure 2 – Examples of SLM manufacture. (a) Heat exchanger manufactured by Senai, (b) A recuperator produced by HiETA using additive manufacturing (longest side ≈ 40 cm), and (c) Heat exchanger structures in SLM from HiETA.

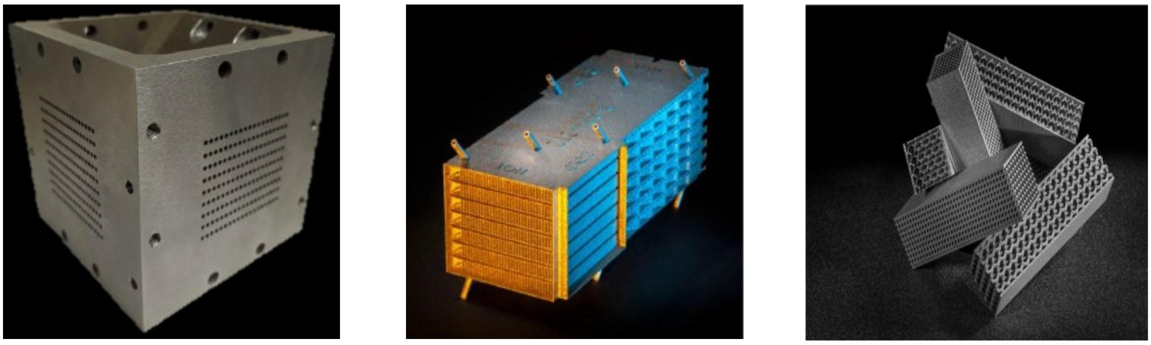

(a) (b) (c)

Source: Adapted from Silva et al. (2021) and Hesselgreaves, Law and Reay (2017).

Figure 2 (a) shows the core of the heat exchanger manufactured by the Senai Institute of Innovation of Joinville, using the SLM method with a chessboard-like technique. According to Silva et al. (2021), this procedure reduces the residual thermal stress, dividing the layers into small areas and melting them randomly. The material used was the gas-atomized AISI316L metallic powder with granulometry between 15 and 45 μm, with which layers of metallic powered with a thickness of 30 μm were formed. Finally, a stress relief treatment of 550°C was performed for 6 hours. It then observed a relative density of 99.8%, external surface roughness of 12.21 μm and a degree of compaction of 22.6 m^2/m^3.

The device illustrated in Figure 2 (a) is the heat exchanger manufactured by SLM previously referred in this work as SLMHE previously, referred to in this work as SLMHE, the main object of study in this dissertation. Since this technology is relatively new, there is a limited number of studies based on these heat exchangers. Therefore, a significant quota of the theoretical basis presented here will concentrate on PCHE heat exchangers.

2.2 LITERATURE REVIEW

The literature review described below aims to identify the main works related to the theme under development in this work, presenting its limitations and advances. As there are few numerical studies conducted on the thermal-hydraulic performance of SLMHE related to the topic covered, will also be indicated papers about PCHE and chaotic channels.

2.2.1 SLMHE

The primary subject of this dissertation focuses on the experimental paper by Silva et al. (2021) which explores the theoretical models for the thermo-hydrodynamic performance of a cross-flow SLMHE made of AISI 316L stainless steel. The heat exchanger core, presented in Figure 3, comprises straight circular mini-channels composed of hot (water) and cold (air) branches. The headers were manufactured in aluminum by the machining process. Was conducted two experimental test sets to evaluate the heat transfer and pressure drop in axial and perpendicular configurations.

Figure 3 – Geometric parameter of the core (a) and schematic illustration of the axial configuration tests (b).

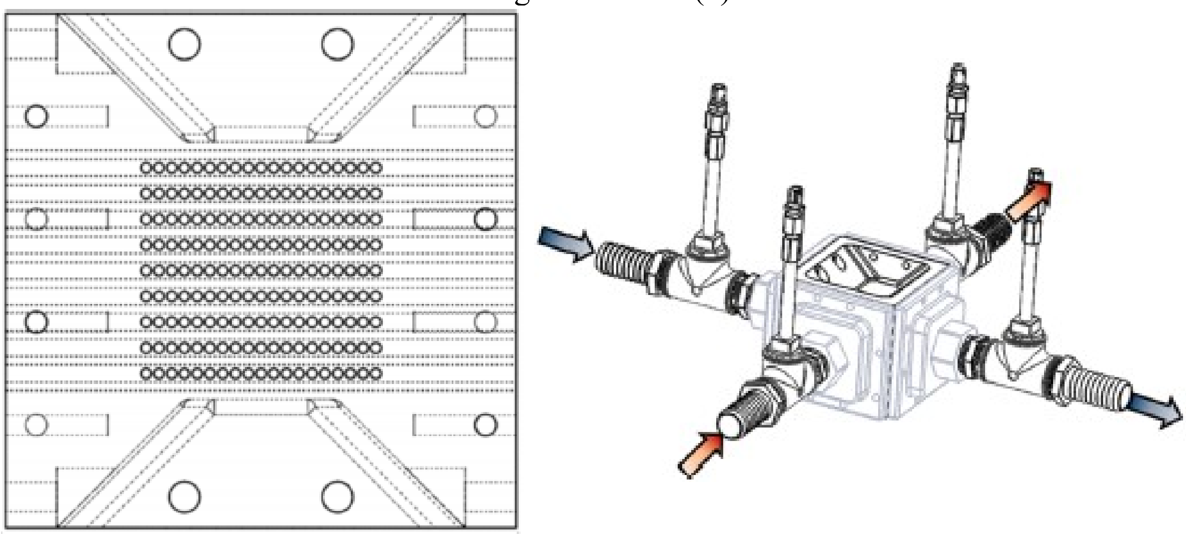

(a) (b)

Source: Silva et al. (2021).

The analytical models showed good agreement with experimental tests for the axial flow configuration, showing an average error of 3.3% for heat transfer rate and 15.3% for pressure loss. The manufacturing process caused inconsistencies in the surface roughness across the length and diameter dimensions, which influenced the pressure drop. The authors noted a proportionality correlation between the Reynolds number and the impact of roughness on the theoretical pressure drop model. However, the reduction in surface roughness has little effect on the total pressure drop. The present work uses the axial configuration information from the study by Silva et al. (2021) for numerical model validation and presents more details in the methodology and results sections.

To evaluate possible structural failures during the operation of compact heat exchangers, Zilio et al. (2022) conducted an experimental and numerical study to assess the mechanical behavior of prototypes of compact heat exchangers under high thermal and pressure gradients. The prototypes (Figure 4) were fabricated using additive manufacturing (AM) to simulate the compact core geometry of heat exchangers, with two core configurations produced in stainless steel 316L using different printing orientations: horizontal and vertical.

Figure 4 – Geometry manufactured by Electro-Optical Systems (EOS) (a) and L-PBF technique (b). Internal layout (c).

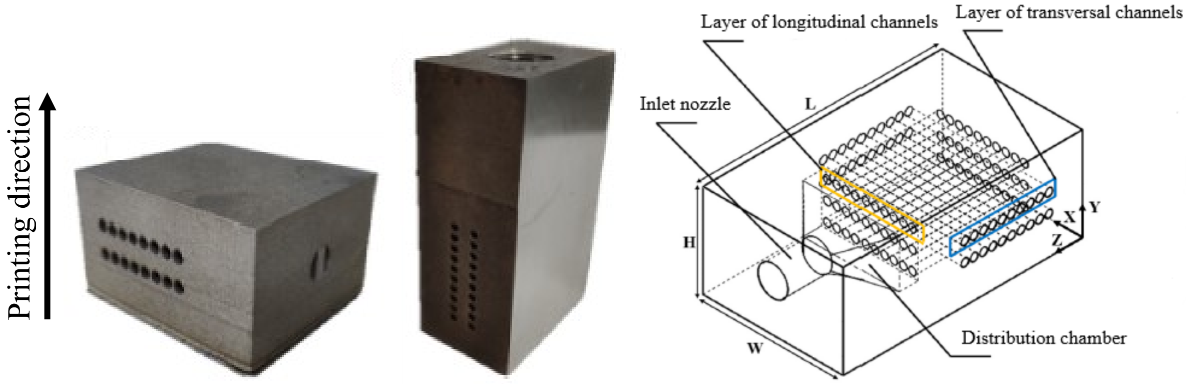

(a) (b) (c)

Source: Adapted from Zilio et al. (2022).

The samples were evaluated using a hydrostatic test bench with pressures up to 700 bar, and no leakage was observed even between longitudinal channels. The results showed that both prototypes exhibited good thermal-hydraulic and structural performance, with the printing orientation affecting material properties and stress levels. Machining processes after heat treatment for stress relief also locally altered mechanical properties, resulting in a difference of up to 15% at 350 bar. The numerical structural study showed good agreement with the experimental tests, indicating that the geometric characteristics of the prototypes ensured the structural integrity of the heat exchanger core, with no deformation observed during the experiment.

Khalil et al. (2022) conducted a numerical and experimental investigation to study the thermohydraulic performance of three heat sinks with lattice topologies based on triply periodic minimal surfaces (TPMS). The TPMS heat sinks consisted of periodically arranged Diamante (D) or Gyroid (G) unit cells of 10 mm size and 80% porosity, with two topologies: solid and sheet networks. The proposed geometries were fabricated using the L-PBF additive manufacturing technique. CFD models were developed to study the heat sinks at a constant surface temperature by varying the Reynolds number (Re). The results showed that G-Sheet had the highest area convection heat transfer coefficient and the lowest thermal resistance, while D-Solid had the highest Nusselt number and thermal efficiency for a given pumping power. G-Solid exhibited the lowest friction factor due to the lowest surface area and largest pore size.

The study by Göltaş et al. (2022) presents a new compact plate heat exchanger (PHE) with a lung pattern surface geometry, produced by additive manufacturing using Direct Metal Laser Sintering (DMLS) method. The authors investigate the new PHE experimentally and numerically using water as the working fluid under single-phase cross-flow conditions. The results showed that the lung-patterned PHE outperformed the classical Chevron angle PHE in terms of heat transfer efficiency and pressure drop. The design created more turbulence than the classical PHE, and as the mass flow rate of the lung patterned PHE increases, the heat transfer and pressure drop also increase. The lung-patterned PHE showed 23% more efficiency compared to the classical PHE at the same flow rate and under the same conditions. The study suggests that the new PHE can reduce the number of plates and the volume of the PHE for the same amount of heat transfer in commercial PHEs.

2.2.2 PCHE

Due to the computational demand in modeling a complete PCHE, most of the studies published so far represent the core of the exchanger through a single heat exchanger unit, which can be composed of two or three channels (two hot channels and one cold or vice versa). The three main types of flow arrangements studied are cross-flow, parallel-flow, and counter-flow, as shown in Figure 5. Usually, the cross-section of the channel can be rectangular, circular, or semicircular. These channel types can be categorized as continuous (straight, zigzag, trapezoidal, and wavy channels) or discontinuous (S-shaped fin and airfoil channels) flow channels.

Figure 5 – Schematic diagram of flow arrangements and channels of PCHEs: (a) cross-flow; (b) parallel-flow; (c) counter-flow; (d) heat exchanger unit types.

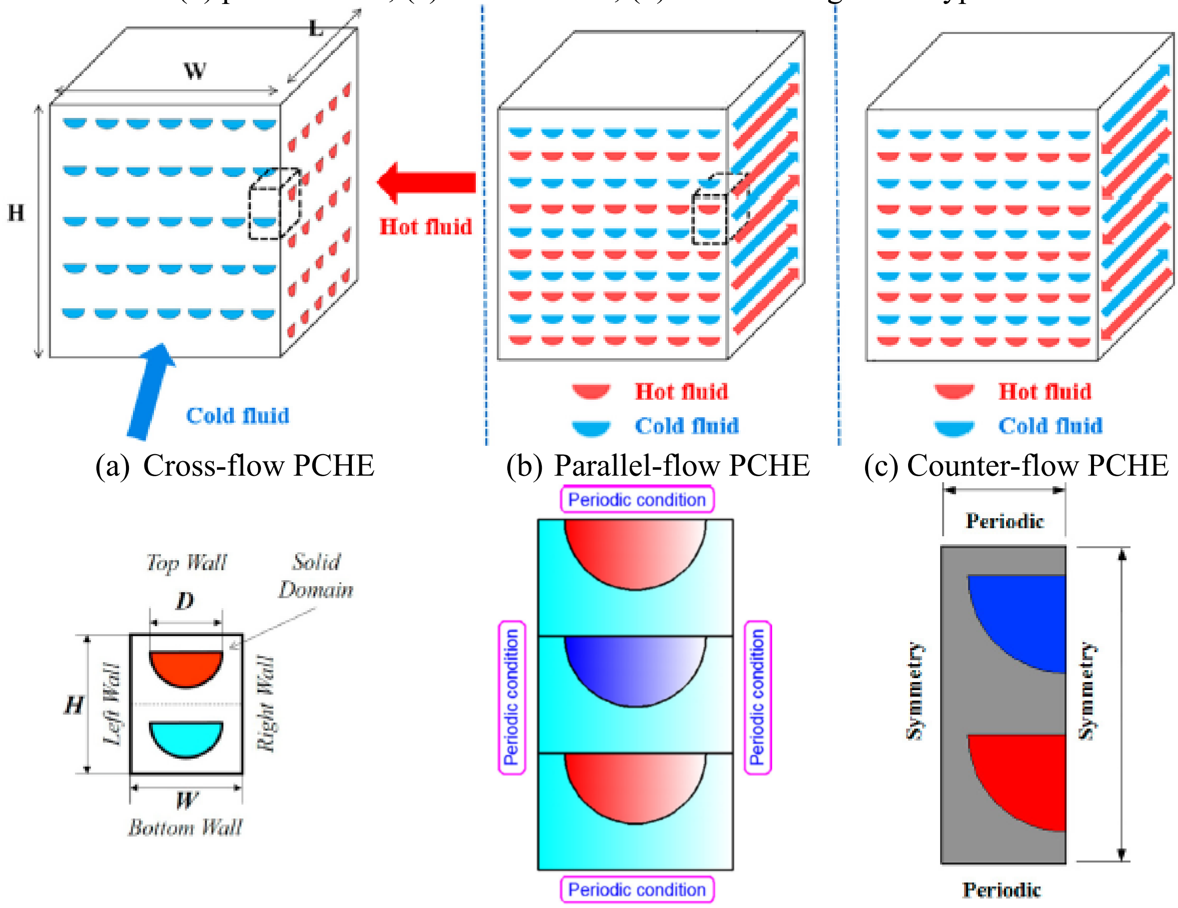

(c) Heat exchanger unit types

Source: Chai and Tassou (2019), Kim et al. (2017) and Ren et al. (2019).

Jeon et al. (2016) conducted a numerical analysis on the effect of channel cross-sectional shape and size on the thermal-hydraulic performance of a cross-flow PCHE manufactured in 304 stainless steel. A unit cell containing two straight semicircular channels, one with hot fluid and the other with cold fluid, represents the entire structure during numerical analysis. The study found that the thermal performance of the PCHE decreases uniformly as the channel size increases, with the size of the hot channel having a more significant impact on thermal performance than the size of the cold channel. The study also found that the channel cross-sectional shape has a negligible effect on thermal-hydraulic performance as long as the hydraulic diameter of the cross-section remains constant. However, the distance between the channels significantly affects the structural reliability of the PCHE. The study concluded that thermal performance and structural reliability must be carefully considered when designing the PCHE, and 1.8 mm was found to be the optimal channel size considering both factors.

Figley et al. (2013) presented a simplified PCHE model consisting of 10-hot and 10-cold side plates in counter-flow. The laminar-to-turbulent transition behavior has been numerically investigated for the circular and semicircular channel geometries, showing that the transition is observed at Reynolds numbers (*Re*) of 2,300 and 3,100, respectively. The velocity profiles for the fully developed region of the channels are shown in Figure 6. For *Re* above 3,200 both the semicircular and circular channels exhibit flat turbulent velocity profiles. The authors concluded that the performance of the numerical model is following the correlations and empirical models used in its evaluation. The thermal effectiveness of this laboratory scale model is low when compared to the 98% efficacy achieved in the literature data due to the straight channels employed in the design and the small heat transfer surface area of the PCHE.

Figure 6 – Velocity profiles for semicircular and circular channel shapes.

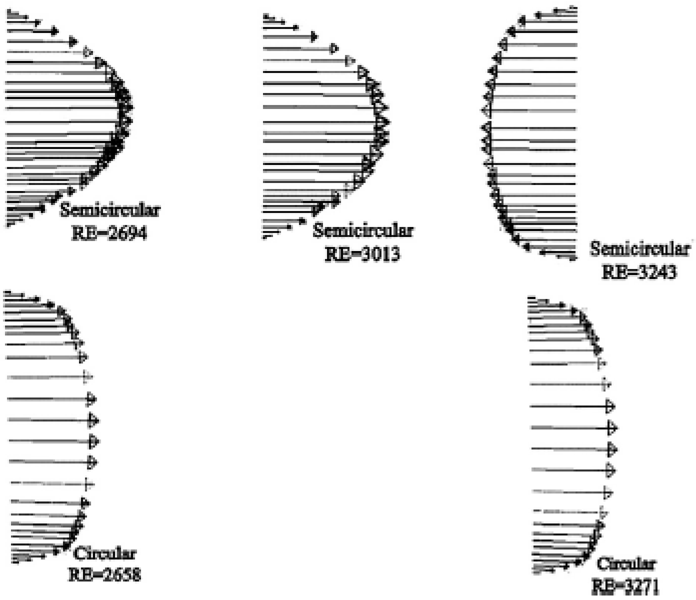

Source: Figley et al. (2013).

The studies indicated so far disregard the inlet and outlet headers, generally addressing the unit cell methodology composed of a limited number of channels. Header analysis is important when identifying whether and how fluid non-uniformity occurs in the exchanger channels. Chu et al. (2019) stands out by presenting, as to the effect of geometrical structure, an analysis of the flow non-uniformity in straight-channel PCHEs with different inlet headers, including rectangular inlet header (RIH), parabolic inlet header (PIH), trapezoidal inlet header (TIH) and hyperbolic inlet header (HIH). Based on the streamlined profile (see Figure 7), the HIH can effectively reduce the flow non-uniformity by 46% compared with the current practical manufactured model. Simultaneously, the improvement of flow uniformity by the novel inlet header may increase the overall performance by 39.5%. Furthermore, the effect of core length is also investigated, and it is found that the flow non-uniformity can be minimized by varying the core length. The result shows that the flow non-uniformity can be expressed as a function of the shape factor and dimensionless core length.

Figure 7 – Streamline schematic of PCHE with four different inlet headers (Re_{in} = 2.89×10^5).

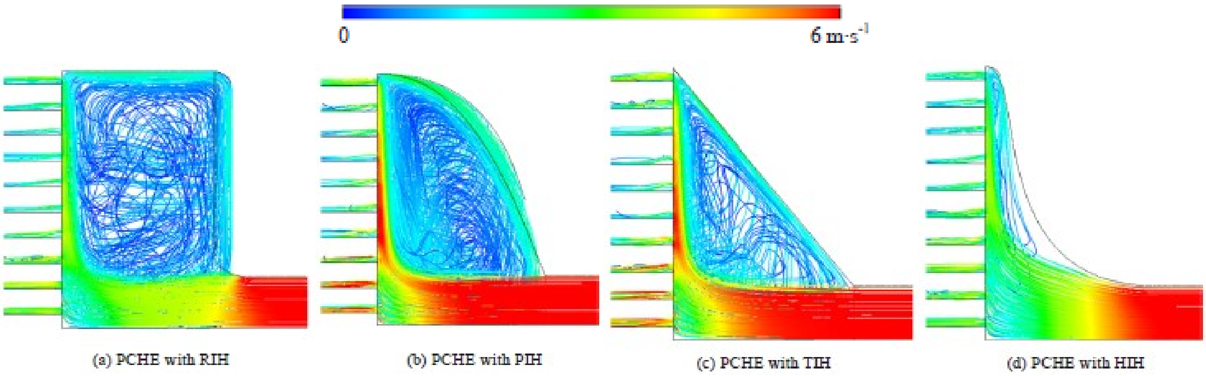

Source: Chu et al. (2019).

From the literature review, a lot of experimental, theoretical, and numerical investigations have been conducted on the thermal-hydraulic performance and optimization of PCHE, and various new types of structures and configurations have been developed (JING; XIE; ZHANG, 2020). The straight channel is the basic channel type, but to improve the thermal-hydraulic performance of the PCHE, zigzag, wavy, S-shaped fin and airfoil channels have been proposed. Studies with new channel configurations are also being conducted, in a more timid way.

According to White et al. (2020), despite the superior heat transfer performance in PCHEs with non-straight channels, a major problem associated with them is the large pressure drop, due to longer flow passages and complicated channel geometry. Another important issue is related to the pinch point, which leads to a minimum heat transfer rate, where two heat exchangers are employed to optimize the capital and operating costs. Lastly, cleaning PCHEs is complicated due to a welded body from the core to the header, for this reason, it is advisable to employ PCHEs within a limited fouling environment, or to at least use strainers.

Liu et al. (2020) provide a comprehensive overview of the heat transfer and pressure drop of Printed Circuit Heat Exchangers (PCHEs) in the SCO_2 Brayton cycle. The authors discuss the industrial feasibility and maturity level of PCHEs with various channel types and cross-sections, including semicircular, rectangular, triangular, circular, elliptical, and sinusoidal. They note that only the semicircular cross-section can be easily obtained through the chemical etching process. The authors suggest that the zigzag channel is the most appropriate channel type for the SCO_2 side, but its pressure drop needs to be optimized through geometric and operating parameter adjustments. The study also highlights that the airfoil and S-shaped fin channels show excellent pressure drop performance, but their high cost and low maturity level confine them to the laboratory. For large-scale applications, reducing the manufacturing cost of PCHEs is crucial because the cost of chemical etching significantly contributes to the overall cost.

Among the literature review studies performed, Chai and Tassou (2020) provides a review of PCHEs, covering material selection, manufacturing and assembly, types of flow passages, thermohydraulic performance, heat transfer and pressure drop correlations, as well as geometric design optimization methods. And they classify that, in general, PCHEs with airfoil fins showed best performance, followed by S-shaped fins and zigzag (or wavy) channel PCHEs.

Huang et al. (2019) summarizes relevant researches on the characteristics and correlations of flow and heat transfer for PCHEs. Some existing problems are presented, for example, boundary conditions in numerical simulations, low Reynolds number flow in experiments, only single-phase flow with SCO_2 or helium as working fluid, etc. Concluding that PCHEs with semicircular zigzag channels have been widely accepted as the most cost-effective configuration. Table 15 in APPENDIX A presents a summary of the papers found, describing the geometry configurations, working conditions, and the attained results.

From the works cited, a few important points related to the present work can be summarized:

a) The manufacturing technique fails to provide always the same manufacturing parameters resulting in small differences in each piece manufactured such as varying relative roughness of the surfaces and small uncertainties in the channels diameters;
b) The thermo-hydraulic performance for different channel shapes with the same hydraulic diameter is equivalent, however, the distance between channels greatly affects the structural behavior of the core;
c) The nozzle connections are important for the modeling of the non-uniformity of the flow through the core of the heat exchanger;
d) Although some works present different channels geometries the more commonly used are straight channels with circular and semicircular shapes;

e) For flow inside circular channels the transition Reynolds for turbulent flow is 2300 while for semicircular channels it is 3100.

The justification for the numerical model to be presented in Chapter 4 is based on items (c), (d) e (e) while items (a) and (b) will be discussed in more detail in the Results sections, Chapter 5.

2.2.3 Chaotic Channels

According to the research experience on the thermal-hydraulic performance of heat exchangers, corrugated or chaotic channels can effectively annul the flow boundary layer and consequently enhance heat transfer. With this purpose, Lasbet et al. (2007) conducted a numerical study to evaluate the thermal-hydraulic performance of different channel formats (Figure 8) in a PEMFC system. The study compared the performance of four different geometries (C-shape, V-shape, B-shape, and straight channel) in terms of heat transfer efficiency, thermal mixing properties, and pressure drops. Two Reynolds numbers (100 and 200) were considered, and water was used as the working fluid. The C-shape and V-shape channels were found to be the most effective in enhancing heat transfer, with the C-shape channel showing the greatest enhancement due to its chaotic flow behavior. The V-shape channel was designed to reduce pressure drop and showed the best balance between convective heat transfer and reasonable pressure drop. The B-shape geometry, designed to reduce machining costs, had thermal and hydraulic performances similar to those of the V-shaped geometry. All the chaotic geometries showed similar mixing ratios for the two Reynolds numbers studied.

Figure 8 – Geometries studied.

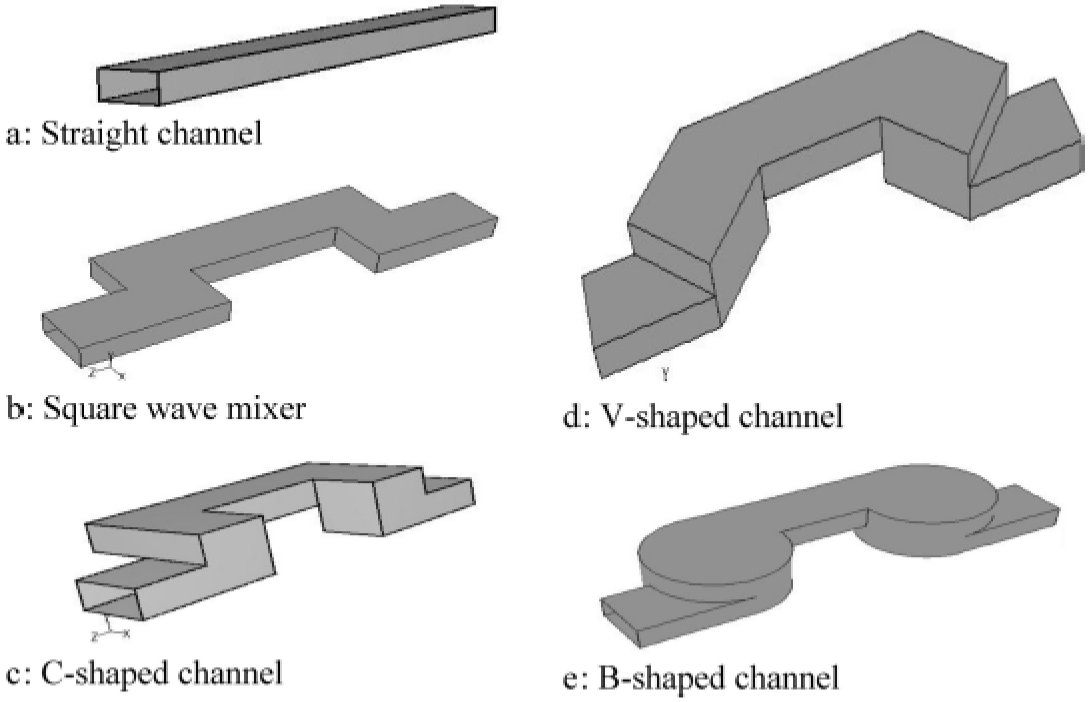

Source: Lasbet et al. (2007).

Continuing previous work, Castelain et al. (2016) conducted an experimental study to improve the thermal performance of heat exchangers used in the bipolar plates of PEM fuel cells. The study compared the performance of two chaotic advection geometries (C-shape and V-shape) and a straight rectangular tube. The geometries were evaluated using numerical simulations and the V-shape and C-shape channels were found to have the best thermal characteristics. These were then studied experimentally, with the straight tube as a reference. The efficiency of all three geometries decreased with increasing Reynolds number due to shorter residence time and higher fluid temperature difference between inlet and outlet at higher flow rates. The C-shape channel had the highest efficiency and overall heat transfer coefficient, which may be due to the significant number of chaotic zones in this geometry compared to the V-shaped channel. The study concluded that three-dimensional geometry is capable of inducing chaotic advection without the need to increase the heat exchanger area.

3 NUMERICAL METHOD

This study employs Computational Fluid Dynamics (CFD), a computer-based tool that simulates fluid flow, heat transfer, and related physical processes. The CFD method solves fluid flow equations over a region of interest with specified boundary conditions. The identification of unique flow physics and fluid used within the flow domain is critical in solving such equations. To facilitate understanding, Figure 9 presents a flow chart highlighting the various flow physics found within the CFD framework and heat transfer processes, as stated by Tu, Yeoh, and Liu (2018).

Figure 9 – Flowchart encapsulating the flow physics in CFD.

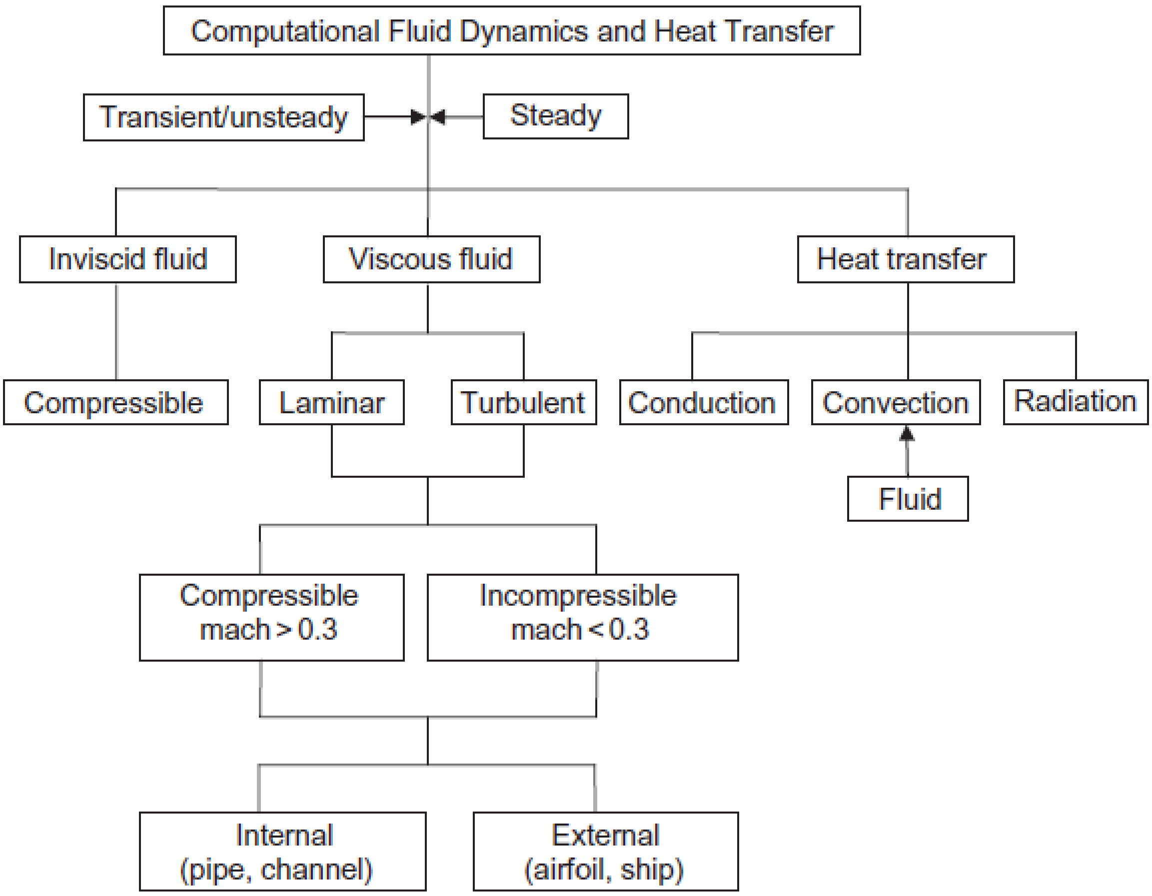

Source: Tu, Yeoh and Liu (2018).

3.1 DISCRETIZATION OF GOVERNING EQUATIONS

CFD is fundamentally based on the governing equations of fluid dynamics. The set of equations involved in fluid dynamics describes the conservation of mass, momentum, and energy and are known as the conservation equations. They are partial differential equations and have no analytical solutions except for very simplified situations, but can be discretized to be solved numerically in full. Therefore, CFD is the process of converting the partial differential equations of fluid dynamics into simple algebraic equations and then solving them numerically to obtain a meaningful result (JAMSHED, 2015).

The most popular discretization approaches in CFD are finite-difference (FDM) and finite-volume (FVM) methods. Figure 10 illustrates the overview process of the computational solution procedure.

Figure 10 – Overview process of the computational solution procedure.

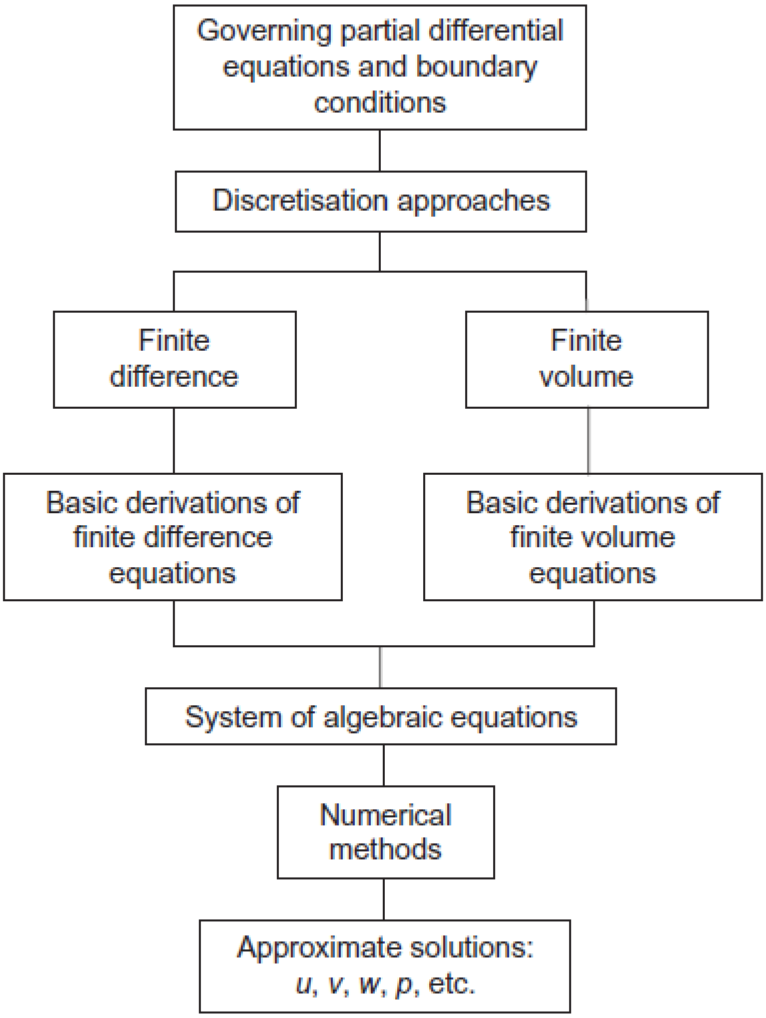

Source: Tu, Yeoh and Liu (2018).

The finite-volume method and its variations are employed in the majority of all commercial CFD codes today, including the software used in this study (ANSYS CFX – The Finite Volume Method – see details of the method in Maliska (2012)). In this method, the region of interest is divided into small subregions, called control volumes. All governing equations are discretized and solved iteratively for each control volume taking into account the interface with other volumes neighboring the analysis volume in the computational mesh. As a result, an approximation of the value of each variable at specific points in the domain can be obtained. And in this way, it is possible to obtain a complete representation of the flow behavior.

As the FVM works with control volumes and not the grid intersection points, it has the capacity to accommodate any type of grid (structured and unstructured mesh, see Figure 11). Structured grid is usually designated as a mesh containing cells having either a regular-shape element with four nodal corner points in two dimensions or a hexahedral-shape element with eight-nodal corner points in three dimensions. In this type of grid, the number of interfaces between volume elements is regular throughout the domain. Unstructured mesh commonly refers however to a mesh overlaying with cells that are in the form of either a triangle-shape element in two dimensions or a tetrahedron-shape element in three dimensions. In this type of grid there is no regularity in the number of interfaces (TU; YEOH; LIU ,2018).

Figure 11 – A representation of structured and unstructured mesh for FVM (full symbols denote element vertices, and open symbols at the center of the control volumes denote computational nodes).

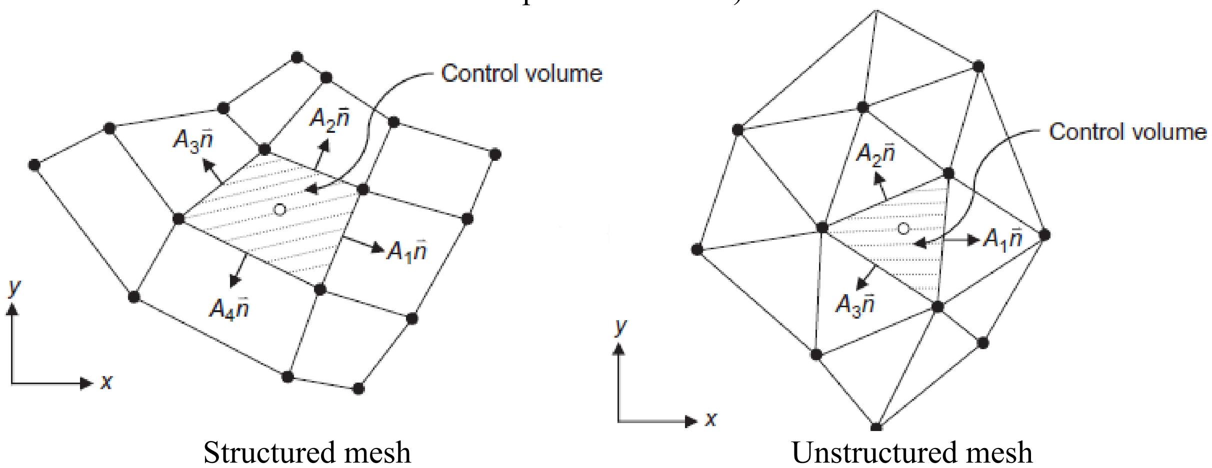

Source: Adapted from Tu, Yeoh and Liu (2018).

According to Tu, Yeoh and Liu (2018), in a control volume, the bounded surface areas of the element are directly linked to the discretization of the first and second order derivatives for ϕ (the generic flow field variable). Figure 11 indicates that the surface areas in the normal ($\vec{n}$) direction to the volume surfaces are resolved with respect to the Cartesian coordinate directions to yield the projected areas A_i^x and A_i^y in the x and y directions, respectively.

3.2 TURBULENCE MODELING

There are two qualitatively different types of viscous fluid flows: laminar and turbulent. The solution of the Navier-Stokes equations does not raise any fundamental difficulties in the case of laminar flows but presents a significant challenge in the case of turbulent flows. Turbulence occurs when the inertial forces of the fluid become significant compared to the viscous forces and is characterized by a high Reynolds number.

Blazek (2015) says that the turbulence regime can be treated utilizing approximations through three turbulence models which have four levels of precision of resolution (decreases as the level grows), shown in Figure 12.

Figure 12 – Hierarchy of turbulence models.

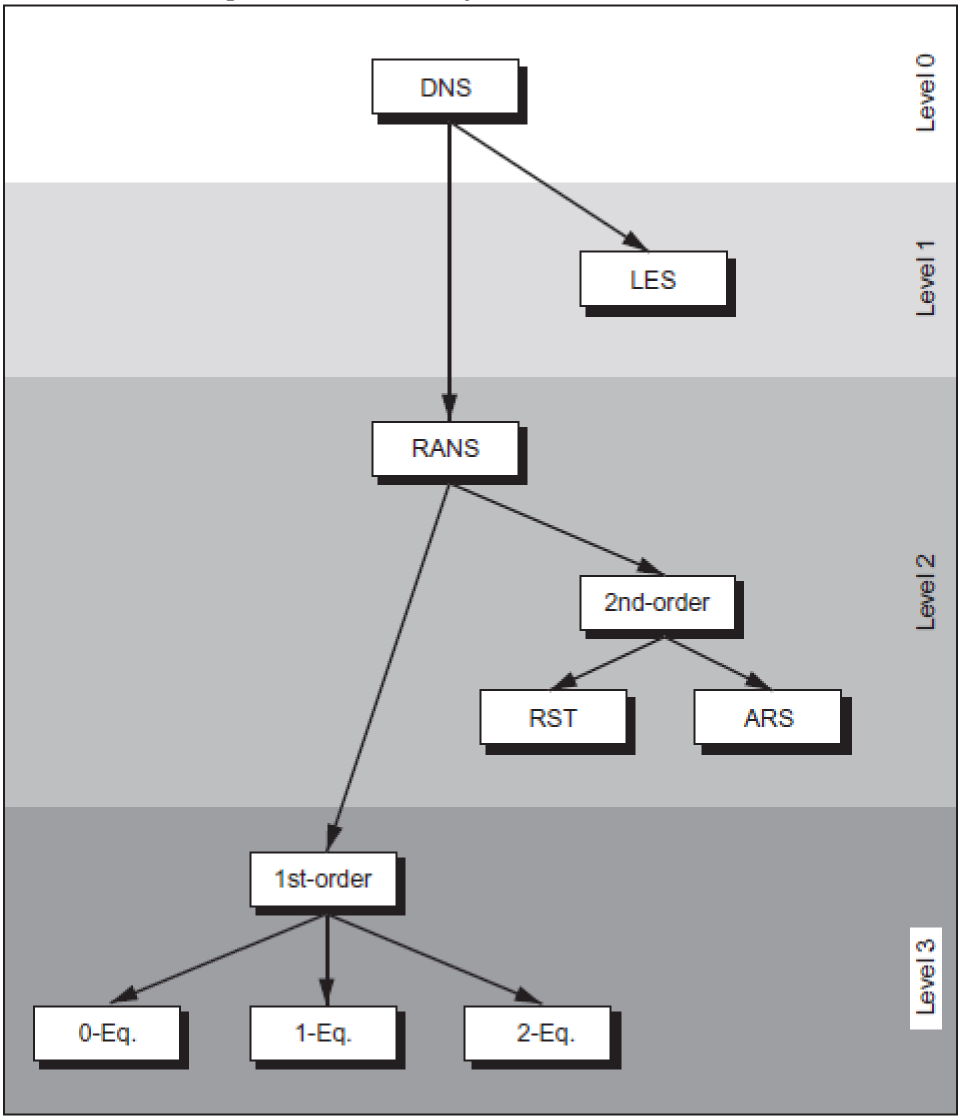

Source: Blazek (2015)

In other words, the models indicated by level 0 are the most complete, and level 3 are the most simplified. In ascending order, the Direct Numerical Simulation (DNS) belongs to level 0 and despite being the most accurate, it requires a lot of computational demand; in level 1 is the Large-Eddy Simulation (LES) which models the biggest fluctuations; the Reynolds-Averaged Navier-Stokes (RANS) of 2nd order it's in the level 2 and is divided in two types: Reynolds-Stress Transport (RST) and Algebraic Reynolds-Stress (ARS) models; and in the level 3 is the RANS of 1st order which is separated in three categories: 0-, 1-, 2-Eq., with zero-(algebraic), one-or two-equations models. The models classified in this last level are based on the Boussinesq turbulent viscosity hypothesis and they are solved from the Reynolds averages concept, using the mean Reynolds equations applied to Navier-Stokes (RANS). The RANS assumes a completely turbulent flow and takes only the average of the fluctuations.

Although the LES turbulence model allows considerably more accurate predictions of turbulent flows, it remains computationally very demanding. On the other hand, the RANS equations offer a relatively simple way to model turbulence.

In this study, the Navier-Stokes equations are solved numerically with a finite volume method on a structured grid using the ANSYS CFX commercial software. To model turbulence, the Shear Stress Transport (SST) model — which belongs to the class of 2 equations RANS models — was used. This model uses the Reynolds-Average in the Navier-Stokes equations and accounts for the effects of turbulent fluctuation directly on an averaged flow. The variables present in the governing equations (components of velocity, pressure, temperature, and other transported quantities) are rewritten using Reynolds decomposition, where an instantaneous property ϕ is expressed by the sum of a time-averaged part $\bar{\phi}$ and its fluctuation ϕ', as introduced below:

$$\phi = \bar{\phi} + \phi', \tag{1}$$

The air was idealized as an ideal gas and the water as incompressible, with the fluid properties ρ, μ, c_p, and λ constant (independent of the fluid temperature), and steady-state condition was considered. The incompressible (concerning the pressure) Navier-Stokes equations subjected to the Reynolds-averaging procedure result in the following relations for the mass and momentum conservation:

$$\frac{\partial}{\partial x_i}(\bar{u}_i) = 0, \tag{2}$$

$$\frac{\partial}{\partial t}(\rho\bar{u}_i) + \frac{\partial}{\partial x_j}(\rho\bar{u}_j\bar{u}_i) = -\frac{\partial\bar{p}}{\partial x_i} + \frac{\partial}{\partial x_j}(2\mu\bar{S}_{ij} - \tau_{ij}^R), \tag{3}$$

$$\bar{S}_{ij} = \frac{1}{2}\left(\frac{\partial\bar{u}_i}{\partial x_j} + \frac{\partial\bar{u}_j}{\partial x_i}\right), \tag{4}$$

$$\tau_{ij}^R = -\rho\overline{u_i'u_j'}\ . \tag{5}$$

where t is the time, $\bar{u}$ is the time-averaged velocity, $\bar{p}$ is the time average static pressure, $\bar{S}_{ij}$ is the mean strain-rate tensor and τ_{ij}^R is the Reynolds-stress tensor. The last one represents, mathematically the effects of fluctuations on the mean fluid flow and physically the rate of transfer of momentum arising from the fluctuation of the velocity of the fluid.

The Reynolds-stress tensor consists of a matrix of the nine components:

$$\rho\overline{u_i'u_j'} = \begin{bmatrix} \rho\overline{(u_1')^2} & \rho\overline{u_1'u_2'} & \rho\overline{u_1'u_3'} \\ \rho\overline{u_2'u_1'} & \rho\overline{(u_2')^2} & \rho\overline{u_2'u_3'} \\ \rho\overline{u_3'u_1'} & \rho\overline{u_3'u_2'} & \rho\overline{(u_3')^2} \end{bmatrix}, \tag{6}$$

Since u_i' and u_j' in the correlations can be interchangeable, the Reynolds-stress tensor contains only six independent components. Thus, the turbulent kinetic energy is defined by the sum of the normal stresses divided by the density:

$$K = \frac{1}{2}\overline{u_i'u_i'} = \frac{1}{2}\left[\overline{(u_1')^2} \quad \overline{(u_2')^2} \quad \overline{(u_3')^2}\right]. \tag{7}$$

3.3 SHEAR STRESS TRANSPORT MODEL (SST)

The Reynolds-Averaged Navier-Stokes (RANS) equations are solved alongside the Shear Stress Transport (SST) turbulence model. The SST model is described by Menter, Esch and Konno (2003) as a combination of the k–ω model (applied for the region adjacent to the wall) and the k–ε model (applied for the remainder of the flow) aiming to achieve a formulation with adverse pressure gradient flow applications close to walls. This approach allows using the attractive performance near the wall of the k–ω model without the possible errors arising from free flow, common in this method. The equations modeled for the turbulent kinetic energy K and the turbulence frequency ω are shown below:

$$\frac{\partial\rho K}{\partial t}+\frac{\partial\rho\bar{u}_j K}{\partial x_j}=\frac{\partial}{\partial x_j}\left[\left(\mu_L+\sigma_K\mu_T\right)\frac{\partial K}{\partial x_j}\right]+\tau_{ij}^F\bar{S}_{ij}-\beta^*\rho\omega K, \tag{8}$$

$$\frac{\partial\rho\omega}{\partial t}+\frac{\partial\rho\bar{u}_j\omega}{\partial x_j}=\frac{\partial}{\partial x_j}\left[\left(\mu_L+\sigma_\omega\mu_T\right)\frac{\partial\omega}{\partial x_j}\right]+\frac{C_\omega\rho}{\mu_T}\tau_{ij}^F\bar{S}_{ij}-\beta\rho\omega^2+2(1-f_1)\frac{\rho\sigma_{\omega2}}{\omega}\frac{\partial K}{\partial x_j}\frac{\partial\omega}{\partial x_j}, \tag{9}$$

$$\tau_{ij}^F=\frac{-\bar{\rho}\overline{u_i^{"}u_j^{"}}}{\partial x_j}. \tag{10}$$

where the τ_{ij}^F is the Reynolds-averaged turbulent stresses; f_1 is the blending function and this function is then equal to 1 near the solid surface and equal to 0 for the flow domain away from the wall. The blending function is calculated as:

$$f_1=\tan h(arg_1^4), \tag{11}$$

$$arg_1=\min\left[\max\left(\frac{\sqrt{k}}{\beta^*\omega y},\frac{500\mu_L}{\rho\omega y^2}\right),\frac{4\rho\sigma_{\omega2}K}{CD_{K\omega}y^2}\right], \tag{12}$$

where y is the distance to the wall and $CD_{K\omega}$ is the positive portion of the cross-diffusion term, given as:

$$CD_{K\omega}=\max\left(2\frac{\rho\sigma_{\omega2}}{\omega}\frac{\partial K}{\partial x_j}\frac{\partial\omega}{\partial x_j},10^{-20}\right). \tag{13}$$

The turbulent viscosity and the dynamic viscosity coefficient (in the viscous stress tensor) are defined, respectively, as:

$$\mu_T=\frac{a_1\rho K}{max(a_1\omega,f_2\|curl\vec{u}\|_2)}, \tag{14}$$

$$\mu=\mu_L+\mu_T. \tag{15}$$

where the auxiliary function f_2 is given by:

$$F_2=\tan h(arg_2^2), \tag{16}$$

$$arg_2=\max\left(2\frac{\sqrt{k}}{\beta^*\omega y},\frac{500\mu_L}{\rho\omega y^2}\right). \tag{17}$$

The model constants are as follows:

$$a_1 = 0.31, \qquad \beta^* = 0.09, \qquad K = 0.41. \tag{18}$$

The blending functions are used to calculate the constants as presented below:

$$\emptyset = f_1\emptyset_1 + (1 - f_1)\emptyset_2, \tag{19}$$

where $\emptyset_1$ and $\emptyset_2$ are respectively, the coefficients of the models k–ω and k–ε. The coefficients of the inner model (k−ω) are given by:

$$\sigma_{K1} = 0.85, \qquad \sigma_{\omega 1} = 0.5, \qquad \beta_1 = 0.075, \qquad C_{\omega 1} = \frac{\beta_1}{\beta^*} - \frac{\sigma_{\omega 1} K^2}{\sqrt{\beta^*}} = 0.533. \tag{20}$$

and the coefficients of the outer model (k−ε) are defined as:

$$\sigma_{K2} = 1.0, \qquad \sigma_{\omega 2} = 0.856, \quad \beta_2 = 0.0828, \quad C_{\omega 2} = \frac{\beta_2}{\beta^*} - \frac{\sigma_{\omega 2} K^2}{\sqrt{\beta^*}} = 0.440. \tag{21}$$

The boundary conditions for the kinetic turbulent energy and the specific dissipation at solid walls are:

$$K = 0, \qquad \omega = 10\frac{6\mu_L}{\rho\beta_1(y_1)^2}. \tag{22}$$

with y_1 being the distance of the first node (cell centroid) from the wall. The grid has to be refined such that $y^+ < 3$ is satisfied. All details of calculations can be found in Blazek (2015).

3.4 WALL TREATMENT

The turbulent flows are significantly affected by the presence of walls and turbulence itself is altered, in different ways, by its presence. Since the average velocity field is affected by the no-slip condition that needs to be satisfied on the wall. The region near the wall, for a turbulent flow developed without adverse pressure gradient, can be fragmented into three layers: the innermost layer (viscous sublayer), where the flow is almost laminar, and the molecular viscosity plays a dominant role in momentum transport and heat or mass transfer;

the outer layer (turbulent layer) whose turbulence plays an important role, with turbulent flow effects predominating; and the intermediate region between the viscous sublayer and the fully turbulent layer (log layer), where the effects of molecular viscosity and turbulence are equally important. Figure 13 illustrates these subdivisions of the region near the wall, plotted in semi-logarithmic coordinates (TASCHECK, 2019) and (WILCOX, 2006).

Figure 13 – Typical velocity profile for a turbulent boundary layer.

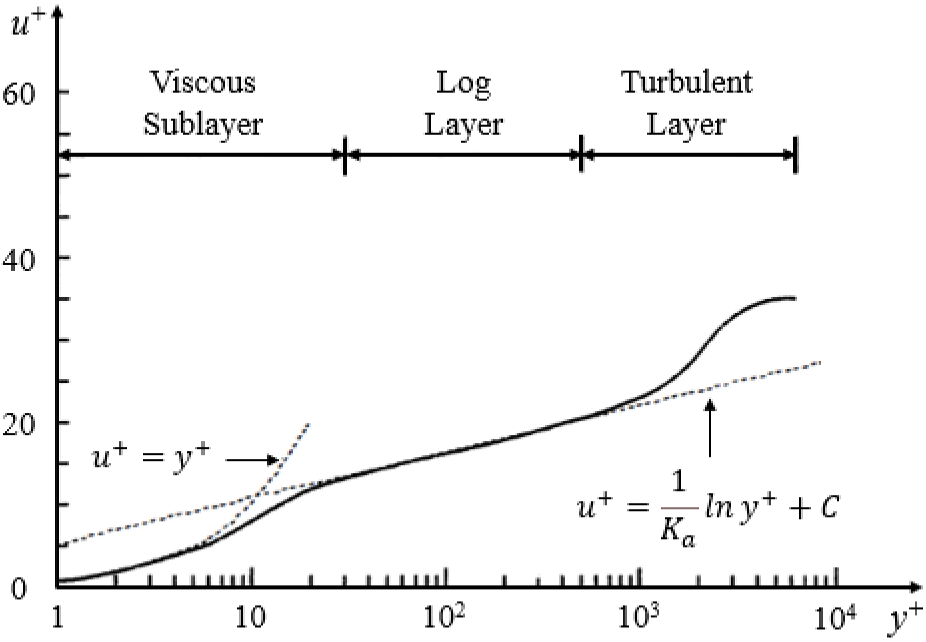

Source: Adapted from Wilcox (2006).

According to Wilcox (2006), the semi-empirical formulas are utilized to model the area affected by the wall, connecting the regions influenced by the viscosity between the wall and the fully turbulent region. Therefore, the non-dimensional velocity close to the wall (hydrodynamic wall law) is calculated from:

$$u^+ = \frac{1}{K_a} ln\, y^+ + C, \tag{23}$$

where K_a is the Kármán constant ($K_a = 0.41$), C is a generic integration constant ($C \approx 5$), and y^+ is the non-dimensional distance between the point (y) and the wall, calculated from:

$$y^+ = \frac{u^* y}{\nu}, \tag{24}$$

where ν is the kinematic viscosity and the u^* is the friction velocity:

$$u^* = \sqrt{\frac{\tau_\omega}{\rho}}, \tag{25}$$

To resolve the viscous sublayer inside the turbulent boundary layer, y^+ at the first node adjacent to the wall should be set preferably near unity ($y^+ = 1$). However, a higher y^+ is acceptable as long as it is still well within the *viscous sublayer* ($y^+ = 4\ or\ 5$). Depending on the Reynolds number, one must ensure that there are between 5 and 10 grid nodal points between the wall and the location where $y^+ = 20$ which is within the viscosity-affected near-wall region to solve mean velocity and turbulent quantities (TU; YEOH; LIU, 2018).

Similarly to velocity, temperature also receives wall treatment. The boundary layer is subdivided into a thermal conduction sublayer and a logarithmic sublayer for the region where the effects of turbulence are predominant over conduction. Therefore, the thermal wall law is denominated:

$$T^+ = \frac{1}{K_{aT}} ln\, y^+ + C_T Pr, \tag{26}$$

where Pr is Prandtl's number and $C_T Pr$ is a function of the molecular Pr of the fluid. In the laminar sublayer, Prandtl's number can be defined by:

$$\mathrm{Pr} = \frac{T^+}{y^+} = \frac{T^+}{u^+}, \tag{27}$$

$$T^+ = \frac{T - T_w}{T^*}, \qquad T^* = \frac{\dot{q}_w''}{\rho C_p u^*}, \qquad \dot{q}_w'' = k\frac{T - T_w}{y}, \qquad Pr = \frac{\nu}{\alpha} = \frac{\nu \rho C_p}{k}. \tag{28}$$

where q_w is the heat flow at the wall (W/m^2), y is the distance from the surface and ρ, μ and k are density, viscosity and thermal conductivity, respectively.

For the development of this work, the SST model with the automatic wall treatment was chosen. This combination explores the robust formulation for the viscous sublayer but requires a more refined mesh near the wall compared to the other wall functions.

The calculation procedures used to evaluate the thermal performances and pressure loss are presented below.

3.5 GLOBAL PARAMETERS

The nondimensional parameter that characterizes the flow regime is the Reynolds number (Re). Depending on the fluid conditions, the flow in a duct can be in a laminar, transitional, or turbulent regime (SHAH; SEKULIC, 2003). For non-circular pipe flow, the Reynolds number as well as the other correlations are based on the hydraulic diameter (KAKAÇ; LIU; PRAMUANJAROENKIJ, 2012). As different cross-section shapes are studied in this paper, this will be the adopted formulation.

For flow in a non-circular tube, the Reynolds number is defined as:

$$Re = \frac{\rho u_m D_h}{\mu}, \tag{29}$$

where ρ is the fluid density, u_m is the average velocity, D_h is the hydraulic diameter of the channels of the heat exchanger and μ is the dynamic viscosity of the fluid. The hydraulic diameter D_h is given by:

$$D_h = \frac{4 \times channel\,flow\,area}{wetted\,perimeter}, \tag{30}$$

The Nusselt number (Nu) is a dimensionless number used to measure the efficiency of convective heat transfer. Thus, the greater the number of Nu, the more effective the convective heat transfer will be (SHAH; SEKULIC, 2003). The thermal performance of the fluid flow for one channel of the heat exchanger is here defined by:

$$Nu = \frac{\varphi}{T_w - T_{in}} \frac{D_h}{\lambda}, \tag{31}$$

where φ is the heat flux on the channel surface, D_h is the hydraulic diameter, λ the thermal conductivity of the fluid, T_w is the wall averaged temperature, and T_{in} is the inlet flow temperature in the analyzed section. The same equation is applied for the analysis of Nu for the individual channels. Table 16 in APPENDIX A presents Nu correlations found in the literature for the different channel configurations based on experimental data.

The Fanning friction factor (f) relates pressure drop and fluid viscous effects. And its use allows pressure drop estimation of different flow lengths of the heat exchanger surface (SHAH; SEKULIC, 2003). Darcy's friction factor (f_D) is related to Fanning's friction factor and since f is the ratio between the shear stress at the wall and the kinetic energy of the flow per unit volume, f_D for a channel of the heat exchanger is represented by:

$$f_D = 4f = 4\left(\frac{2\tau_w}{\rho u_m^2}\right) = \frac{8\tau_w}{\rho u_m^2}, \tag{32}$$

where τ_w is the wall shear stress. It can also be described as:

$$f_D = \Delta p\left(\frac{D_h}{L}\right) = -\left(\frac{dp}{ds}\right)\frac{D_h}{\frac{1}{2}\rho U_m^2}, \tag{33}$$

where $\frac{dp}{ds}$ is the local pressure gradient along the channel. Table 16 in APPENDIX A presents the f correlations found in the literature for different channel configurations based on experimental data. Both the friction factor and the Nusselt number are strongly dependent on the thermal boundary conditions and the geometry of the flow path.

For all types of fully developed internal flow such as laminar or turbulent flow in a circular or non-circular pipe, smooth or rough surfaces, and horizontal or inclined pipes, the pressure drop can be expressed as (ÇENGEL, 2007):

$$\Delta p = f\,\frac{L}{D_h}\frac{\rho u_m^2}{2}, \tag{34}$$

where L is the length of the duct.

Validation comparisons for all results presented in this work are based on the percent relative error defined as:

$$Difference\ \% = \left|\frac{c^{ref} - c^{i}}{c^{ref}}\right| \times 100. \tag{35}$$

where the superscript ref indicates the reference value (experimental or analytical data) and the superscript i refers to the numerically simulated values of the cases being compared.

4 METHODOLOGY

The methodology used in this study is known as Computational Fluid Dynamics (CFD), based on discretizing the computational domain into a finite number of elements and applying a suitable numerical method to solve the problem. The present study was performed with the support of the commercial software ANSYS CFX 18.2 to evaluate the thermo-hydraulic performance of the heat exchanger manufactured by SLM (SLMHE). A summary of the applied CFD methodology is shown in Figure 14, where the blue gradient represents the pre-processing, processing, and post-processing steps, respectively.

Figure 14 – CFD methodology flowchart.

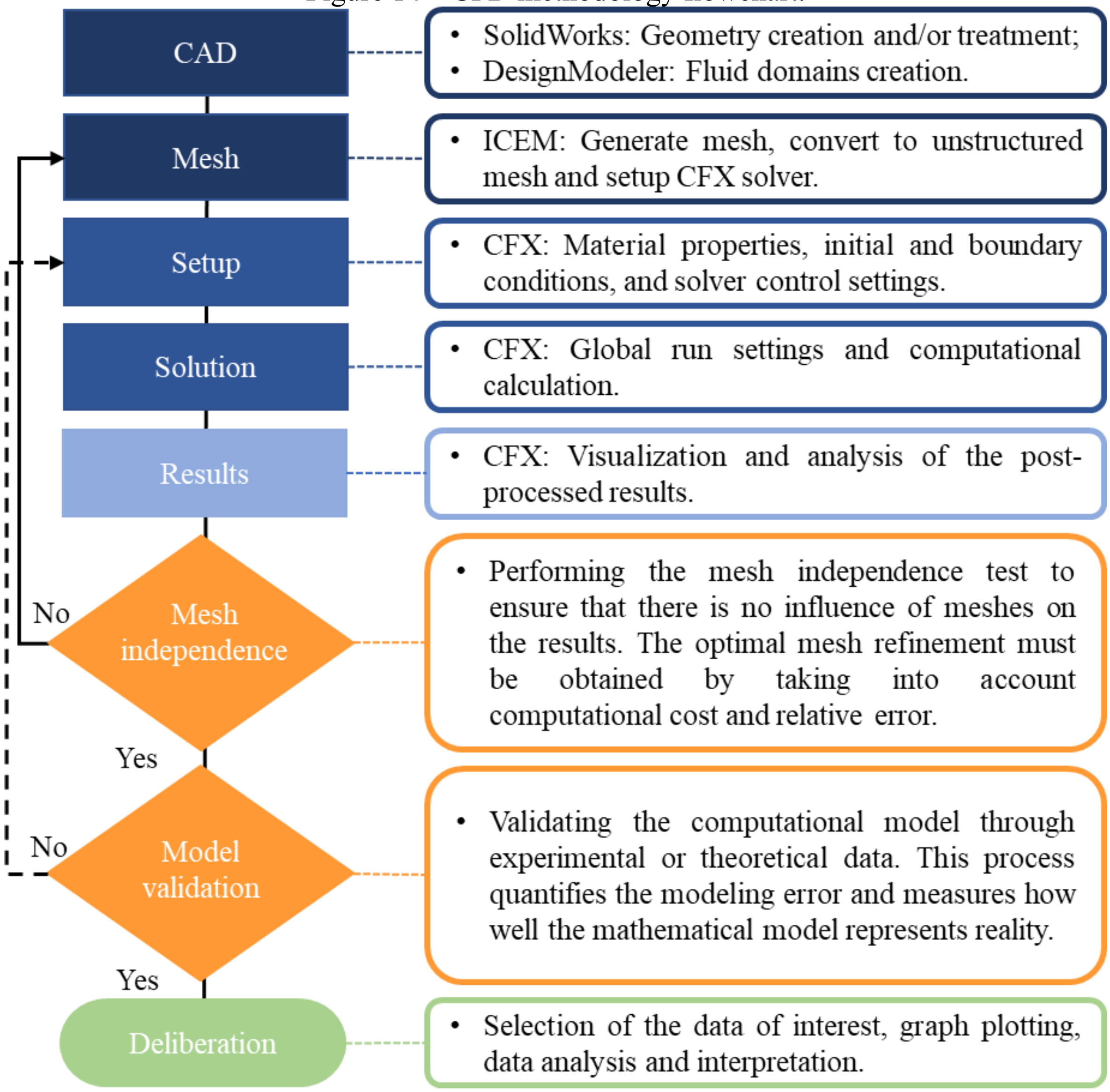

Source: Author (2022).

All CAD geometries were modeled with the software SolidWorks and the ANSYS DesignModeler was used to adjust the geometries (geometric simplification) and create the fluid domains. The volumes were meshed using hexahedral and wedge-shaped elements using ANSYS ICEM.

In more detail, the methodology of the present work consists of the following steps:

1) Development of two numerical models for Compact Heat Exchanger: the first model is the numerical model of the entire heat exchanger studied by Silva et al. (2021), an SLMHE manufactured Compact Heat Exchanger with mini straight circular channels. The second model is a variation of the first model where only the core is modified to represent straight semicircular channels with the same hydraulic diameter and same heat transfer area;
2) Development of four numerical models for individual channels of different cross-section geometries: straight circular, straight deformed circular, straight semicircular, and chaotic circular inclined V-shaped. Keeping the same hydraulic diameter and channel length of the complete heat exchanger;
3) Mesh refinement analysis for the six models;
4) Validation for the circular channel model through experimental data available in Silva et al. (2021);
5) Identification of possible causes of discrepancies between experimental data and circular channel model;
6) Comparison of results between circular channel model and semicircular channel model;
7) Study of the effects of the channel cross-section geometry on heat transfer rate and pressure drop in the individual channels.

The description of the computational domains, resolution mesh, and boundary conditions are shown in the following subsections.

4.1 CIRCULAR AND SEMICIRCULAR CHANNEL GEOMETRIES

4.1.1 Computational Domain

Figure 15 presents the geometry of the analyzed heat exchanger. For the actual equipment, the core of the heat exchanger was manufactured by the SLM method with a chessboard-like technique with gas-atomized AISI316L metallic powder. The core is a square with edges of 100 mm and has two branches, hot and cold, with 171 and 190 channels, respectively. The circular cross-section channels are 1.83 mm (cold branch) and 1.70 mm (hot branch) in diameter (d), the distance between the centers of the channels (p) is 2.5 mm, and the distance between layers (e) is 0.67 mm (cold branch) and 0.80 mm (hot branch).

Figure 15 – Geometric parameter of the core with circular (a) and semicircular (b) channels, and nozzle (c) (all dimensions are in mm).

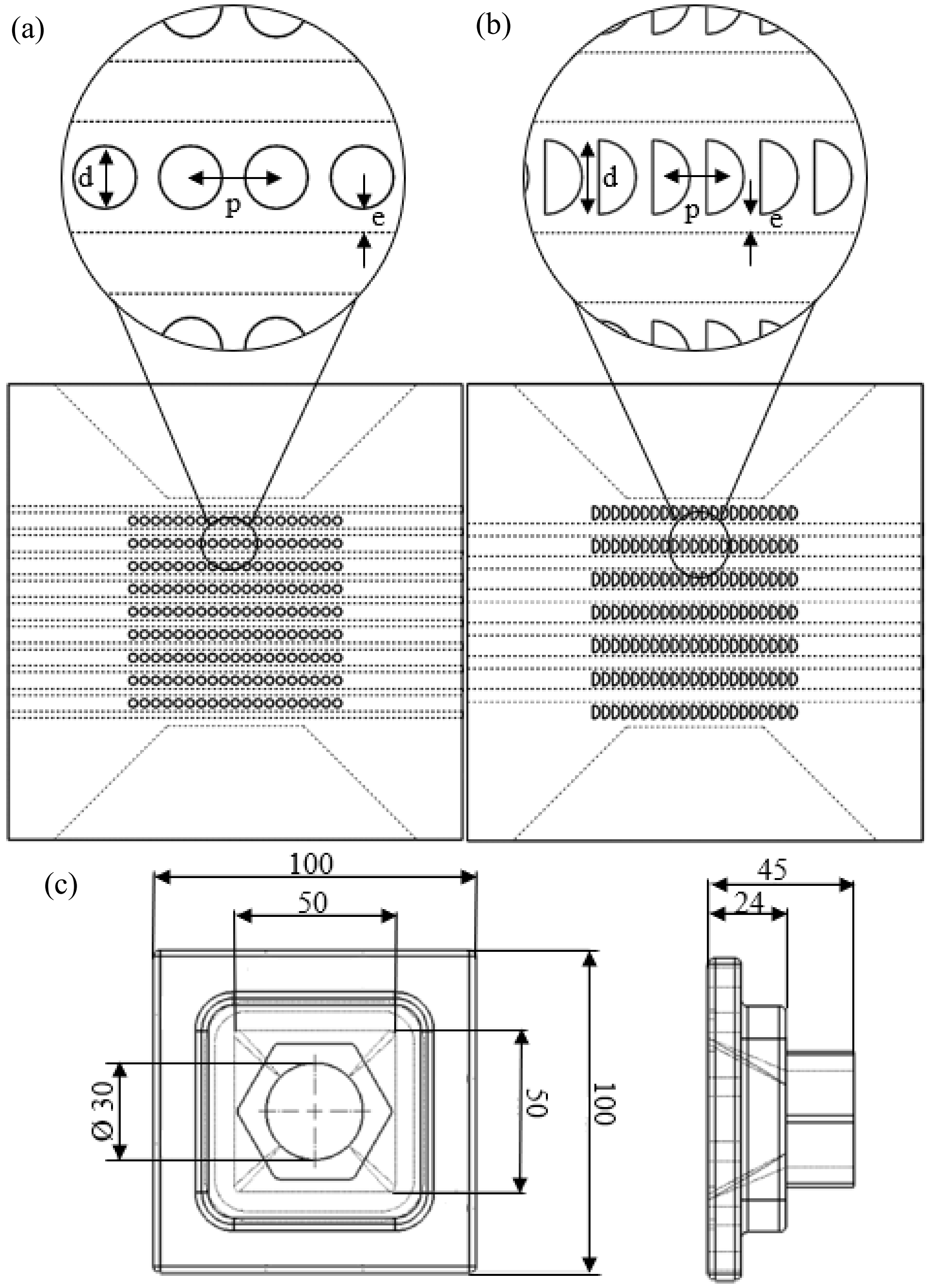

Source: Author (2022).

The main difference between the two branches lies in the diameter and, consequently, the distance between the layers, resulting from the manufacturing process, more specifically in the manufacturing direction. Given that the heat exchanger comprises a cubic core and channels in cross-flow, one branch was manufactured vertically with the channel entrance perpendicular to the powder bed, while the other branch was produced horizontally with the channel entrance parallel to the powder bed. In situations where the circular channel is parallel to the powder bed, a 90° overhang angle arises, requiring the use of a support structure. Nevertheless, since the channel diameter is too small, removing the support structure along the channel would not be possible. Consequently, the channels were produced without the support structure, leading to a slight collapse in the channel's upper part and a reduction in its hydraulic diameter. Table 1 describes the geometry specifications for the SLMHE channels in both arrangements.

Table 1 – SLMHE geometry specifications.

Geometry characteristics	**Circular channel**	**Semicircular channel**
Channel shape	Straight	Straight
Core length (*L*)	100 mm	100 mm
Core height (*H*)	100 mm	100 mm
Core width (*W*)	100 mm	100 mm
Number of layers (*N*)	9 (hot)/10 (cold)	6 (hot)/7 (cold)
Number of channels per layer (*n*)	19	21
Distance between layers (*e*)	0.80 mm (hot)/ 0.67 mm (cold)	0.80 mm (hot)/ 0.67 mm (cold)
Distance between the center of the channels (*p*)	2.5 mm	2.19 mm
Channel diameter (*d*)	1.70mm (hot)/ 1.83 mm (cold)	2.872 mm (hot)/ 2.995 mm (cold)
Channel hydraulic diameter (D_h)	1.70mm (hot)/ 1.83 mm (cold)	1.70mm (hot)/ 1.83 mm (cold)
Total heat transfer area (A_{tot})	0.0913 m^2 (hot)/ 0.1092 m^2 (cold)	0.0901 m^2 (hot)/ 0.1132 m^2 (cold)
Free flow area (A_f)	0.0003881 m^2 (hot)/ 0.0004997 m^2 (cold)	0.0003830 m^2 (hot)/ 0.0005178 m^2 (cold)

Source: Author (2022).

Unlike most existing works, this study opted to use channels with a semicircular cross-section in the vertical direction to apply a symmetry condition in the numerical model and also to facilitate the manufacturing of the channel, since this configuration minimizes the 90° overhang angle that would exist in the horizontal direction. For the calculation of the semicircular channel size (Table 2), the same hydraulic diameter and heat transfer area were kept the same as for the circular channel, consequently, the diameter and the number of semicircular channels per layer increased but the number of layers decreased for both branches in the semicircular configuration. Notice that the heat transfer area slightly varies between configurations (lower than 3%). This arrangement is necessary to compare the configurations of circular and semicircular channels. However, for this diameter of the semicircular channel, it is possible to accommodate a total of 23 channels per layer and 7 layers for each branch (version 2). The distance between layers was also maintained to conserve the same structural characteristics for both channel configurations.

Table 2 – Diameter calculation for channels with semicircular cross-section.

Nomenclature	**Circular**	**Semicircular Present study**	**Semicircular Version 2**	**Semicircular Version 3**	**Semicircular Version 4**
D_{hot} [mm]	1.70	2.782	2.782	1.70	1.70
D_{cold} [mm]	1.83	2.995	2.995	1.83	1.83
e_{hot} [mm]	0.80	0.80	0.80	0.80	0.80
e_{cold} [mm]	0.67	0.67	0.67	0.67	0.67
$D_{h,hot}$ [mm]	1.70	1.70	1.70	1.04	1.04
$D_{h,cold}$ [mm]	1.83	1.83	1.83	1.12	1.12
N_{hot}	9	6	7	9	9
N_{cold}	10	7	7	10	10
n	19	21	23	23	30
$A_{tot.hot}$ [mm^2]	91,326.10	90,114.64	115,146.48	90,466.32	117,999.55
$A_{tot.cold}$ [mm^2]	109,233.18	113,183.16	123,962.51	108,204.82	141,136.72
$A_{free.hot}$ [mm^2]	388.14	382.95	489.33	234.92	306.42
$A_{free.cold}$ [mm^2]	499.74	517.81	567.13	302.48	394.53
$F_{h,hot}$ [mm]	41.70	38.60	45.77	41.70	46.70
$F_{h,cold}$ [mm]	46.83	46.98	46.98	46.83	46.83
$F_{l,hot}$ [mm]	46.70	45.21	49.59	37.15	48.70
$F_{l,cold}$ [mm]	46.83	44.85	49.18	35.79	46.88

Source: Author (2022).

Table 2 shows the possible configurations for the channels with semicircular cross-section, presenting the version studied herein and three other versions varying the number of channels and layers, where in the last two versions the hydraulic diameter is also varied. Remember that the positioning area of the channels is limited by the nozzle dimensions (50 x 50 mm), as seen in Figure 15 (c), represented by F_h for the height of the flow region and F_l for the length of the flow region.

Semicircular channel version 2 has the largest number of channels and layers possible within the flow region, maintaining the same hydraulic diameter as the circular channel version. Version 3 maintains the same diameter and heat transfer area of the circular channel, which consequently decreases the hydraulic diameter and increases the number of channels per layer compared to version 2. And finally, version 4 presents the most significant number of channels and layers possible within the flow region considering diameter only. Versions 2 to 4 are not analyzed in this study since the objective of this study is to compare a similar version of the circular and semicircular channels with the same hydraulic diameter and heat transfer areas. However, it is interesting to notice that it is possible to analyze other channel configurations for the semicircular heat exchanger where a higher heat transfer area could be used and more heat could be exchanged with the same heat exchanger's main dimensions (100 x 100 x 100 mm).

4.1.2 Boundary Conditions and Solver Settings

Two fluids (air and water) and one solid (heat exchanger core) domain were modeled. Three surface types are used in the heat exchanger model: fluid inlets, fluid outlets, and core walls (see Figure 16). All fluid inlets are chosen as temperature (T_{in}) and mass flow rate ($\dot{m}$). The fluid outlets are set as prescribed manometric pressure (P). The model uses two different types of walls: the walls forming the interface between the fluid and solid volumes (coupled) and the outer walls of the heat exchanger (adiabatic by assigning zero heat flux).

The values of the input boundary condition, Table 3, were taken from the work of Silva et al. (2021), who performed forty-five tests. In this study, only twenty-five experimental tests were simulated alternatingly manner due to computational cost (the experimental data are shown in Table 20 in APPENDIX C).

In the hot channel, the water temperature was varied from 40 ºC to 80 ºC, with an increment of 10 °C, and the water mass flow rate was kept constant ($\dot{m}_h$ = 0.264 kg/s) at each temperature. For the cold channel, there were nine levels of air mass flow rate, from 0.085 to

0.0513 kg/s, comprising the theoretical laminar, transition, and turbulent regimes for internal flow inside a circular channel (1,500 ≤ Re ≤ 10,000). In the cold channel, the inlet air temperature remained constant (at room temperature) during the tests in the experimental work described by Silva et al. (2021). The ambient temperature from the experimental tests was prescribed in the numerical model each time. The adopted roughness of 12.21 μm is the mean surface roughness measured on the external walls of the manufactured prototype.

Figure 16 – Heat exchanger model.

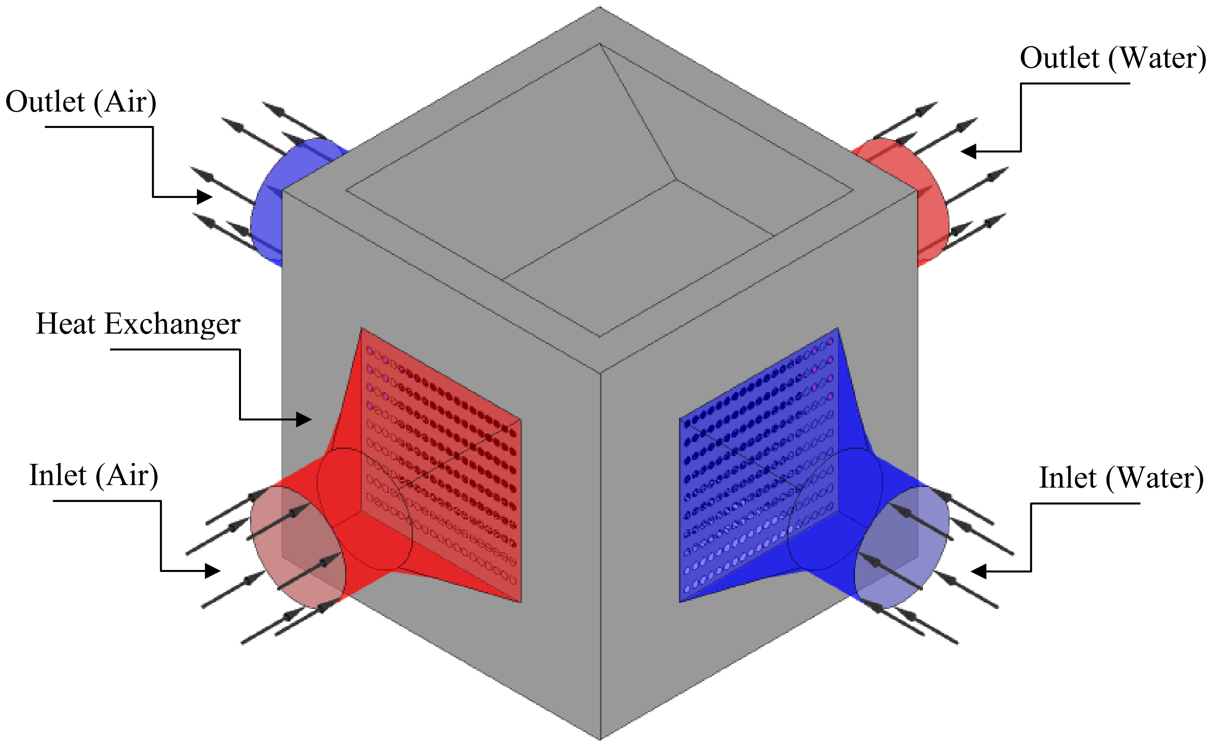

Source: Author (2022).

The Shear Stress Transport model (SST), based on the Reynolds Averaged Navier-Stokes equations (RANS), was applied to model the turbulence phenomenon since this model compensates for deficiencies observed for the k-ε and k-ω models, and produces accurate results under adverse pressure gradients and separate flows. The total energy model for heat transfer was applied for both fluid domains and in the heat exchanger core (solid domain). The convergence of the analysis was achieved by using the High-Resolution method for the convection scheme, with a 10^{-6} RMS (Root Mean Square) residual convergence criteria target, and conservation target of 0.01 (1%).

Table 3 – Boundary conditions.

Boundary conditions for the water domain (hot channel)		
Condition type	**Name/Value**	**Surface**
Mass flow rate ($\dot{m}$)	0.2510 kg/s to 0.2745 kg/s	Inlet nozzle
Temperature (T_{in})	40 ºC to 80 ºC (increment of 10 °C)	Inlet nozzle
Pressure (P)	0 Pa (manometric)	Outlet nozzle
Fluid-Solid Interface	No slip wall/Roughness of 12.21 µm /Conservative heat flux	Contact surfaces between water and heat exchanger core
Wall	No slip wall/Roughness of 12.21 µm /Adiabatic	Nozzle wall
Boundary conditions for the air domain (cold channel)		
Condition type	**Name/Value**	**Surface**
Mass flow rate ($\dot{m}$)	0.0088 kg/s to 0.0513 kg/s	Inlet nozzle
Temperature (T_{in})	22.6 ºC to 27.6 °C	Inlet nozzle
Pressure (P)	0 Pa (manometric)	Outlet nozzle
Fluid-Solid Interface	No slip wall/Roughness of 12.21 µm /Conservative heat flux	Contact surfaces between air and heat exchanger core
Wall	No slip wall/Roughness of 12.21 µm /Adiabatic	Nozzle wall
Boundary conditions for the heat exchanger core		
Condition type	**Name/Value**	**Surface**
Fluid-Solid Interface	Conservative heat flux	Contact surfaces between water and heat exchanger core
Fluid-Solid Interface	Conservative heat flux	Contact surfaces between air and heat exchanger core
Wall	Adiabatic	Bottom and top surfaces of the heat exchanger core

Source: Author (2022).

As a simplifying hypothesis, the fluid domain is formed by liquid water (single phase) and air ideal gas (incompressible to the pressure). Its thermo-physical properties were obtained from the ANSYS CFX library. The solid domain is the core of the heat exchanger itself, made of AISI 316L powder, and its physical properties are shown in Table 4.

Table 4 – Material Properties.

Properties of AISI 316L Metallic Powder	
Property	**Name/Value**
Chemical Composition	Cr (17%), Ni (12%), Mo (2.5%), Mn (1.5%), Si (0.8%), C (0.01%), O (0.06%), N (0.10%) and Fe (Balance)
Nominal Particle Range	20 – 53 μm (max 5% over- and undersize)
Molar Mass (M)	56.23 g/mol
Density (ρ)	7.90 g/cm^3
Specific Heat Capacity (c_p)	450 J/kg-K
Thermal Conductivity (k)	14.9 W/m-K

Source: Adapted from Höganäs (2022) and Sandmeyer (2014).

The physical properties described above were taken from the metal powder supplier's datasheet. It is expected that the mechanical and thermal properties of the 316L powder used in additive manufacturing will vary depending on the direction (vertical or horizontal) due to the manufacturing process, but in this work, they were adopted as constant.

4.1.3 Symmetry Condition

The symmetry plane is used in cases where the domain to be studied is two-dimensional, because the software only performs three-dimensional simulations. Its applicability extends to cases that present symmetrical characteristics, making it possible to simulate half of the geometry, reducing the computational simulation's effort. The symmetry condition mirrors the flow concerning a line or a plane, imposing no flux across the boundary, i.e., the component of the velocity normal to the symmetry boundary is zero, as are the gradients of the scalar variables (BLAZEK, 2015).

Therefore, to decrease the computational effort required to simulate the entire heat exchanger core, the symmetry condition was applied in the ANSYS DesignModeler module, where the geometry is symmetrically divided into two parts through cutting by the *Symmetry* tool plane. Since the heat exchanger studied has a cross-flow configuration, it was impossible to make more than one symmetry plane due to the inlet and outlet position of the nozzles. Figure 17 shows the symmetry condition applied to half of the three-dimensional domain of the complete core already selected as the boundary condition in ANSYS CFX. The red arrows represent the symmetry boundary condition, and the green highlights indicate the interfaces between the fluid-solid and solid-solid domains.

Figure 17 – Heat exchanger model with symmetry condition.

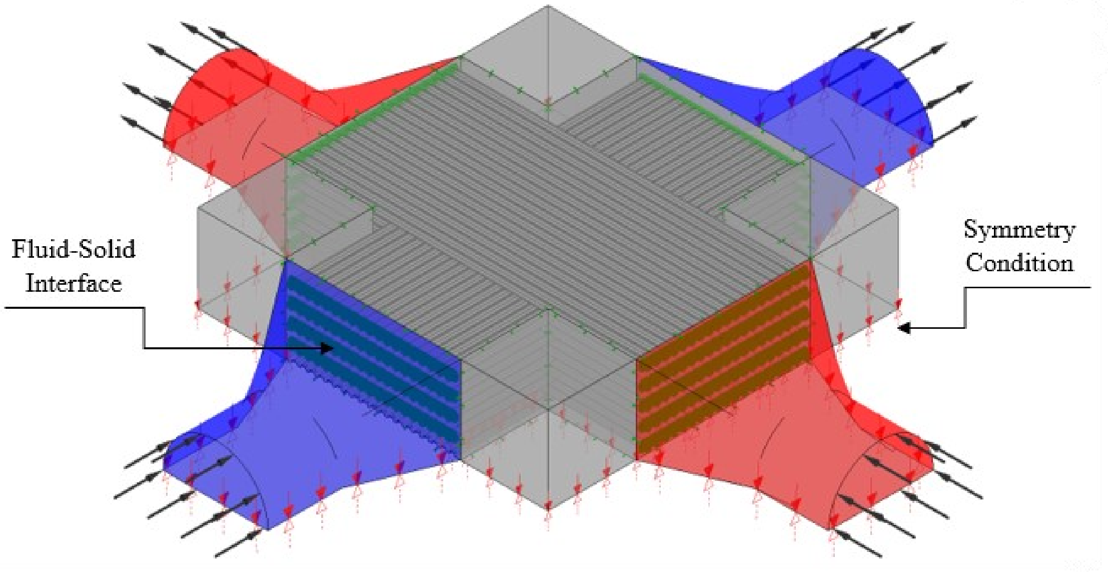

Source: Author (2022).

Since the symmetry boundary condition imposes constraints that mirror the expected flow pattern or thermal solution on either side of it, only the values of fluid mass flow rate at the inlet are split in two. All other initial and boundary conditions remained the same, as did the solver settings (Table 3). In this adopted model, the heat exchanger core's top extra structures for connections were disregarded since they do not significantly interfere with the final result.

4.2 SINGLE CHANNEL GEOMETRIES

4.2.1 Computational Domain

In order to study the effects of the channel cross-section geometry on heat transfer and pressure drop, three geometries were investigated (Figure 18). Analyses were performed for each branch separately, where only a single channel of the hot branch and another of the cold branch were examined separately, as shown in Figure 19.

Figure 18 – Single channel geometries studied: circular (a), deformed circular (b), and inclined V-shaped chaotic circular (c).

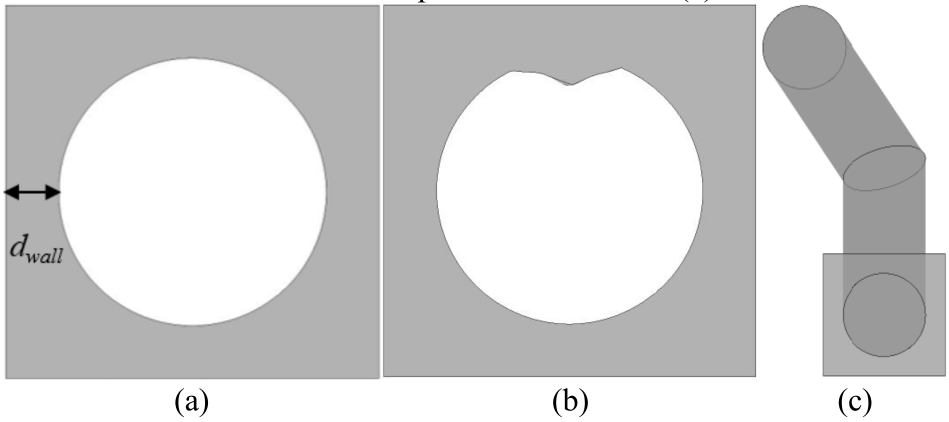

Source: Author (2022).

In Figure 18, the channel with a circular cross-section (a) represents a reduction of the main geometry studied in this study (Figure 15 (a)). The second geometry studied (b) has a circular cross-section with a depression at the top of the cylinder that will roughly represent the final design of the channel structure due to manufacturing in the horizontal direction. This investigation aims to determine how much numerical error concerning the experimental data this difference in geometry can produce. In this way, as it is a preliminary study, the deformed geometry was designed in a flexible and simplified manner without following any standard. At this initial stage of the investigation, it is common to use simple or improvised geometries that allow the evaluation of the effect of a single factor alone, without the need to worry about the precision and detail of the final design.

Finally, a chaotic channel with a circular cross-section (c) having a V-shaped path, made of a succession of 90° sharp bends followed by 45° bends and returned to 90º sharp bends, and the upper part with 55° inclination to the horizontal, was studied. This last geometry configuration was the one that obtained the best result compared to the other three analyzed in the study on chaotic channels presented in detail in APPENDIX, which had as its objective aimed to improve the thermal-hydraulic performance of compact heat exchangers by developing a 3D geometry that induces chaotic advection.

Figure 19 – Representation of the hot branch of the chaotic channel in a V-shape with 55° inclination to the horizontal and circular cross-section.

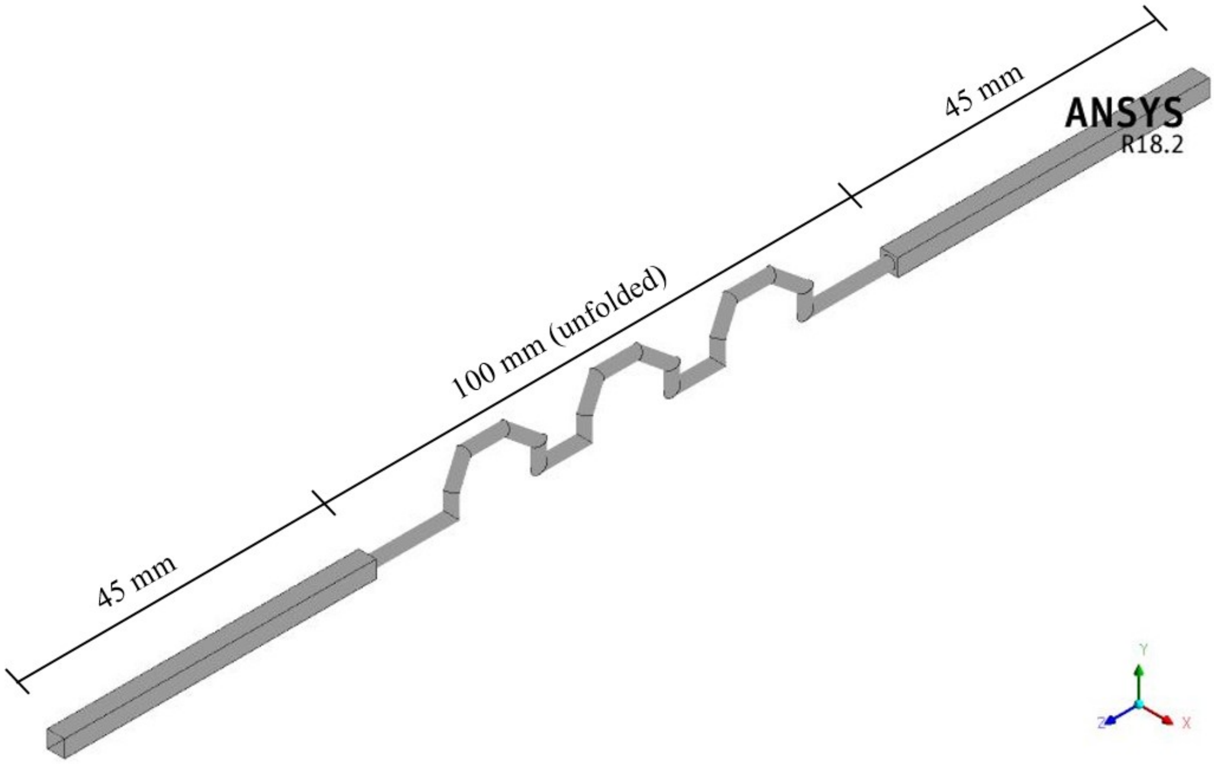

Source: Author (2022).

The circular cross-section channel is 1.83 mm (cold branch) and 1.70 mm (hot branch) in diameter. All channels have 100 mm in unfolded length and an additional parallelogram is situated at the ends, representing the nozzle flow. This nozzle representation was added to model the recirculation regions at the entrance and exit of the channels, having a length of 45 mm and a distance from the channel wall (d_{wall}) of 0.335 mm for the cold and 0.4 mm for the hot branch.

4.2.2 Boundary Conditions and Solver Settings

The boundary conditions used for the individual channels were almost the same as in the previous section and are presented in Table 5. It is worth noting that the mass flow and heat transfer rate per unit area was divided by the number of channels for each branch (171 channels for the hot branch and 190 channels for the cold branch). The total heat transfer rate per unit area values were taken from the study of Silva et al. (2021).

Table 5 – Boundary conditions for the single channels.

Boundary conditions for the water domain (hot branch)		
Condition type	**Name/Value**	**Surface**
Mass flow rate ($\dot{m}$)	0.0015 kg/s to 0.0016 kg/s	Inlet nozzle
Temperature (T_{in})	60 ºC	Inlet nozzle
Pressure (P)	0 Pa (manometric)	Outlet nozzle
Wall	No slip wall/Roughness of 12.21 µm /Heat flux of 869 W/m^2	Channel wall
Wall	No slip wall/Roughness of 12.21 µm /Adiabatic	Nozzle wall
Boundary conditions for the air domain (cold branch)		
Condition type	**Name/Value**	**Surface**
Mass flow rate ($\dot{m}$)	0.000046 kg/s to 0.00027 kg/s	Inlet nozzle
Temperature (T_{in})	23.3 ºC to 29.3 °C	Inlet nozzle
Pressure (P)	0 Pa (manometric)	Outlet nozzle
Wall	No slip wall/Roughness of 12.21 µm /Heat flux of 11,249 W/m^2	Channel wall
Wall	No slip wall/Roughness of 12.21 µm /Adiabatic	Nozzle wall

Source: Author (2022).

All others boundary conditions and solver settings were the same used for the complete core of Section 4.1.2. To reduce the number of simulations due to the computational cost, only the five central cases (T60C1, T60C3, T60C5, T60C7, and T60C9) were simulated, for each proposed geometry. The experimental data used in the numerical simulations for all cases studied are shown in Table 20 in APPENDIX C.

5 RESULTS AND DISCUSSIONS

The effects of the Reynolds number on heat transfer rate and numerical pressure drop are presented in this chapter. Initially, the mesh independence study is developed, followed by the validation of the numerical model by comparing the results obtained numerically with experimental and theoretical data. The comparison of results from the complete model with circular and semicircular cross-sections is demonstrated next. Finally, the thermal and hydrodynamic results are evaluated with emphasis on the evolution of the static pressure of the measurement points along the channels. The results of the discretized models of the individual channels are shown in the sequel.

5.1 MESH INDEPENDENCE STUDY

5.1.1 Complete Core

Mesh generation consists of decomposing the total volume into smaller volume elements to which the finite volume method will be applied to solve the system of equations. This step was performed with the help of ANSYS ICEM, a high-quality mesh generator that provides several modes of mesh creation. First, due to the difficulty of meshing the complete model at once, a mesh was generated for each computational domain separately: hot branch, cold branch, and core of the heat exchanger (where its corners were also separated). Then, for the complete geometry an unstructured mesh, with hexahedral and wedge-shaped elements, was chosen for both geometrical channels (Figure 20).

It was necessary to refine the mesh in the inlet and outlet regions of the channels and the nozzle region near the wall of the channels (1 mm distance region from the channels) for the simulation to be more successful because the higher the number of hexahedrons the higher the accuracy of the results. It should be noted that mesh refinement near the walls is also necessary for the model to adequately resolve the flow boundary layer. In addition, local mesh refinement is also essential to better resolve specific fluid dynamics problems such as upward stagnation flow and backward-facing step geometry.

Figure 20 – Mesh of circular (a) and semicircular (b) cross-section.

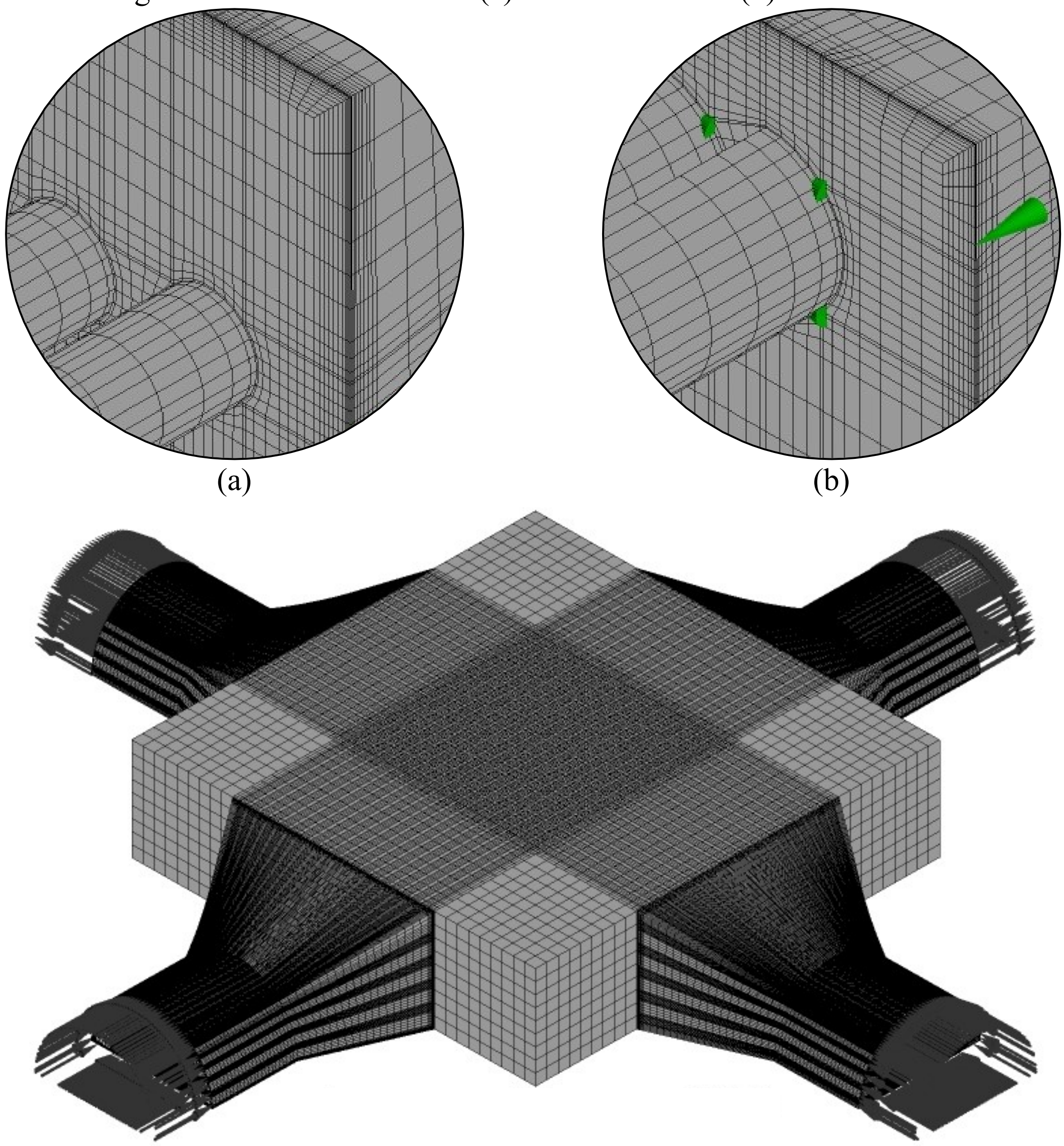

(a) (b)

Source: Author (2022).

A mesh independence study was performed for the complete core's heat transfer rate and pressure drop for both channels with circular and semicircular cross-sections. For the case of the circular channels, it can be seen in Figure 21 that as mesh refinement occurs, there is a stabilization of the evaluated properties, between Mesh 4 and 5, with a difference in heat transfer and pressure drop below 1%.

The graph (Figure 21, Figure 23 and Figure 26) illustrating the evolution of the mesh independence test is composed of three axes, in which the values of heat transfer and pressure drop are plotted as a function of the Reynolds number of the cold branch. It was generated using the Reynolds values of the cold branch, as in the hot branch, the mass flow rate is kept constant, maintaining the Reynolds unchanged. In the legend, each mesh is identified by a distinct symbol, while the two dashed lines with different patterns and colors represent the two branches, hot and cold, in red and blue, respectively. This pattern is maintained throughout the results chapter.

Figure 21 – Circular channel mesh independence study.

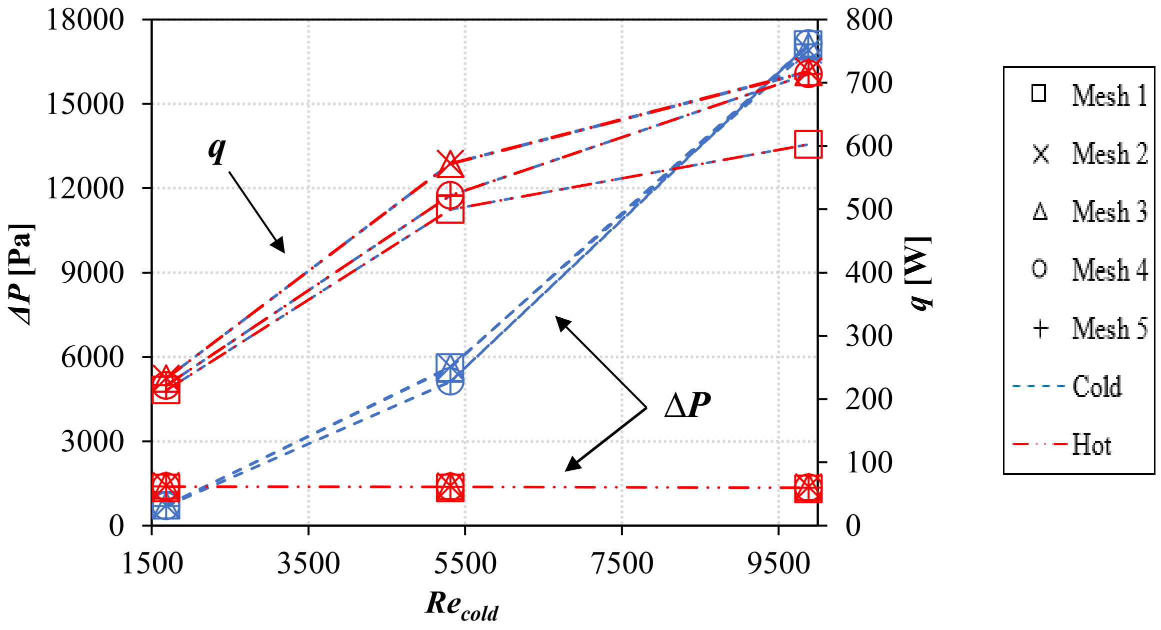

Source: Author (2022).

In more detail, five meshes were analyzed, starting with the essential refinement of the commercial software and then increasing the number of elements: 2,105,880, 5,317,064, 6,566,240, 9,385,291, and 12,731,431. Two main regions refinements were analyzed, the solid core and the fluid branches. Total heat transfer rate and total pressure drop were applied to compare meshes. From Mesh 1 to Mesh 2, the number of elements on the solid core and fluid branches was increased by a rate of 2 to 3 times higher. Results indicated that both the heat transfer and the pressure drop changed by 10 to 20% for most cases analyzed. From Mesh 2 to Mesh 3, the number of elements on the solid core was again increased by a rate of 2, and the fluid elements from the branches were kept the same as in Mesh 2. Less than a 2% difference was found for heat transfer and pressure drop between Meshes 2 and 3. Based on these results, the number of elements of the solid core was considered converged and kept constant for Meshes 3 to 5. From Mesh 3 to 4, the number of elements on both fluid branches was increased at a rate of 2, and more than a 10% difference was found for heat transfer and pressure drop. From Mesh 4 to 5, the number of elements from both fluid branches was again augmented by a rate of 1.5. Results from Meshes 4 and 5 indicated a difference of 0.14% for heat transfer and

0.21% for pressure drop. Based on that, Mesh 4 was chosen as the final mesh for this work. The characteristics of the studied meshes are shown in Table 21 in APPENDIX C.

It is important to emphasize that the magnitude y^+ represents the dimensionless coordinate of the wall (see Section 3.4). Therefore, it should be below $y^+ < 1$ to adequately use the SST turbulence model (MENTER et al., 2003), as can be seen in Figure 22. Although the values of y^+ stay close to 1 along the channels, this value increases in the inlet and outlet regions of the channels near the walls of the nozzles. Still, the values achieved were considered adequate to meet the criteria that the turbulence model application requires to solve the boundary layer when comparing results from the numerical model to the experimental results.

Figure 22 – Circular channel, y^+ region.

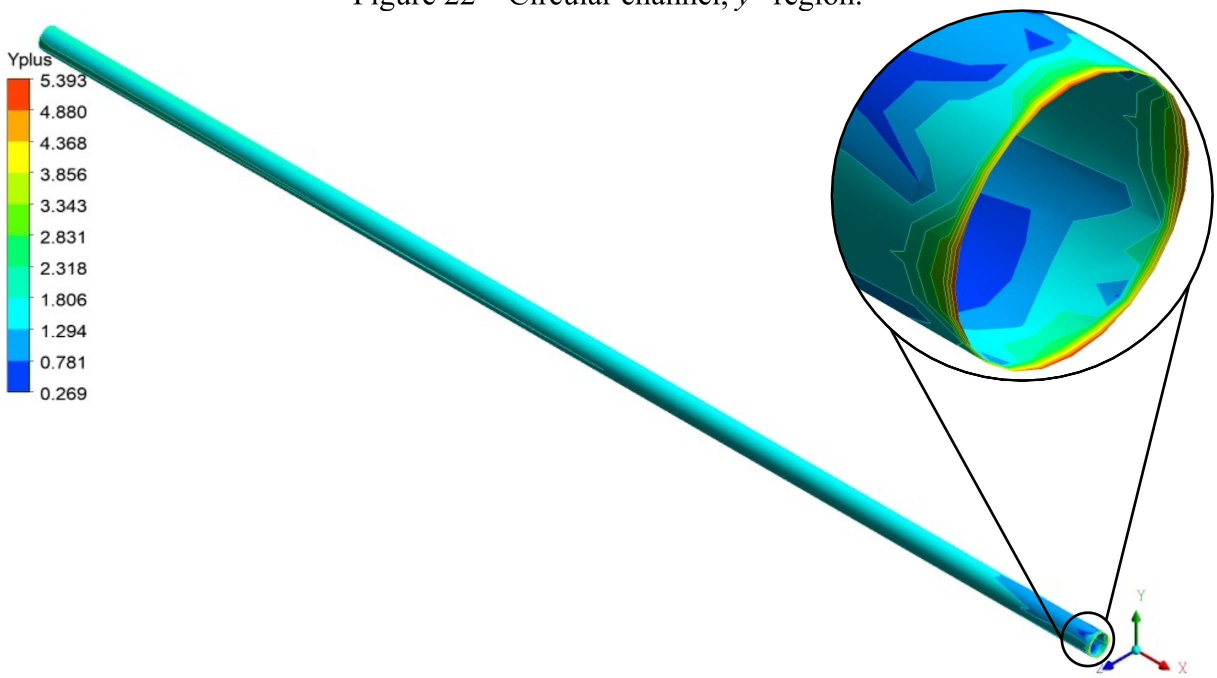

Source: Author (2022).

Thus, for the core with circular cross-section channels, Mesh 4 with a total of 9,385,291 elements was chosen to conduct the twenty-five cases studied, since it presented the best convergence of results. It is important to note that the independent study was performed for the entire input mass flow range and the results were consistent, as can be seen in APPENDIX C.

Figure 23 shows the evolution of the mesh independence study performed as a function of heat transfer rate and pressure drop in the cold branch of the complete core with a semicircular cross-section. The same logic of analysis described before was applied to the refinement study. It is noticeable that as mesh refinement occurs, there is a stabilization of the evaluated properties to values below 1% in Mesh 2, except for the last refinement, which reached 3.35% for the pressure drop. For the heat transfer rate, the relative error was 0.80% and to pressure drop was 3.35%.

Figure 23 – Semicircular channel mesh independence study.

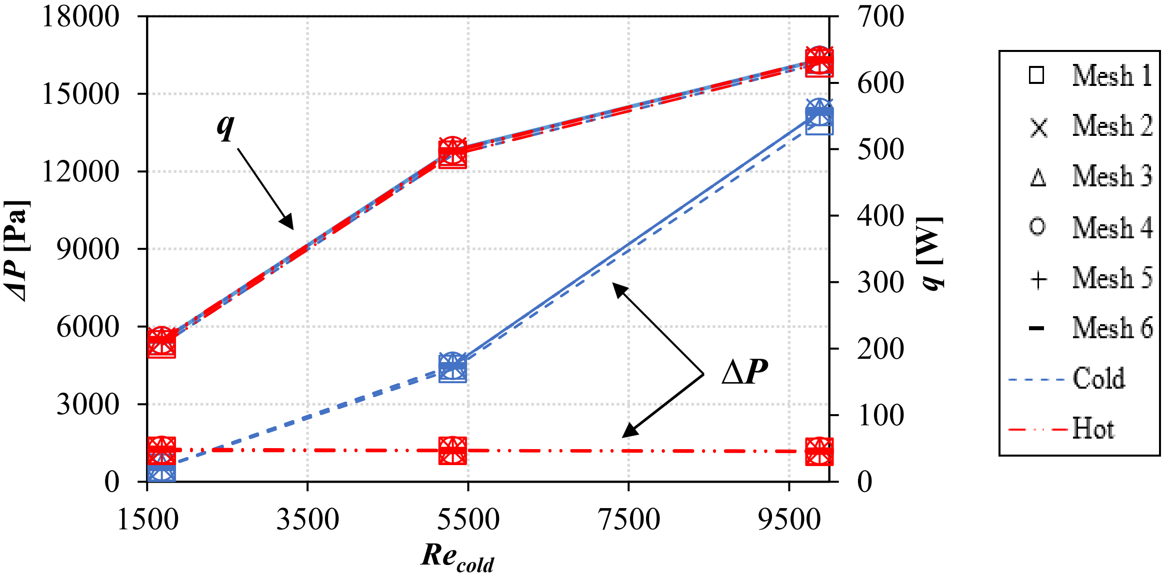

Source: Author (2022).

Six meshes were analyzed, starting with the essential refinement of the commercial software and then increasing the number of elements: 1,823,196, 5,441,188, 8,891,768, 7,564,218, 8,445,308, and 9,281,347. The characteristics of the studied meshes are shown in Table 22 in APPENDIX C.

The behavior of y^+ of the semicircular channel can be seen in Figure 24, and just as in the circular channel, even though the values of y^+ stay close to 1 along the channels, this value increases significantly in the inlet and outlet regions of the channels near the walls of the nozzles. Nevertheless, the values achieved are adequate to meet the turbulence model application's criteria requires to solve the boundary layer, presenting good agreement with the circular channel.

Figure 24 – Semicircular channel, y^+ region.

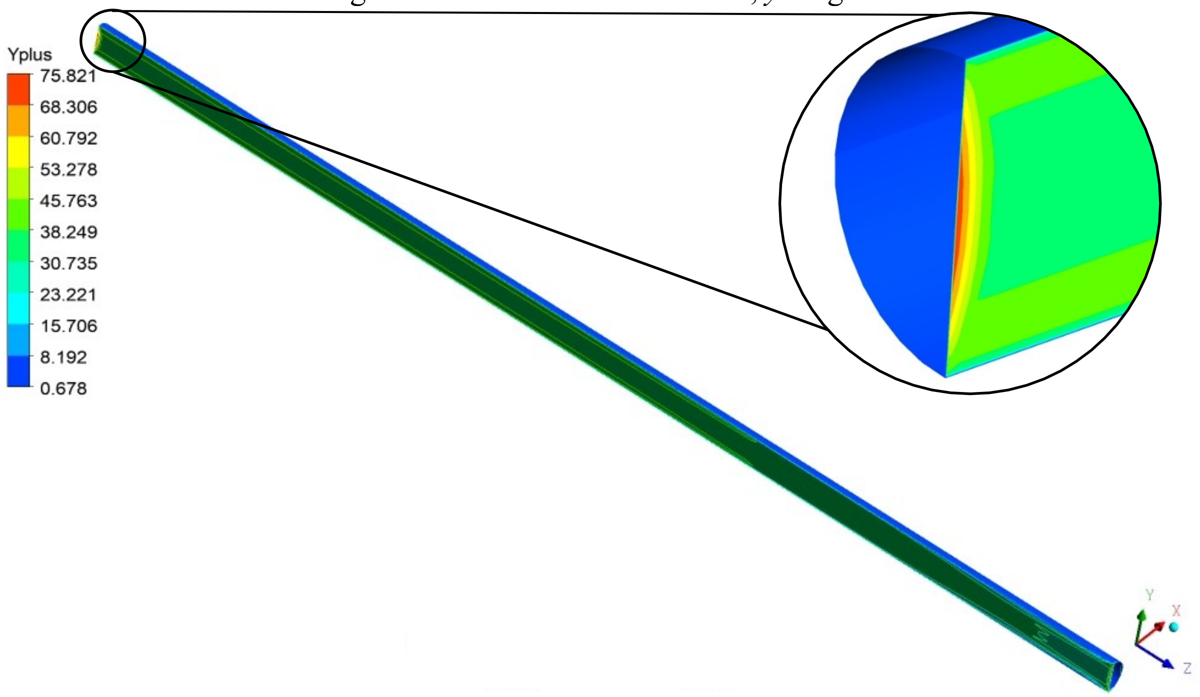

Source: Author (2022).

To the core with a semicircular cross-section channel, Mesh 2 with 5,441,188 elements, was chosen to conduct the twenty-five cases studied, since it presented the best cost-benefit regarding computational time and convergence of results. The mesh could have been more refined, but this would have increased the computational effort, increasing the simulation time, so a less refined mesh was chosen, which generated a satisfactory result. More details about the convergence study can be found in APPENDIX C.

5.1.2 Single Channel Geometries

Similarly, as for the complete core, a mesh was generated in ANSYS ICEM for each computational domain separately: hot branch and cold branch. However, the solid domain should have been considered since only a single channel is being studied. The unstructured mesh used to discretize the fluid domain is composed of hexahedral and wedge-shaped elements for the channels with circular (Figure 25 (a)) and deformed circular (b) cross-sections. For the chaotic channel (c), it was decided to use, due to the geometry complexity, ANSYS Meshing software to develop the hexahedral mesh through the MultiZone method. As far as refinement is concerned, a simpler mesh was chosen in terms of global parameters due to the processing time for obtaining the results, but a higher refinement (inflation) was performed in the regions near the wall, which are the areas of greatest interest. More specifically, one can have the refined mesh around the cylinder with a band of hexahedrons (inflation) with a given number of layers and growth rate, as well as the mesh transition from wedge-shaped to hexahedrons elements near the wall.

Figure 25 – Mesh of circular (a), deformed circular (b), and chaotic channels with circular cross-sections (c).

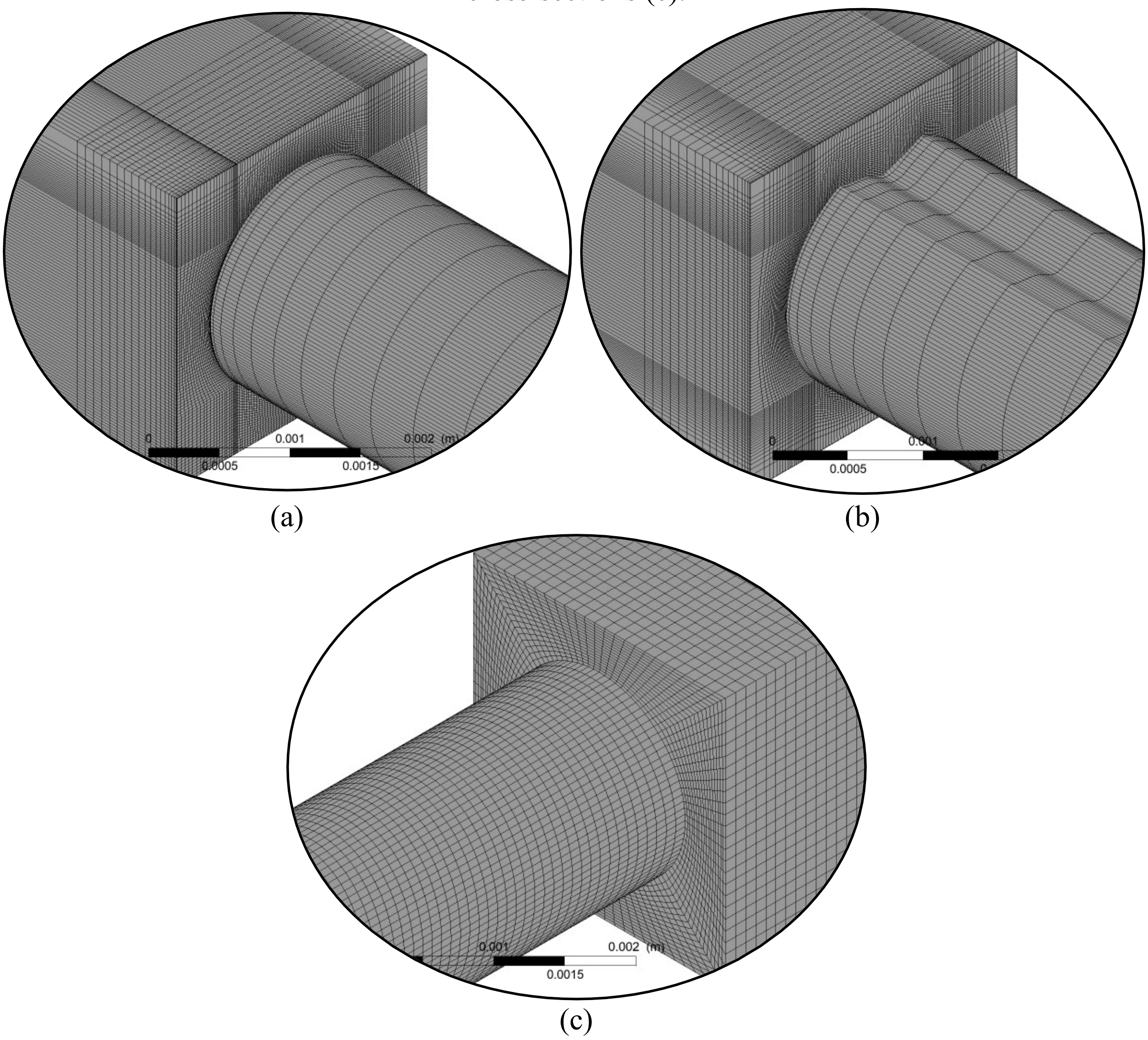

(a) (b) (c)

Source: Author (2022).

A mesh independence study was performed for the heat transfer rate and pressure drop of the three studied geometries. In Figure 26, it can be seen that as mesh refinement occurs, there is a stabilization of the evaluated properties to values below 4% in the first mesh tested, due to the high number of elements in the initial mesh. For the Nusselt number, the relative error was less than 0.2% for all arrangements. And to pressure drop, the relative error was

0.54% to the circular channel, 0.26% and 1.10% to the deformed circular channel, and 1.71% and 3.25% to the chaotic channel, respectively.

Figure 26 – Single channel mesh independence study: circular (a), deformed circular (b), and chaotic channels with circular cross-sections (c).

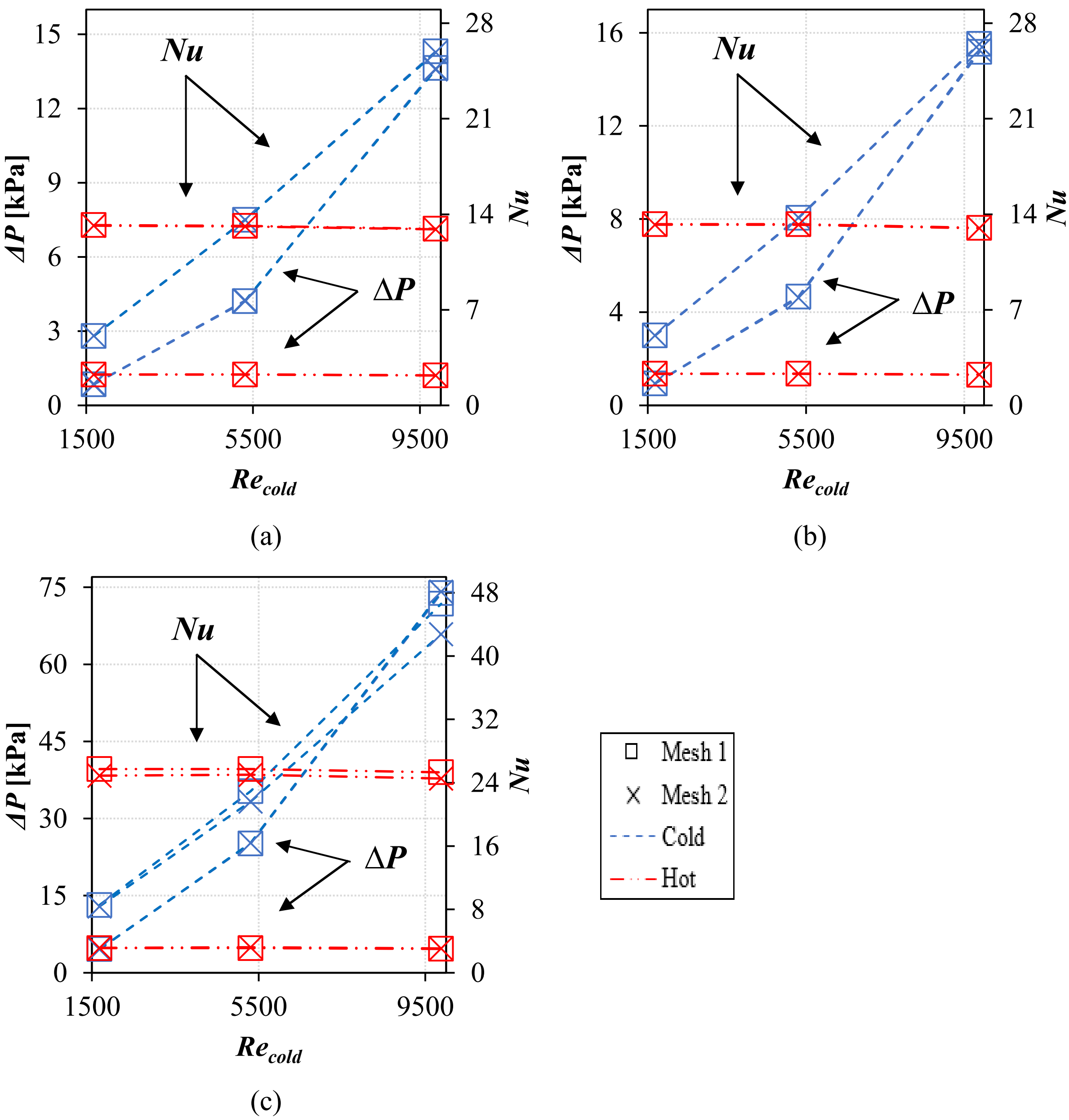

Source: Author (2022).

The characteristics of the two studied meshes are shown in Table 23 in APPENDIX C. Reproducing the behavior of complete geometries with circular and semicircular channels, although the values of y^+ stay close to 1 along the channels, this value increases significantly in the inlet and outlet regions of the channels near the walls of the nozzles (Figure 27). Thus, an adequate mesh was obtained to meet the criteria that the application of the turbulence model requires to solve the boundary layer.

Figure 27 – Semicircular channel, y^+ region of circular (a), deformed circular (b), and chaotic channels with circular cross-sections (c).

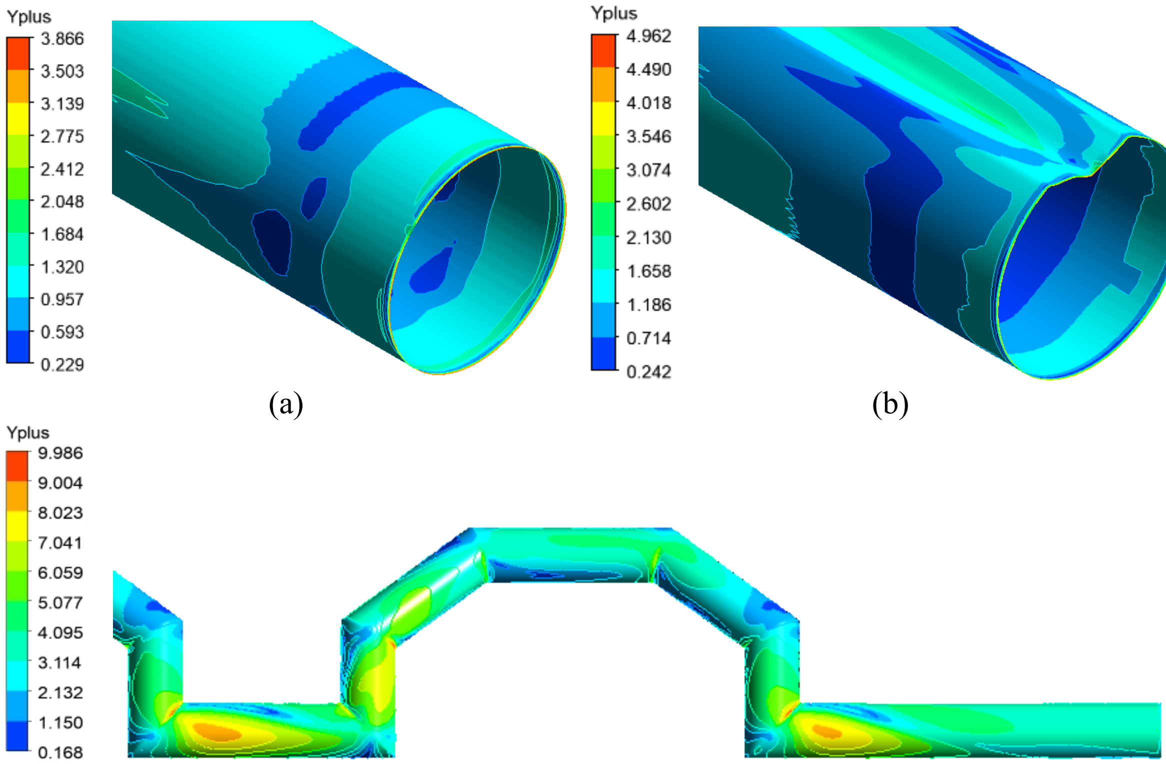

(a) (b)

(c)

Source: Author (2022).

For the three geometries studied, the first mesh was chosen to conduct the five cases studied because it presented the best cost-benefit regarding computational time and convergence of results. Totaling 2,703,417 elements to circular channel (hot and cold branch), 2,703,417 elements to deformed circular channel (hot and cold branch), 3,532,146 (hot branch) and 3,992,392 (cold branch) elements to chaotic channel with a circular cross-section.

The complete core numerical models are validated based on existing experimental data. In turn, the data from the previously developed complete core numerical model with circular channels are used to validate the numerical models of individual channels.

5.2 NUMERICAL MODEL VALIDATION

5.2.1 Complete Core

In this section, the numerical results for the geometry of channels with a circular cross-section, are compared with those obtained from the experimental and theoretical models. It is worth remembering that the symmetry condition was applied to analyze the complete geometry, and the initial mass flow rates were divided by two, so the heat transfer rate obtained as numerical results was multiplied by two to consider the complete core. Table 6 indicates the heat transfer rate (q) comparison of experimental and numerical results for both hot and cold branches.

Table 6 – Experimental and numerical heat transfer rate for the heat exchanger with a circular channel.

Test	Experimental Result		Numerical Result		Difference (Num vs. Exp)	
	q_h [W]	q_c [W]	q_h [W]	q_c [W]	$E_{q.h}$ [%]	$E_{q.c}$ [%]
T40C1	120.76	79.15	108.08	108.09	10.50	36.55
T40C3	173.81	156.45	178.15	178.15	2.50	13.87
T40C5	260.86	251.71	256.73	256.72	1.58	1.99
T40C7	327.00	322.81	317.97	317.96	3.06	1.50
T40C9	344.54	320.27	326.76	326.76	5.16	2.03
T50C1	159.64	123.70	152.48	152.48	4.48	23.26
T50C3	229.86	212.18	246.46	246.44	7.22	16.15
T50C5	362.63	368.21	372.23	372.22	2.65	1.09
T50C7	461.34	462.10	449.19	449.18	2.63	2.80
T50C9	506.76	487.40	482.10	482.10	4.87	1.09
T60C1	225.06	178.62	221.32	221.31	1.66	23.90
T60C3	323.09	301.81	350.12	350.11	8.37	16.00
T60C5	515.40	517.90	521.67	521.68	1.22	0.73
T60C7	650.90	647.96	626.81	626.78	3.70	3.27
T60C9	755.97	737.01	713.79	713.78	5.58	3.15
T70C1	278.07	230.14	286.28	286.27	2.96	24.39
T70C3	436.18	408.07	464.77	464.77	6.56	13.89
T70C5	649.81	618.89	631.70	631.71	2.79	2.07
T70C7	886.95	869.60	831.62	831.59	6.24	4.37
T70C9	1034.78	999.85	955.89	955.88	7.62	4.40
T80C1	320.47	280.93	344.96	344.94	7.64	22.79
T80C3	512.93	497.14	564.32	564.33	10.02	13.52
T80C5	819.18	828.48	826.77	826.78	0.93	0.21
T80C7	1,079.02	1,104.28	1,049.21	1,049.17	2.76	4.99
T80C9	1,235.44	1,242.71	1,177.70	1,177.69	4.67	5.23

Source: Author (2022).

As observed in the experimental work of Silva et al. (2021), the first case (T40C1) presented the most significant discrepancy in the heat transfer rate between numerical and experimental data. The reduced temperature difference for the hot branch accounts for the divergence in the results, especially at lower flow rates. It results in great uncertainty in the experimental data, as the heat transfer rate between the hot and cold branches can diverge at low flow rates. The numerical model presented, in general, lower results than the experimental data in the hot branch and higher in the cold branch. The average difference between them was 5% for the hot branch and 10% for the cold branch, with a maximum difference of 10.5% and 36.6% (T40C1), respectively.

The results of both branches need to be similar since the thermal exchange results in the thermal equilibrium of the system studied. Thus, although the results of the table above show high values of relative errors with the experimental results for some cases of the cold branch, the relative error between numerical results for the hot and cold branches is below 0.005%, showing that the numerical results indicate that the energy balance for the numerical solution is consistent since the walls of the heat exchanger were set as adiabatic. It is important to highlight that the experimental results used in the numerical validation have an uncertainty between 5 and 10% for the total heat transfer and pressure drop in the analyzed range.

Figure 28 presents the results of the heat transfer rate for hot and cold branches, water, and air, respectively.

Figure 28 – Heat transfer rate comparison of experimental and numerical results for the heat exchanger with the circular channel: (a) as heat transfer rate and (b) as a function of Re_{cold}.

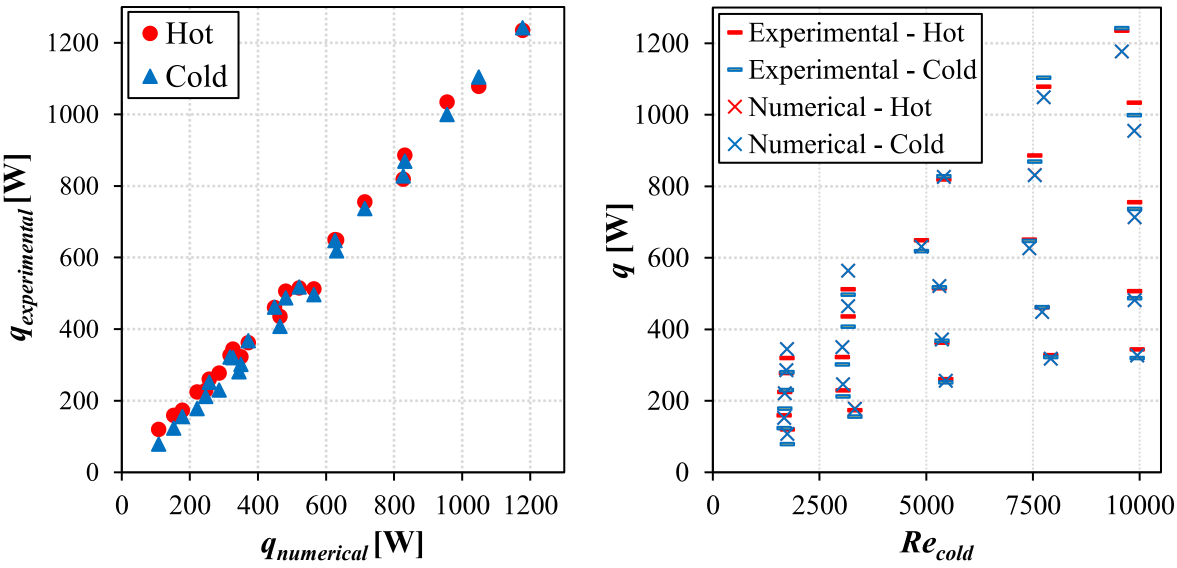

(a) (b)

Source: Author (2022).

It is evident that the heat transfer rate increases as the Reynolds number and the temperature of the hot branch increase. However, for Reynolds numbers higher than 5,500, the rate tends to remain at constant ranges. According to Silva et al. (2021), this behavior is due to the limitations of the experimental apparatus, since it occurs due to the increase of the compressed air inlet temperature from one test to the next, generated by insufficient air storage in the compressor.

Table 7 indicates the pressure drop (*ΔP*) comparison of experimental and numerical results for both hot and cold branches, where the numerical model showed lower results than the experimental data.

Table 7 – Experimental and numerical comparison of pressure drop for the heat exchanger of circular channel.

Test	Experimental Result		Numerical Result		Difference (Num vs. Exp)	
	ΔP_h [Pa]	ΔP_c [Pa]	ΔP_h [Pa]	ΔP_c [Pa]	$E_{\Delta P.h}$ [%]	$E_{\Delta P.c}$ [%]
T40C1	2,030.10	624.70	1,255.20	687.57	38.17	10.07
T40C3	2,059.90	2,331.00	1,274.17	2,087.48	38.14	10.45
T40C5	2,028.20	6,786.60	1,279.49	5,091.39	36.92	24.98
T40C7	2,058.30	14,649.30	1,295.05	10,332.17	37.08	29.47
T40C9	2,032.10	22,888.70	1,267.08	16,298.44	37.65	28.79
T50C1	2,214.30	599.50	1,324.61	665.08	40.18	10.94
T50C3	2,159.00	2,001.30	1,289.69	1,857.87	40.27	7.17
T50C5	2,115.40	6,765.60	1,263.86	5,104.29	40.26	24.56
T50C7	2,125.60	14,441.10	1,263.22	10,211.57	40.57	29.29
T50C9	2,085.20	23,438.90	1,237.48	16,766.25	40.65	28.47
T60C1	2,155.80	646.00	1,387.34	691.07	35.65	6.98
T60C3	2,094.50	2,032.20	1,360.79	1,882.64	35.03	7.36
T60C5	2,134.60	6,732.30	1,380.64	5,121.84	35.32	23.92
T60C7	2,111.80	13,530.80	1,377.12	9,693.33	34.79	28.36
T60C9	2,061.20	23,937.00	1,347.36	17,146.25	34.63	28.37
T70C1	2,078.20	700.30	1,447.11	737.80	30.37	5.36
T70C3	2,056.40	2,278.00	1,436.70	2,073.57	30.14	8.97
T70C5	2,056.70	5,742.60	1,432.78	4,490.44	30.34	21.81
T70C7	2,085.90	14,282.30	1,446.77	10,186.87	30.64	28.68
T70C9	2,097.50	24,269.00	1,448.48	17,459.06	30.94	28.06
T80C1	2,082.30	744.80	1,448.14	767.28	30.46	3.02
T80C3	2,095.50	2,355.90	1,444.04	2,129.23	31.09	9.62
T80C5	2,074.10	7,297.10	1,419.54	5,530.11	31.56	24.22
T80C7	2,060.40	15,244.10	1,405.67	10,930.28	31.78	28.30
T80C9	2,030.10	23,247.60	1,390.86	16,662.65	31.78	28.33

Source: Author (2022).

As the mass flow rate is kept constant in the hot branch, the pressure drop values are also kept constant and present a maximum difference of 41% that decreases with increasing water temperature, resulting in an average difference of 35% compared to the experimental data. In the cold branch, the difference compared to the experimental data increases with increasing Reynolds number reaching 29% for Re > 7,000. It is possible to observe that for Re > 5,000, a considerable increase occurs compared to the cases with smaller values that stay below 10% in all cases except the first one (T40C1). The average relative error of the cold branch was 19%.

The described behavior of the two branches, hot and cold, can be seen in Figure 29, which compares the experimental and numerical pressure drop results for the twenty-five cases studied. As noted by Silva et al. (2021), this difference between the experimental and numerical data may be due to the geometric imperfections of the circular channel arising from the manufacturing process (variation of the diameter and circularity along the channel), since the numerical model considers the circular channel with constant geometry. Another explanation for this difference is the non-uniformity of the mass flow rates in the nozzles, which according to Chu et al. (2019), is intensified with increasing inlet mass flow rate due to tapering in the transition region between the nozzle and the channels, which can cause recirculation of the flow in these regions.

Figure 29 – Pressure drops comparison of experimental and numerical results: (a) as pressure drop and (b) as a function of Re_{cold}.

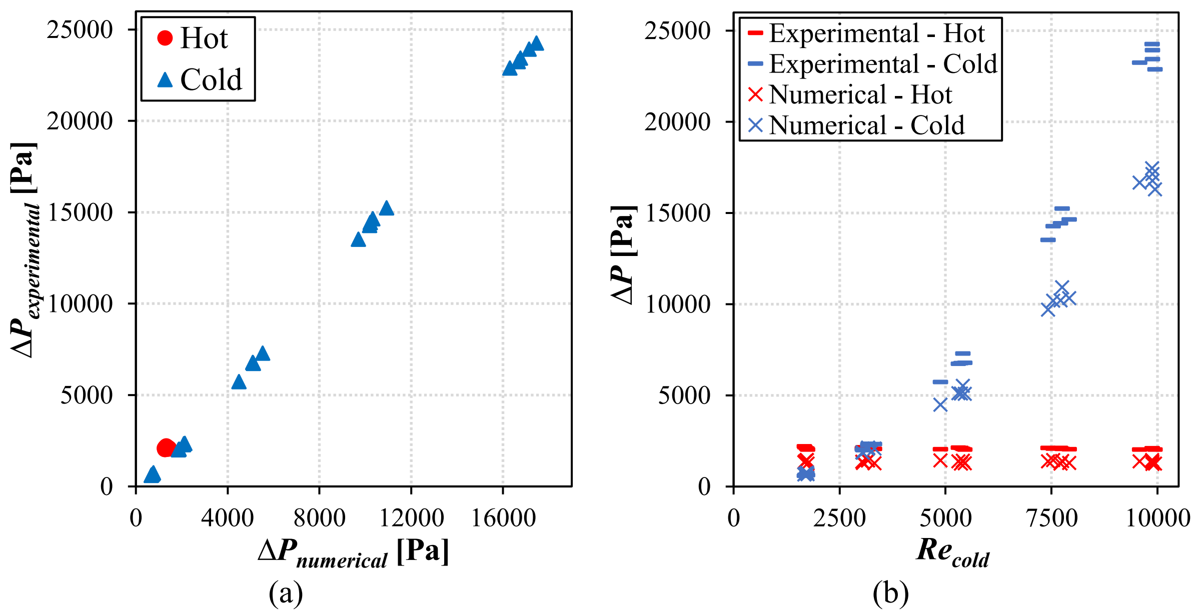

Source: Author (2022).

To perform a complete analysis of the pressure drop between the experimental and numerical data, the results presented in this section will be compared, with the theoretical model developed by Silva et al. (2021), in the next section.

5.2.1.1 Theorical Model Comparison

To verify the discrepancy between the numerical and experimental results in pressure drop was evaluated a comparison between the three models, experimental, theoretical, and numerical, in the cold branch (Table 8). Remember that the pressure drop in the hot branch is constant due to the constant water mass flow rate, so only the results for the cold branch are analyzed below.

Table 8 – Model Comparison.

Test	**Experimental**	**Numerical**	**Theorical**	**Difference [%]**		
	ΔP_c [Pa]	**ΔP_c [Pa]**	**ΔP_c [Pa]**	$E_{\Delta P.c\ (E\ vs\ T)}$	$E_{\Delta P.c\ (E\ vs\ N)}$	$E_{\Delta P.c\ (T\ vs\ N)}$
T40C1	624.70	687.57	600.00	3.95	10.07	14.60
T40C3	2,331.00	2,087.48	2,600.00	11.54	10.45	19.71
T40C5	6,786.60	5,091.39	6,100.00	10.12	24.98	16.54
T40C7	14,649.30	10,332.17	11,600.00	20.82	29.47	10.93
T40C9	22,888.70	16,298.44	16,900.00	26.16	28.79	3.56
T50C1	599.50	665.08	600.00	0.08	10.94	10.85
T50C3	2,001.30	1,857.87	2,300.00	14.93	7.17	19.22
T50C5	6,765.60	5,104.29	6,100.00	9.84	24.56	16.32
T50C7	14,441.10	10,211.57	11,500.00	20.37	29.29	11.20
T50C9	23,438.90	16,766.25	17,300.00	26.19	28.47	3.09
T60C1	646.00	691.07	600.00	7.12	6.98	15.18
T60C3	2,032.20	1,882.64	2,300.00	13.18	7.36	18.15
T60C5	6,732.30	5,121.84	6,100.00	9.39	23.92	16.04
T60C7	13,530.80	9,693.33	11,000.00	18.70	28.36	11.88
T60C9	23,937.00	17,146.25	17,600.00	26.47	28.37	2.58
T70C1	700.30	737.80	700.00	0.04	5.36	5.40
T70C3	2,278.00	2,073.57	2,500.00	9.75	8.97	17.06
T70C5	5,742.60	4,490.44	5,400.00	5.97	21.81	16.84
T70C7	14,282.30	10,186.87	11,400.00	20.18	28.68	10.64
T70C9	24,269.00	17,459.06	17,900.00	26.24	28.06	2.46
T80C1	744.80	767.28	700.00	6.02	3.02	9.61
T80C3	2,355.90	2,129.23	2,600.00	10.36	9.62	18.11
T80C5	7,297.10	5,530.12	6,600.00	9.55	24.22	16.21
T80C7	15,244.10	10,930.28	12,200.00	19.97	28.30	10.41
T80C9	23,247.60	16,662.65	17,300.00	25.58	28.33	3.68

Source: Author (2022).

In general, the experimental data showed the highest results, followed by the theoretical and numerical models. According to Silva et al. (2021), the pressure drops results of the theoretical model underestimated the experimental results for the most part presenting a difference of up to 26% for *Re* > 6,000. However, for the laminar regime, the value was less than 15%. On the other hand, for the numerical results, it was the opposite, the smallest differences occurred for *Re* > 6,000 (decreasing with the growth of *Re*) with values below 12%, and for the laminar regime it was similar staying below 20%. The largest difference between numerical and theoretical data was 20% for *Re* ~ 3,000.

Since the deviations occur with increasing Reynolds number in the cold branch, but maintain a similar behavior with increasing temperature in the hot branch. Figure 30 presents the behavior of the pressure drop in the cold branch, it is possible to observe the behavior described above, where the numerical and theoretical models show great agreement as the mass flow rate increases, and on the other hand, the experimental model deviates even more from the other two models with increasing *Re*.

Figure 30 – Theoretical model comparison for the cold branch.

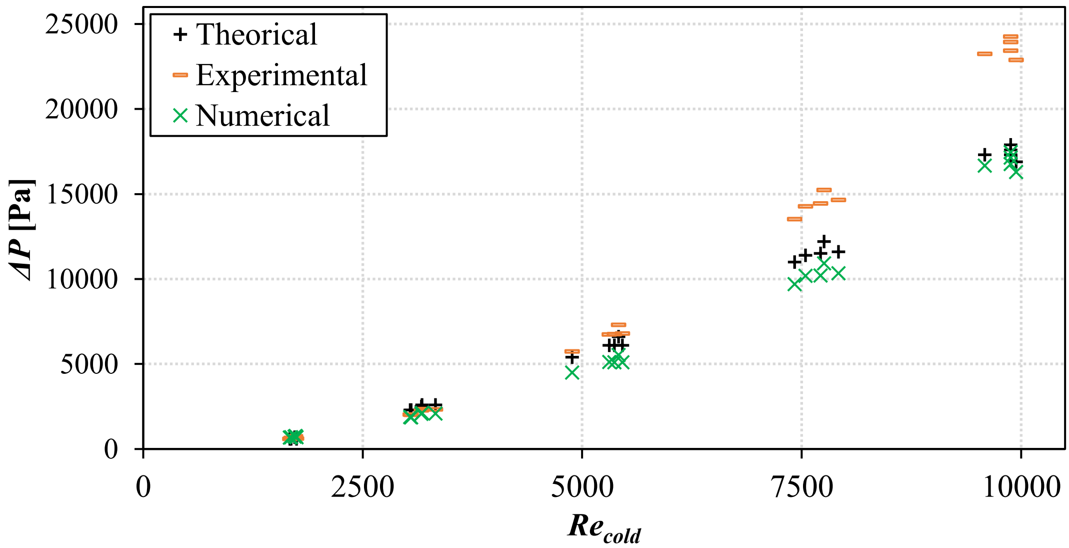

Source: Author (2022).

The great agreement between the theoretical and numerical models for high Reynolds numbers reinforces the suspicion that the channel deformation interferes directly with the pressure drop since both models consider the circular channel with constant geometry, in contrast to the prototype, which presents geometric imperfections in the circular channel, resulting from the manufacturing process. Other causes for the discrepancy in the final results are related to the non-uniform distribution of the flow and the non-uniformity of the diameter along the channel. Thus, a study of individual channels with different geometries is developed in the following sections to verify this hypothesis.

5.2.2 Single Channel Geometry

To validate the numerical model of the single channel with a circular cross-section a comparison of the results with the model of the complete core with circular channels was performed. Table 9 indicates the Nusselt number (*Nu*) for both hot and cold branches. The inlet mass flow and heat transfer rate were divided by the number of channels for each branch (171 channels for the hot branch and 190 channels for the cold branch), so the results for the *Nu* number of the complete core presented in the table below is the average value calculated for a single channel in each branch. The *Nu* number was calculated from Equation 31, described in Chapter 3.

Table 9 – Complete core and single channel comparison of Nusselt number for the heat exchanger of circular cross-section.

Test	Complete Core Result (Circular)		Single Channel Result (Circular)		Difference (Complete vs. Single)	
	Nu_h	Nu_c	Nu_h	Nu_c	$E_{Nu,h}$ [%]	$E_{Nu,c}$ [%]
T60C1	14.44	4.80	13.21	5.09	8.55	5.87
T60C3	14.22	8.43	13.03	7.99	8.41	5.22
T60C5	14.36	14.38	13.15	13.59	8.41	5.46
T60C7	14.32	20.13	13.21	19.13	7.81	4.98
T60C9	14.09	27.26	12.94	25.93	8.17	4.86

Source: Author (2022).

The individual channel showed lower results than the entire core. The hot and cold branches have an average difference of approximately 8% and 5%, respectively, as illustrated in Figure 31, showing good agreement with the previously simulated data of the complete core with circular channels in section 5.2.1. The low average difference in the hot and cold branches suggests that the numerical model can accurately predict the heat transfer conditions.

Figure 31 – Complete core and single channel comparison of Nusselt number for the heat exchanger of circular cross-section: (a) as *Nu* and (b) as a function of Re_{cold}.

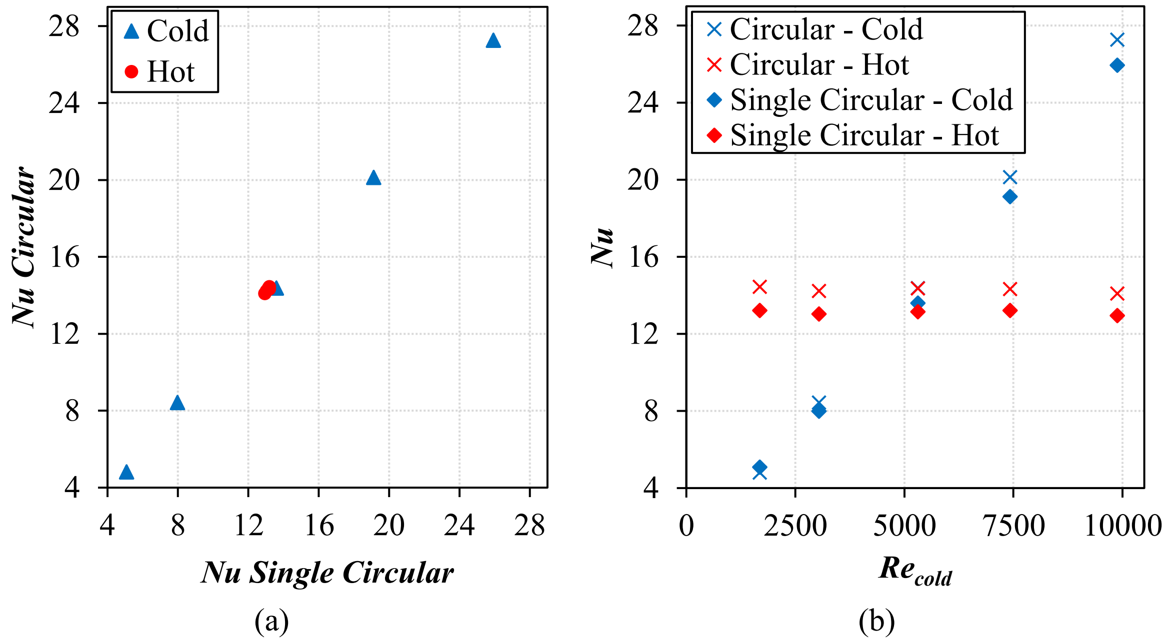

Source: Author (2022).

The pressure drops (ΔP) comparison of the complete core with circular channels and circular single channel results for hot and cold branches is indicated in Table 10. The results demonstrate that the single channel produced lower results than the complete core. In addition, the hot branch showed an average difference of 10% compared to the complete core, while the cold branch showed a mean difference of 18%, reaching a maximum of 24% in the first case (T60C1).

Table 10 – Complete core and single channel comparison of pressure drop for the heat exchanger of circular cross-section.

Test	Complete Core Result (Circular)		Single Channel Result (Circular)		Difference (Complete vs. Single)	
	ΔP_h [Pa]	ΔP_c [Pa]	ΔP_h [Pa]	ΔP_c [Pa]	$E_{\Delta P.h}$ [%]	$E_{\Delta P.c}$ [%]
T60C1	1,387.34	691.07	1,249.13	853.55	9.96	23.51
T60C3	1,360.79	1,882.64	1,224.19	1,698.55	10.04	9.78
T60C5	1,380.64	5,121.84	1,249.13	4,207.92	9.53	17.84
T60C7	1,377.12	9,693.33	1,249.13	7,758.73	9.29	19.96
T60C9	1,347.36	17,146.25	1,211.81	13,635.18	10.06	20.48

Source: Author (2022).

A cause for this behavior is that in the individual channel model, the mass flow rate is applied only at the channel inlet, while in the complete heat exchanger model the mass flow rate is applied at the nozzle inlet. Thus, in each channel of the entire core model, there is a non-uniform distribution of the flow, which results in a different mass flow rate at the inlet of each channel. The non-uniformity of the flow mainly affects the total pressure drop in the heat exchanger, which will be based on the highest pressure drop found.

As discussed earlier, since the mass flow rate is held constant in the hot branch, the pressure drop values are also constant for this branch. The difference compared to the complete core data for the cold branch increases with increasing Reynolds number. The behavior of the two branches, hot and cold, can be seen in Figure 32, which shows the pressure drop results from the comparison of the complete circular core and single circular channel for the five cases studied.

Figure 32 – Complete core and single channel comparison of pressure drop for the heat exchanger of circular cross-section: (a) as pressure drop and (b) as a function of Re_{cold}.

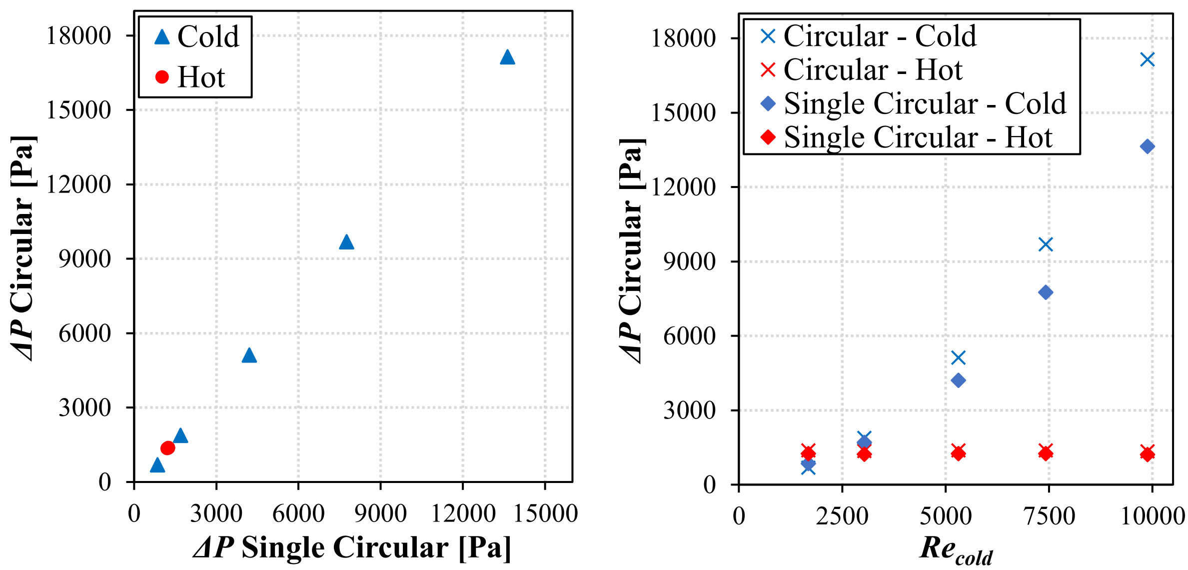

(a) (b)

Source: Author (2022).

Although the cold branch has a difference twice as large as the hot branch, the values found are satisfactory since this was a large model reduction. This result is important for comparing the circular channel and the circular channel with deformed geometry to be presented in later sections of this work.

5.3 CIRCULAR VS. SEMICIRCULAR CROSS-SECTION

In this section, the numerical results of the complete core with circular and semicircular cross-section channels are compared. It is important to highlight here that the same values of hydraulic diameter and heat transfer area from the circular channel were applied to the semicircular channel to make this comparison equivalent.

5.3.1 Heat Transfer Analysis in the Complete Heat Exchanger

The complete core heat exchangers with circular and semicircular cross-sections showed similar behavior and a tiny difference between the heat transfer rate magnitudes. Figure 33 shows the temperature gradient in the two fluid domains, with hot water on the z-axis and cold air on the x-axis for a circular channel (a) and the opposite for a semicircular channel (b), evidencing that the temperature gradient is more intense in the central region (cross-flow).

Figure 33 – Temperature range for circular (a) and semicircular (b) cross-section of complete geometry for case T60C5.

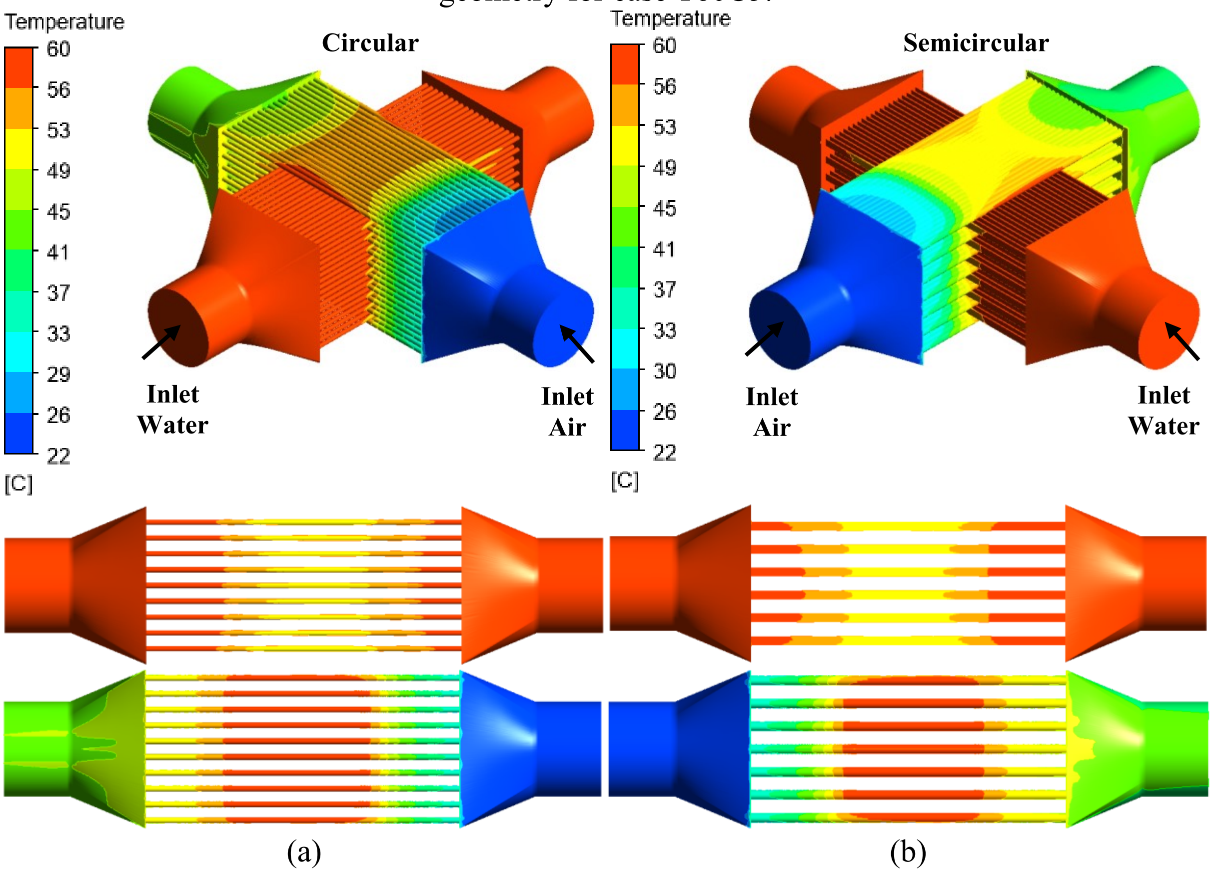

Source: Author (2022).

Due to the high thermal capacity of water, the flow suffers low-temperature variation concerning the value of the inlet and outlet of the branch. On the other hand, the opposite happens with the air, for having a low thermal capacity. It presents a high-temperature variation in the inlet and outlet regions of the branch. It is also noted that heat transfer is facilitated in the air inlet region by the high-temperature difference between the fluids and hampered in the outlet region due to the reduction of this temperature difference.

Table 11 presents the heat transfer rate (q) for the circular and semicircular cross-sections channels results for both hot and cold branches, for the complete heat exchanger. It can be seen that there was an average decrease of 6% in the heat transfer rate for the heat exchanger with the semicircular channels compared to the circular channels for both branches, reaching 11% for Re = 10,000.

Table 11 – Circular vs semicircular heat transfer rate.

Test	**Circular Result**		**Semicircular Result**		**Difference (Cir vs. Sem)**	
	q_h **[W]**	q_c **[W]**	q_h **[W]**	q_c **[W]**	$E_{q.h}$ **[%]**	$E_{q.c}$ **[%]**
T40C1	108.08	108.09	103.19	103.29	4.52	4.43
T40C3	178.15	178.15	168.15	168.14	5.62	5.62
T40C5	256.73	256.72	246.69	246.07	3.91	4.15
T40C7	317.97	317.96	298.27	298.19	6.20	6.22
T40C9	326.76	326.76	298.42	297.96	8.67	8.81
T50C1	152.48	152.48	145.71	145.90	4.44	4.32
T50C3	246.46	246.44	232.14	232.40	5.81	5.70
T50C5	372.23	372.22	355.76	355.79	4.42	4.41
T50C7	449.19	449.18	419.49	419.55	6.61	6.60
T50C9	482.10	482.10	433.67	432.87	10.05	10.21
T60C1	221.32	221.31	212.46	211.87	4.00	4.26
T60C3	350.12	350.11	330.28	330.24	5.67	5.68
T60C5	521.67	521.68	497.97	498.04	4.54	4.53
T60C7	626.81	626.78	585.65	586.67	6.57	6.40
T60C9	713.79	713.78	635.03	634.30	11.03	11.14
T70C1	286.28	286.27	274.90	274.08	3.98	4.26
T70C3	464.77	464.77	439.54	438.50	5.43	5.65
T70C5	631.70	631.71	603.48	602.30	4.47	4.66
T70C7	831.62	831.59	777.07	775.83	6.56	6.71
T70C9	955.89	955.88	847.15	845.89	11.38	11.51
T80C1	344.96	344.94	331.38	330.39	3.94	4.22
T80C3	564.32	564.33	533.97	532.71	5.34	5.60
T80C5	826.77	826.78	791.18	789.69	4.30	4.49
T80C7	1,049.21	1,049.17	976.32	974.70	6.95	7.10
T80C9	1,177.70	1,177.69	1,049.53	1,047.86	10.89	11.02

Source: Author (2022).

Figure 34 illustrates that, for *Re* > 5,500, the difference in the heat transfer increases with Reynolds number growth. Because the results are too close, the hot fluid points are positioned behind the cold fluid points.

Figure 34 – Circular vs semicircular heat transfer rate: (a) as heat transfer rate and (b) as a function of Re_{cold}.

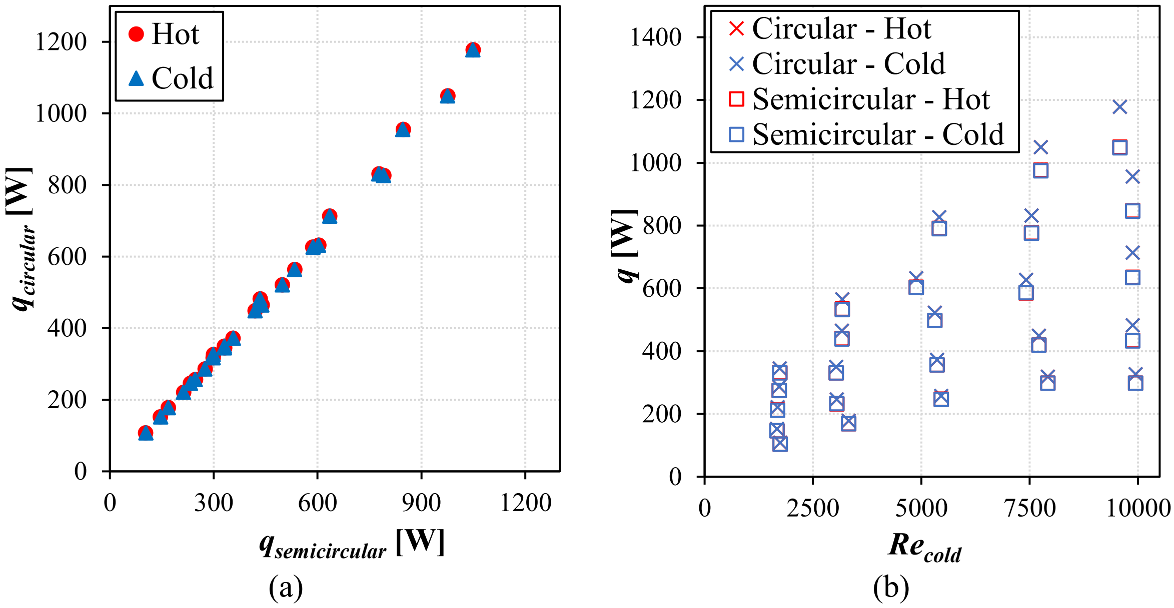

Source: Author (2022).

The discrepancy between the heat transfer rates can be explained by the difference in the geometry of the channel cross-section, where the semicircular geometry ends up causing more recirculation regions because of the non-uniformity of the mass flow rates at the inlet and outlet nozzle (Figure 35), thus generating adverse results and reducing thermal performance. The first two images represent the water branch keeping the mass flow rate constant, and the last two represent the air branch varying the mass flow rate, with hot water on the z-axis and cold air on the x-axis for a circular channel (a) and the opposite for semicircular channel (b).

Figure 35 – Streamline of circular (a) and semicircular (b) cross-section for complete geometry to case T60C5.

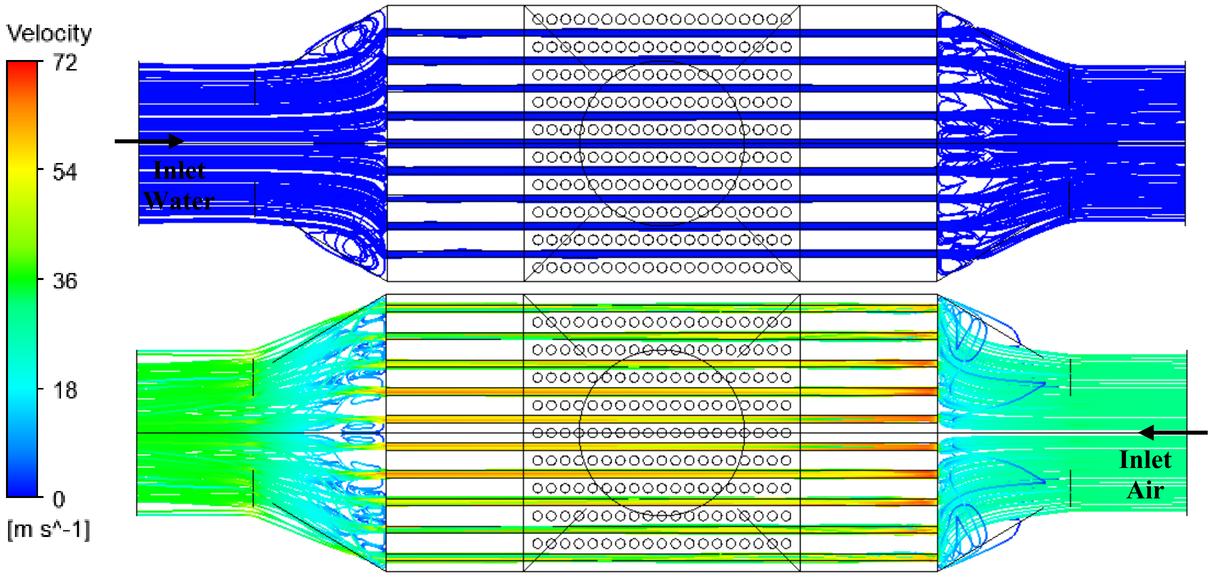

(a)

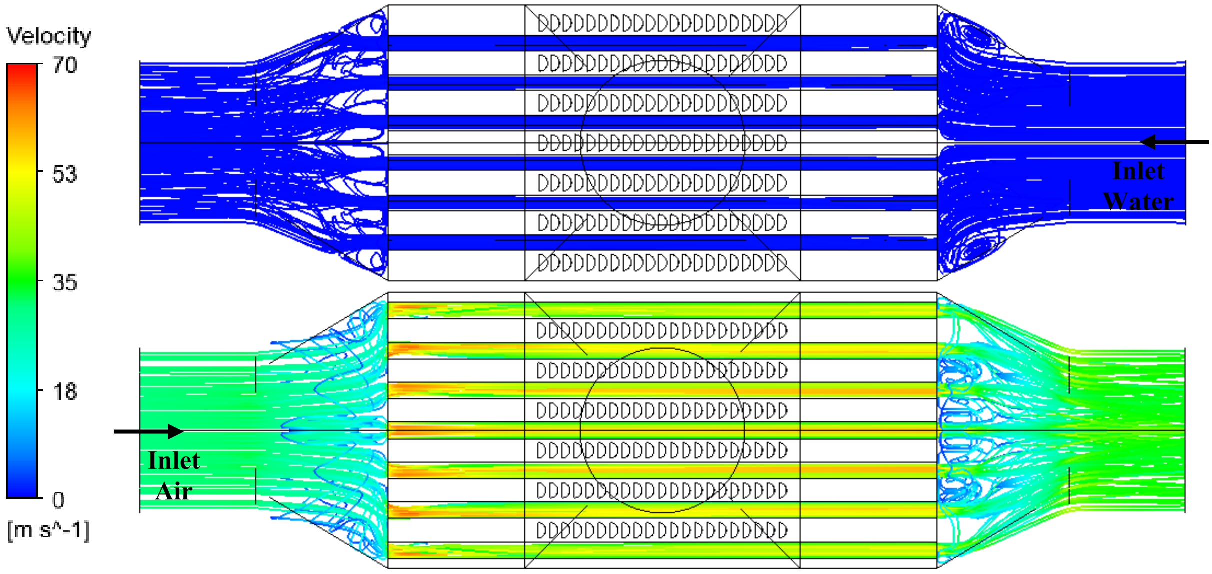

(b)

Source: Author (2022).

A slight advantage is observed in the circular channels over the semicircular ones, presenting a 6% higher mean heat transfer rate. These results are consistent with the fact that the semicircular arrangement has the same heat transfer area as the circular one, but the cross-sectional area of its channel is higher, which reduces the local velocity of the fluid and causes a lower heat transfer rate. However, it is worth noting that in the semicircular configuration, it would be possible to increase the heat exchange area by increasing the number of channels and layers, preserving the same core and nozzles sizes to improve the thermal performance of the heat exchanger.

5.3.2 Pressure Drop Analysis in the Complete Heat Exchanger

The pressure drop (ΔP) follows the same behavior as the heat transfer rate presented above, the total pressure drop for the complete core with semicircular channels decreased compared to the pressure drop for the complete core with circular channels. Figure 36 presents the static pressure gradient in the two fluid domains, with hot water on the z-axis and cold air on the x-axis for a circular channel (a) and the opposite for a semicircular channel (b), demonstrating that the static pressure variation is more intense in the channel region (the core of the heat exchanger) due to the abrupt contraction of the area.

Figure 36 – Pressure range of circular (a) and semicircular (b) cross-section for complete geometry to case T60C5.

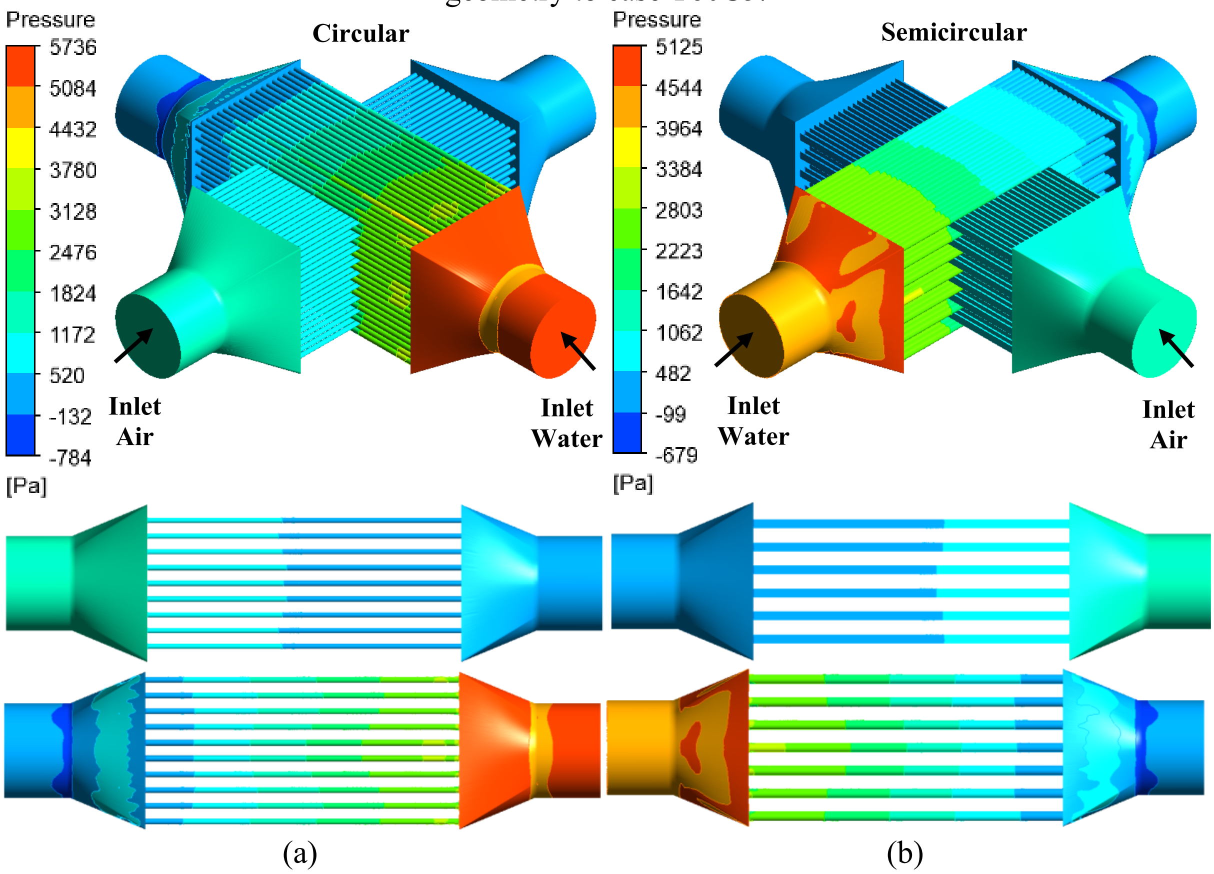

Source: Author (2022).

For a circular channel, in the hot branch, there is a momentary decrease in pressure in the middle of the inlet nozzle and a momentary increase in pressure in the middle of the outlet nozzle due to the transition region of geometry that expands and contracts the area, respectively. It can also be seen that the magnitude of the pressure variation at the inlet nozzle is higher than at the outlet nozzle, although the outlet nozzle has a higher non-uniformity of pressure distribution. This is because the fluid is expanded as it exits the heat exchanger core and is contracted again to exit the nozzle.

It is observable that the hot branch of the semicircular channels presents a more pronounced pressure variation in the nozzles, mainly in the transition region of the geometry that expands/contracts the area. And although the magnitude of the pressure variation at the inlet nozzle is also higher than at the outlet nozzle, unlike the circular channel, the inlet nozzle has a higher number of various sites. This discrepancy is justified by the difference in the geometry of the channel cross-section, which, being semicircular, ended up causing more recirculation regions at the inlet nozzle, as seen previously in Figure 35.

Table 12 shows the pressure drop comparison between the complete core with circular and semicircular channels.

Table 12 – Circular vs semicircular pressure drop.

Test	**Circular Result**		**Semicircular Result**		**Difference (Cir vs. Sem)**	
	ΔP_h **[Pa]**	ΔP_c **[Pa]**	ΔP_h **[Pa]**	ΔP_c **[Pa]**	$E_{\Delta P.h}$ **[%]**	$E_{\Delta P.c}$ **[%]**
T40C1	1,255.20	687.57	1,104.65	558.97	11.99	18.70
T40C3	1,274.17	2,087.48	1,122.16	1,771.31	11.93	15.15
T40C5	1,279.49	5,091.39	1,127.14	4,472.51	11.91	12.16
T40C7	1,295.05	10,332.17	1,141.29	8,909.28	11.87	13.77
T40C9	1,267.08	16,298.44	1,115.51	13,587.59	11.96	16.63
T50C1	1,324.61	665.08	1,168.56	539.23	11.78	18.92
T50C3	1,289.69	1,857.87	1,136.30	1,566.49	11.89	15.68
T50C5	1,263.86	5,104.29	1,112.57	4,483.28	11.97	12.17
T50C7	1,263.22	10,211.57	1,112.29	8,829.16	11.95	13.54
T50C9	1,237.48	16,766.25	1,088.44	13,977.69	12.04	16.63
T60C1	1,387.34	691.07	1,226.43	560.62	11.60	18.88
T60C3	1,360.79	1,882.64	1,202.10	1,586.41	11.66	15.73
T60C5	1,380.64	5,121.84	1,220.67	4,498.40	11.59	12.17
T60C7	1,377.12	9,693.34	1,216.79	8,423.02	11.64	13.11
T60C9	1,347.36	17,146.25	1,189.68	14,298.19	11.70	16.61
T70C1	1,447.11	737.80	1,282.10	599.64	11.40	18.73
T70C3	1,436.70	2,073.57	1,272.44	1,752.23	11.43	15.50
T70C5	1,432.78	4,490.44	1,268.81	3,930.44	11.44	12.47
T70C7	1,446.77	10,186.87	1,281.78	8,841.74	11.40	13.21
T70C9	1,448.48	17,459.06	1,283.37	14,566.19	11.40	16.57
T80C1	1,448.14	767.28	1,283.05	624.08	11.40	18.66
T80C3	1,444.04	2,129.23	1,279.25	1,799.37	11.41	15.49
T80C5	1,419.54	5,530.12	1,256.54	4,862.39	11.48	12.07
T80C7	1,405.67	10,930.28	1,243.70	9,462.69	11.52	13.43
T80C9	1,390.86	16,662.65	1,229.99	13,979.29	11.57	16.10

Source: Author (2022).

For the semicircular channels, the hot branch exhibits a 12% average decrease in pressure drop relative to the circular channels, and the cold branch presents an average decrease of 15%. Interestingly, in the cold branch, the higher difference occurs at the lowest Reynolds number reaching 19%, followed by a drop in the middle *Re* values and again increasing with the growth of *Re*. The results are consistent with the idea that since the cross-section area is higher for the same hydraulic diameter in the semicircular channel, less pressure drop is expected when compared to the same hydraulic diameter circular channel.

The behavior of the two branches (hot and cold) is illustrated in Figure 37, showing the comparison of the pressure drop results of the circular and semicircular cross-section channels for the twenty-five cases studied.

Figure 37 – Circular vs semicircular pressure drop: (a) as pressure drop and (b) as a function of Re_{cold}.

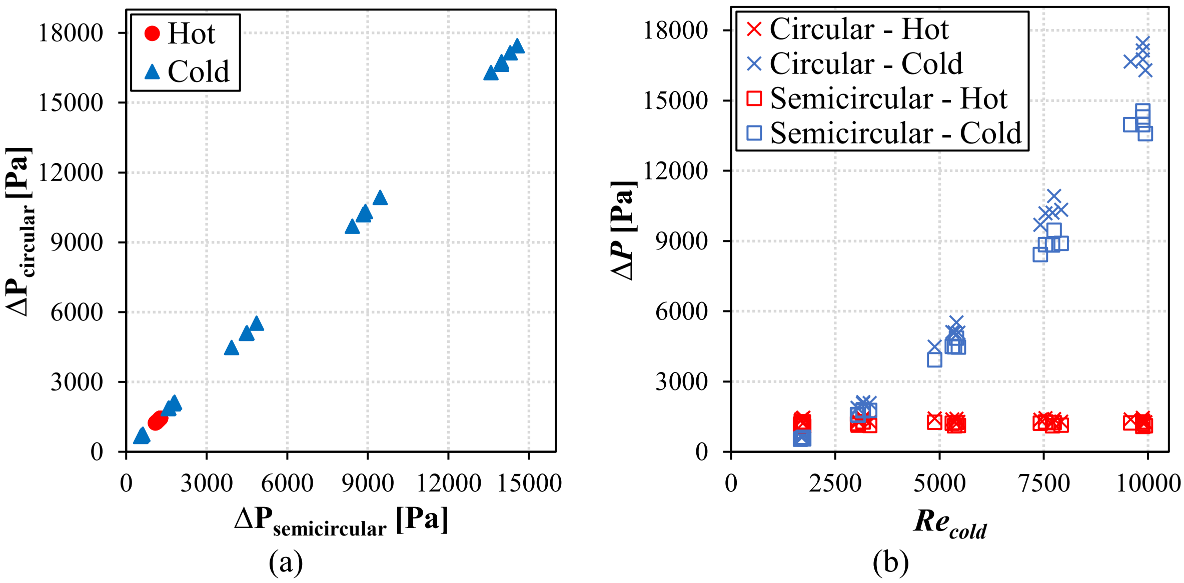

Source: Author (2022).

To investigate the pressure drops further, the total pressure drop presented above was decomposed into inlet, core, and outlet losses by positioning planes along the branches for both channel arrangements. The planes were positioned in the transition regions of the nozzle area and at the inlet and outlet of the core, as depicted in Figure 38 (a). Table 26 (hot branch) and Table 27 (cold branch) in APPENDIX C present the pressure values per plane for the circular channels. Table 28 (hot branch) and Table 29 (cold branch) in APPENDIX C present the pressure values per plane for semicircular channels. Figure 38 (b) illustrates the comparison between the numerical results showing the evolution of the static pressure variation relative to the inlet along the branch for the T60C5 case (Re = 5,310). According to the concept of Shah and Sekulić (2003), it is possible to observe the significant reduction of static pressure at the inlet of the heat exchanger core due to the abrupt contraction that accelerates the flow, followed by the linear pressure drop along the channels due to friction and the static pressure increase at the core outlet due to the abrupt expansion and consequent deceleration of the flow. Therefore, it is concluded that the core is responsible for the greatest resistance to the flow, being the main contribution to the static pressure variation due to the abrupt contraction of the area and the friction along the channels.

Figure 38 – Positioning planes along the system (a) and analysis of the pressure drop of the circular and semicircular cross-section for complete geometry to case T60C5 (b).

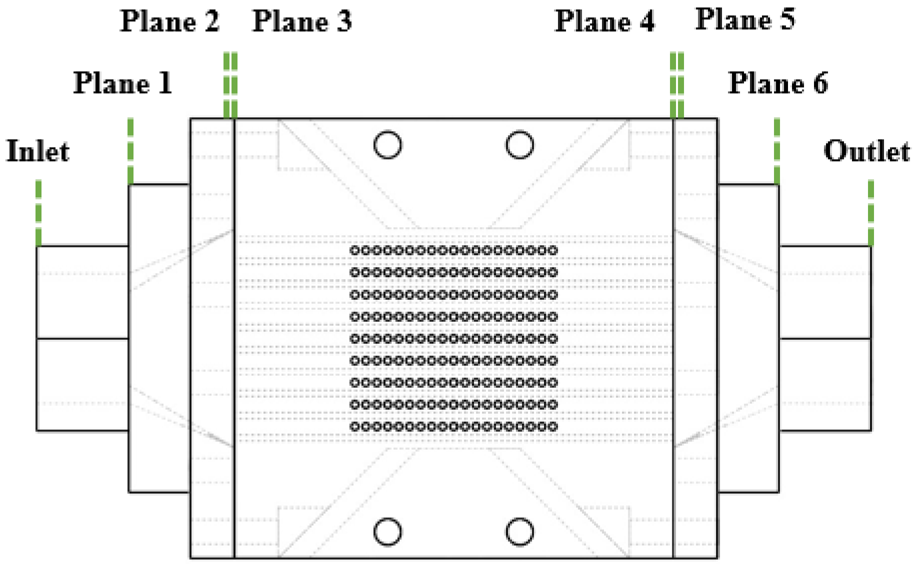

(a)

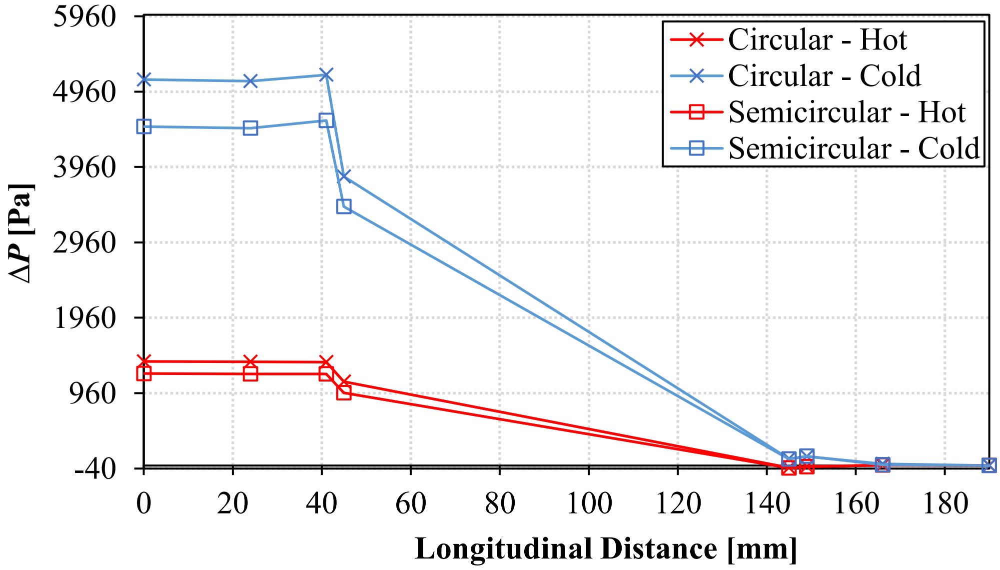

(b)

Source: Author (2022).

The numerical results show an average of 83% and 73% pressure drop in the core with circular channels for the hot and cold branches, respectively. For the core with semicircular channels, the pressure drop is 82% for the hot branch and 74% for the cold branch. These results are in good agreement with the experimental data of Silva et al. (2021), which show that the core is responsible for approximately 87% of the total pressure drop and the other singularities (e.g., inlet and outlet nozzles, tee) are responsible for the remaining 13%.

Due to the same hydraulic diameter and heat transfer area, the channels with circular and semicircular cross-sections exhibited similar results. It was observed that the circular channels presented a higher heat transfer rate and higher pressure drop, but in the semicircular configuration, it would be possible to increase the number of channels and layers since this configuration of semicircular channels occupies less space in the core than the circular channel configuration, thus improving the thermos-hydraulic performance of the heat exchanger. It is crucial to note that an increased number of semicircular channels within the same core can impact the structural behavior of the heat exchanger, which has non analyzed in this study. Additionally, the use of a semicircular arrangement may increase fouling due to the presence of sharp corners.

5.4 SINGLE CHANNEL GEOMETRIES

This section investigates the effects of channel cross-section geometry on Nusselt number (*Nu*) and pressure drop for the three geometries shown in Figure 18 in section 4.2.1. Only a two-channel set of each configuration is modeled in this section. All models apply the likewise value of inlet mass flow and prescribed heat transfer flux in each channel. It also considers the same hydraulic diameter for each channel. Table 13 indicates the *Nu* for both branches (hot and cold), for channels with cross-section: circular, deformed circular (depression at the top of the cylinder), and chaotic circular with a V-shaped path with 55° inclination to the horizontal.

Table 13 – Nusselt number comparison of the single channel geometries.

Test	Nu_h	Nu_c	Nu_h	Nu_c	$E_{Nu.h}$ [%]	$E_{Nu,c}$ [%]
	Circular		**Circular Deformed**		**C vs. DC**	
T60C1	13.21	5.09	13.28	5.12	0.51	0.65
T60C3	13.03	7.99	13.09	8.08	0.50	1.23
T60C5	13.15	13.59	13.28	13.74	0.95	1.10
T60C7	13.21	19.13	13.27	19.35	0.51	1.19
T60C9	12.94	25.93	13.01	26.49	0.52	2.15
Test	**Circular**		**V-shape Inclined**		**C vs. VI**	
T60C1	13.21	5.09	25.73	8.56	94.85	68.32
T60C3	13.03	7.99	25.46	13.12	95.39	64.26
T60C5	13.15	13.59	25.73	22.96	95.70	68.91
T60C7	13.21	19.13	25.73	33.42	94.82	74.73
T60C9	12.94	25.93	25.32	46.61	95.70	79.72

Source: Author (2022).

The deformation of circular channels can have multiple impacts on heat transfer in a heat exchanger, including both convection and conduction, ultimately influencing the efficiency of the heat exchanger. However, compared to perfectly circular channels, the deformed circular channel shows an average difference of 1% in the Nusselt number in both branches, with a maximum of 1% for the hot and 2% for the cold branches, showing slightly higher *Nu* values.

Compared to the single circular channel, the chaotic channel showed an increase of about 95% in the *Nu* number for the hot branch and 71% for the cold branch, achieving the maximum of 80%. The three-dimensional geometry of the channels can affect heat transfer due to variations in the characteristics of the fluid flow along the x, y, and z axes. This includes variations in turbulence and effective thermal conductivity of the channel wall, which can affect convective and conduction heat transfer, respectively, and affect the efficiency of the heat exchanger.

The Nusselt number behavior for the three geometries studied is illustrated in Figure 39.

Figure 39 – Nusselt number comparison of the single channel geometries: (a) as *Nu* and (b) as a function of Re_{cold}.

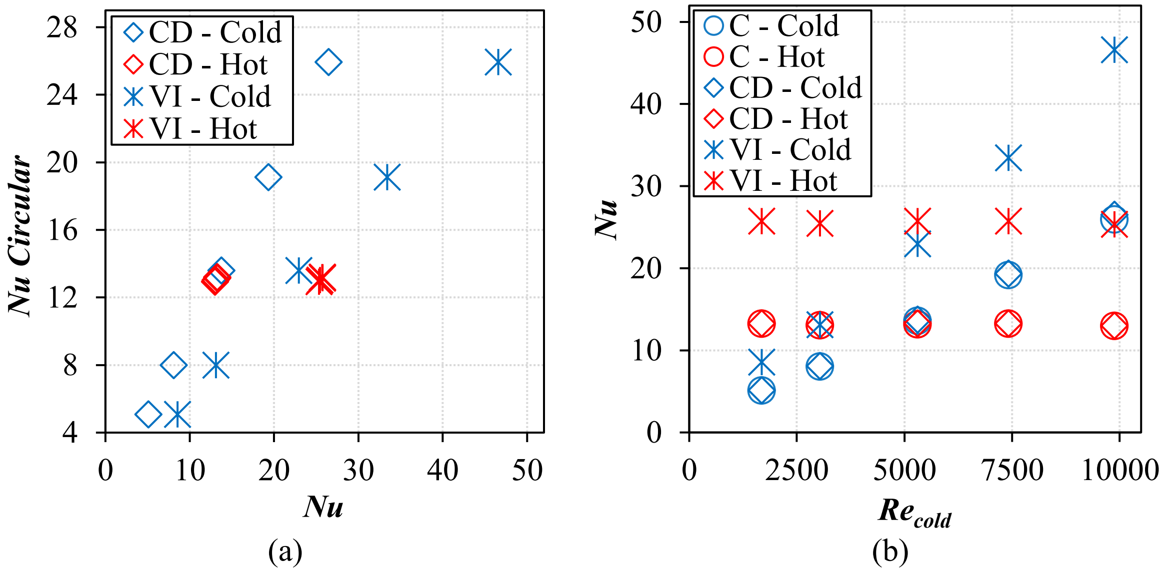

Source: Author (2022).

Table 14 exhibits the comparison of the pressure drop for the three geometries studied, where all three channel configurations had an increase in pressure drop compared to the circular channel. The deformed circular channel showed a 9% and 11% increase relative to the circular channel for the hot and cold branches, respectively. Thus, the suspicion that the circularity of the channel directly interferes with the pressure drop results is confirmed. In the single-channel models, the same inlet mass flow is prescribed for all configurations while in the complete heat exchanger model, the prescribed inlet mass flow is the same at the nozzle inlet. For each channel in the complete heat exchanger model, a non-uniform distribution of mass probably occurs, leading to different mass flow inlets in each channel. The total pressure drop in the heat exchanger is then affected by this non-uniformity since the pressure drop will be based on the higher pressure drop encountered in the heat exchanger.

The chaotic channel shows a 284% and 469% increase in the magnitude of the pressure drop for the hot and cold branches, respectively, compared to the individual circular channel. In the case of the chaotic channel, its geometry is more complex than that of the circular channel, which increases the resistance to fluid flow. This causes the fluid velocity to decrease, and consequently, the fluid pressure also decreases. As a result, there is a greater magnitude of pressure drop in the chaotic channel compared to the individual circular channel.

Table 14 – Pressure drop comparison of the single channel geometries.

Test	ΔP_h [Pa]	ΔP_c [Pa]	ΔP_h [Pa]	ΔP_c [Pa]	$E_{\Delta P.h}$ [%]	$E_{\Delta P.c}$ [%]
	Circular		**Circular Deformed**		**C vs. DC**	
T60C1	1,249.13	853.55	1,358.28	941.91	8.74	10.35
T60C3	1,224.19	1,698.55	1,331.28	1,883.03	8.75	10.86
T60C5	1,249.13	4,207.92	1,358.28	4,669.30	8.74	10.97
T60C7	1,249.13	7,758.73	1,358.28	8,628.42	8.74	11.21
T60C9	1,211.81	13,635.18	1,317.88	15,175.86	8.75	11.30
Test	**Circular**		**V-shape Inclined**		**C vs. VI**	
T60C1	1,249.13	853.55	4,804.68	4,600.11	284.64	438.94
T60C3	1,224.19	1,698.55	4,703.48	9,758.30	284.21	474.51
T60C5	1,249.13	4,207.92	4,804.68	25,138.27	284.64	497.40
T60C7	1,249.13	7,758.73	4,804.68	45,817.95	284.64	490.53
T60C9	1,211.81	13,635.18	4,646.21	73,836.38	283.41	441.51

Source: Author (2022).

The behavior described above is illustrated in Figure 40, which shows the comparison of the pressure drop for the three geometries studied.

Figure 40 – Pressure drop comparison of the single channel geometries: (a) as pressure drop and (b) as a function of Re_{cold}.

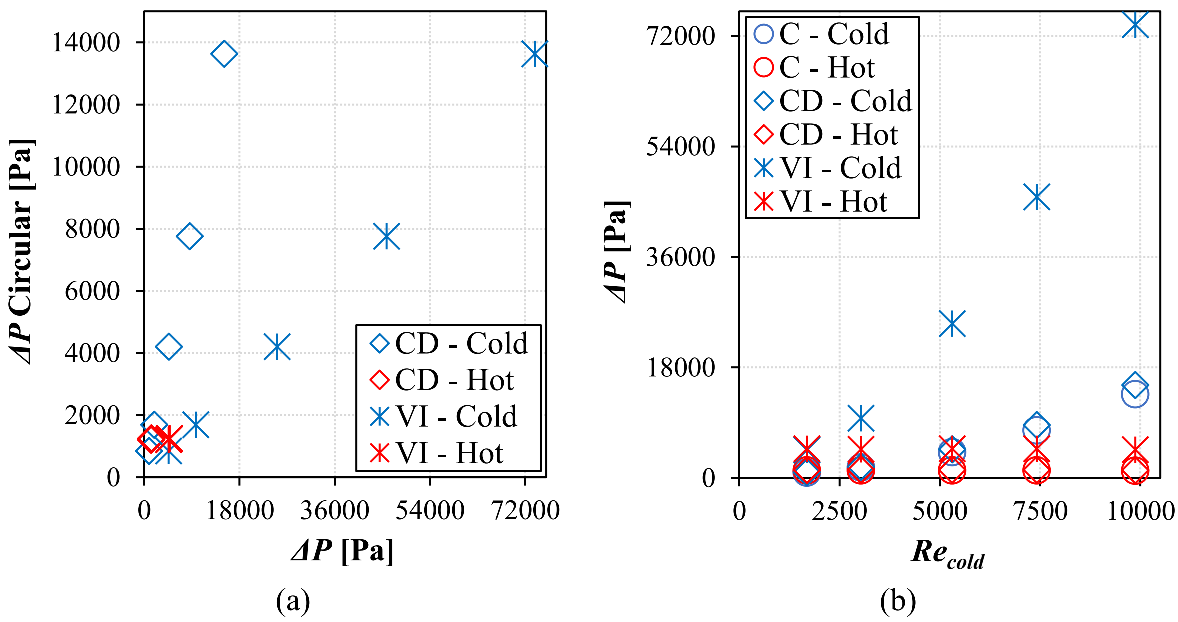

Source: Author (2022).

The main results achieved in this section point out that the shape of the channel cross-section directly interferes with the pressure drop. This is a probable cause of the elevated difference between the pressure drop encountered when comparing the experimental results for the complete circular channel heat exchanger and the numerical model presented in this work.

Also, it indicates what differences it would be found in the modeling of single channels compared to the complete heat exchanger with different channel configurations. However, when comparing the individual channel models to the complete heat exchanger model is possible to conclude that other variables such as non-uniformity of flow distribution inside the heat exchanger and geometric design of the core highly affect the practical results for actual equipment and should be taken into account for design purposes.

6 CONCLUSIONS

To numerically analyze the thermal-hydraulic performance of a heat exchanger, two numerical models were developed for a compact cross-flow heat exchanger with straight mini-channels. The first model corresponds to the SLMHE prototype with circular cross-section channels, as the second model is a variation of the first by replacing the circular configuration with semicircular ones, maintaining the same hydraulic diameter and heat transfer area. Subsequently, to conduct a study on the effects of channel cross-section geometry on heat transfer and pressure drop, three numerical models were developed for individual channels of different geometries, including the straight circular, the straight deformed circular (depression at the top of the cylinder), and the V-shaped chaotic circular inclined at 55° with the horizontal, all with the same hydraulic diameter and length of the complete core channel.

Water and air were used, as working fluids for the hot and cold branches, respectively. As boundary conditions, temperature and mass flow rate at the inlets, static pressure equal to zero at the outlets, a rough wall with conservative heat flux at the fluid-solid interfaces, and adiabatic wall at the external walls of the nozzles and heat exchanger core, were adopted. The analyses were performed using the ANSYS 18.2 software, through the ICEM CFD, MESH, and CFX modules, applying the SST turbulence model, with residual convergence criteria target of 10^{-6} RMS and conservation target of 0.01 (1%).

The numerical model validation of the complete heat exchanger core occurred using experimental data. Numerical results demonstrate that the complete core with circular cross-section channel compared to the experimental data shows an average difference for the heat transfer rate in the value of 5% and 10%, with lower results in the hot and higher in the cold branches. For pressure drop, it shows an average reduction of 35% on the hot side and 19% on the cold side. The errors increased with the increase in the number of Reynolds.

The confirmation that channel shape directly impacts pressure drop occurs by comparing the cold branch of the experimental, theoretical, and numerical models. Observed optimum agreement between the numerical and theoretical models, for a high Reynolds number, shows a difference of 14% since both consider the circular channel with constant geometry, unlike the actual prototype that presents geometric imperfections in the circular arrangement arising from the manufacturing process (diameter variation and circularity along the path) which, in turn, exhibits a discrepancy of 26% compared to the theoretical model. The irregular distribution of the flows and the non-uniformity of the channel diameter is associated with the differences between the final results, besides channel deformation.

The channels with circular and semicircular cross-sections showed similar results due to the same hydraulic diameter and heat transfer area, with the semicircular configuration having a slight advantage over the circular one exhibiting a 6% lower average heat transfer rate for both branches, but a lower pressure drop, with a difference of 12% for the hot side and 15% for the cold side. Through the more detailed study of the pressure drop along the branches, it was possible to see that the highest pressure drop occurs in the heat exchanger core, which for the circular channels presents an average pressure drop of 83% and 73% for the hot and cold branches, respectively. For the semicircular arrangement, the pressure drop is 82% on the hot side and 74% on the cold side. These results coincide with the experimental data, which showed an average of 87% in pressure drop of the core.

It is worth noting that in the semicircular configuration, it would be possible to increase the heat exchange area by increasing the number of channels and layers, preserving the likewise size of the core and nozzles to improve the thermal-hydraulic performance of the heat exchanger. However, it´s essential to consider that increasing the number of semicircular channels may impact the structural behavior of the heat exchanger, which was non analyzed in this study. In addition, a semicircular arrangement may favor fouling due to the sharp corners.

The single-channel with circular cross-section numerical model validation was performed by comparing its results with the complete core numerical model with circular channels. The individual channel showed lower results than the entire core for Nusselt number (Nu) and pressure drop. For Nu, the average difference was 8% on the hot and 5% on the cold branches. For pressure drop, the hot side showed an average difference of 10%, while the cold side showed an average difference of 18%.

The investigation of the influence of the shape of the channel cross-section on the thermal-hydraulic performance, performed using single channels, indicates that the shape of the channel cross-section directly interferes with the pressure drop. Nevertheless, in heat transfer, this influence is less significant. For the Nusselt number, the deformed circular channel showed higher results than the circular one, presenting an average difference of 1% in both branches. The chaotic configuration shows an increase of 95% on the hot and 71% on the cold sides. Regarding pressure drop, the deformed circular channel exhibits an increase of 9% and 11% compared to the circular for the hot and cold branches, respectively. And the chaotic arrangement had a 284% increase on the hot side and 469% on the cold side. These results confirm that the shape of the channel cross-section directly affects the pressure drop and justifies the differences between the experimental and numerical results for the complete core with circular channels.

The V-shaped chaotic circular arrangement showed the highest values of Nu and pressure drop, followed by deformed straight circular and straight circular. Although the chaotic channel showed a significant increase in heat transfer compared to the straight circular channel, the increase in pressure drop was much higher, making this arrangement unfavorable for this application.

Recommendations for future work:

- Perform the simulation of the actual model of the manufactured prototype by scanning the deformation of the channels;
- Evaluation of the thermal-hydraulic performance of the complete core for the other configurations studied in the individual channels;
- Conduct a further study on chaotic channels by increasing the number of geometries, changing the shape of the channel path and the shape of the cross-section to raise the thermal-hydraulic performance of the current prototype;
- Study the fouling along the channels of all the proposed geometries;
- Develop the numerical structural analysis study for all the configurations mentioned above.

BIBLIOGRAPHY

BLAZEK, J. **Computational fluid dynamics: Principles and applications.** 3. ed. Sankt Augustin: Elsevier, 2015. 447 p.

CASTELAIN, Cathy; LASBET, Yahia; AUVITY, Bruno; PEERHOSSAINI, Hassan. Experimental study of the thermal performance of chaotic geometries for their use in PEM fuel cells. **International Journal of Thermal Sciences**, [S.L.], v. 101, p. 181-192, mar. 2016. Elsevier BV. http://dx.doi.org/10.1016/j.ijthermalsci.2015.10.033.

CHAI, Lei; A TASSOU, Savvas. Numerical study of the thermohydraulic performance of printed circuit heat exchangers for supercritical CO2 Brayton cycle applications. **Energy Procedia**, [S.L.], v. 161, p. 480-488, mar. 2019. Elsevier BV. http://dx.doi.org/10.1016/j.egypro.2019.02.066.

CHAI, Lei; TASSOU, Savvas A.. A review of printed circuit heat exchangers for helium and supercritical CO2 Brayton cycles. **Thermal Science and Engineering Progress**, [S.L.], v. 18, p. 100543, ago. 2020. Elsevier BV. http://dx.doi.org/10.1016/j.tsep.2020.100543.

CHU, Wen-Xiao; BENNETT, Katrine; CHENG, Jie; CHEN, Yi-Tung; WANG, Qiu-Wang. Numerical study on a novel hyperbolic inlet header in straight-channel printed circuit heat exchanger. **Applied Thermal Engineering**, [S.L.], v. 146, p. 805-814, jan. 2019. Elsevier BV. http://dx.doi.org/10.1016/j.applthermaleng.2018.10.027.

ÇENGEL A, Y.. **Heat and mass transfer: A practical approach.** 3. ed. Boston: Mcgraw-hill, 2007.

FIGLEY, Justin; SUN, Xiaodong; MYLAVARAPU, Sai K.; HAJEK, Brian. Numerical study on thermal hydraulic performance of a Printed Circuit Heat Exchanger. **Progress In Nuclear Energy**, [S.L.], v. 68, p. 89-96, set. 2013. Elsevier BV. http://dx.doi.org/10.1016/j.pnucene.2013.05.003.

GÖLTAş, Merve; GÜREL, Barış; KEÇEBAş, Ali; AKKAYA, Volkan Ramazan; GÜLER, Onur Vahip. Improvement of thermo-hydraulic performance with plate surface geometry for a compact plate heat exchanger manufactured by additive manufacturing. **International Journal of Heat and Mass Transfer**, [S.L.], v. 188, p. 122637, jun. 2022. Elsevier BV. http://dx.doi.org/10.1016/j.ijheatmasstransfer.2022.122637.

GONG, Guanghao; YE, Jiajia; CHI, Yiming; ZHAO, Zhihuan; WANG, Zifan; XIA, Guang; DU, Xueyun; TIAN, Hongfang; YU, Huijun; CHEN, Chuanzhong. Research status of laser additive manufacturing for metal: a review. **Journal of Materials Research and Technology**, [S.L.], v. 15, p. 855-884, nov. 2021. Elsevier BV. http://dx.doi.org/10.1016/j.jmrt.2021.08.050.

HESSELGREAVES, John E.; LAW, Richard; REAY, David A.. **COMPACT HEAT EXCHANGERS: Selection, design and operation.** 2. ed. Uk: Elsevier, 2017.

HÖGANÄS. **316L Material data sheet. 2022.** Available at: https://digitalmetal.tech/wp-content/uploads/2021/11/DIM0108_Data-sheet-316L.pdf. Accessed on: 10 jan. 2022.

HUANG, Changye; CAI, Weihua; WANG, Yue; LIU, Yao; LI, Qian; LI, Biao. Review on the characteristics of flow and heat transfer in printed circuit heat exchangers. **Applied Thermal Engineering**, [S.L.], v. 153, p. 190-205, maio 2019. Elsevier BV. http://dx.doi.org/10.1016/j.applthermaleng.2019.02.131.

JAMSHED, Shamoon. **Using HPC for computational fluid dynamics: A guide to high performance computing for CFD engineers.** Waltham: Elsevier, 2015. 213 p.

JEON, Sangwoo; BAIK, Young-Jin; BYON, Chan; KIM, Woojin. Thermal performance of heterogeneous PCHE for supercritical CO2 energy cycle. **International Journal of Heat and Mass Transfer**, [S.L.], v. 102, p. 867-876, nov. 2016. Elsevier BV. http://dx.doi.org/10.1016/j.ijheatmasstransfer.2016.06.091.

JING, Qi; XIE, Yonghui; ZHANG, Di. Thermal hydraulic performance of printed circuit heat exchanger with various channel configurations and arc ribs for SCO2 Brayton cycle. **International Journal of Heat and Mass Transfer**, [S.L.], v. 150, p. 119272, abr. 2020. Elsevier BV. http://dx.doi.org/10.1016/j.ijheatmasstransfer.2019.119272.

KAKAÇ, Sadik; LIU, Hongtan; PRAMUANJAROENKIJ, Anchasa. **Heat Exchangers: Selection, Rating and Thermal Design.** 3. ed. New York: Taylor & Francis Group. Llc, 2012. 624 p.

KAUR, Inderjot; SINGH, Prashant. State-of-the-art in heat exchanger additive manufacturing. **International Journal of Heat and Mass Transfer**, [S.L.], v. 178, p. 121600, out. 2021. Elsevier BV. http://dx.doi.org/10.1016/j.ijheatmasstransfer.2021.121600.

KHALIL, Mohamad; ALI, Mohamed I. Hassan; KHAN, Kamran A.; AL-RUB, Rashid Abu. Forced convection heat transfer in heat sinks with topologies based on triply periodic minimal surfaces. **Case Studies in Thermal Engineering**, [S.L.], v. 38, p. 102313, out. 2022. Elsevier BV. http://dx.doi.org/10.1016/j.csite.2022.102313.

KIM, Woojin; BAIK, Young-Jin; JEON, Sangwoo; JEON, Daechan; BYON, Chan. A mathematical correlation for predicting the thermal performance of cross, parallel, and counterflow PCHEs. **International Journal of Heat and Mass Transfer**, [S.L.], v. 106, p. 1294-1302, mar. 2017. Elsevier BV. http://dx.doi.org/10.1016/j.ijheatmasstransfer.2016.10.110.

LASBET, Yahia; AUVITY, Bruno; CASTELAIN, Cathy; PEERHOSSAINI, Hassan. Thermal and Hydrodynamic Performances of Chaotic Mini-Channel: application to the fuel cell cooling. **Heat Transfer Engineering**, [S.L.], v. 28, n. 8-9, p. 795-803, ago. 2007. Informa UK Limited. http://dx.doi.org/10.1080/01457630701328908.

LIU, Guangxu; HUANG, Yanping; WANG, Junfeng; LIU, Ruilong. A review on the thermal-hydraulic performance and optimization of printed circuit heat exchangers for supercritical CO2 in advanced nuclear power systems. **Renewable and Sustainable Energy Reviews**, [S.L.], v. 133, p. 110290, nov. 2020. Elsevier BV. http://dx.doi.org/10.1016/j.rser.2020.110290.

MALISKA, C. R. **Transferência de Calor e Mecânica dos Fluidos Computacional.** 2.ed. Florianópolis: LTC, 2012. ISBN-10: 9798521613961

MENG, Bao; WAN, Min; ZHAO, Rui; ZOU, Zhengping; LIU, Huoxing. Micromanufacturing technologies of compact heat exchangers for hypersonic precooled airbreathing propulsion: a review. **Chinese Journal of Aeronautics**, [S.L.], v. 34, n. 2, p. 79-103, fev. 2021. Elsevier BV. http://dx.doi.org/10.1016/j.cja.2020.03.028.

MENTER, F.; C. F. J.; ESCH, T.; KONNO, B. The SST turbulence model with improved wall treatment for heat transfer prediction in gas turbines. **International gas turbine congress.** GTSJ, 2003.

RANGANAYAKULU, C.; SEETHARAMU, K.N.. **Compact Heat Exchangers: Analysis, design and optimization using fem and CFD approach**. Hoboken, Nj: John Wiley & Sons Ltd, 2018. 527 p.

REN, Zhuo; ZHAO, Chen-Ru; JIANG, Pei-Xue; BO, Han-Liang. Investigation on local convection heat transfer of supercritical CO2 during cooling in horizontal semicircular channels of printed circuit heat exchanger. **Applied Thermal Engineering**, [S.L.], v. 157, p. 113697, jul. 2019. Elsevier BV. http://dx.doi.org/10.1016/j.applthermaleng.2019.04.107.

SANDMEYER. **Specification Sheet: Alloy 316/316L.** 2014. Available at: https://www.sandmeyersteel.com/images/316-316L-317L-Spec-Sheet.pdf. Accessed on: 10 jan. 2022.

SHAH, Ramesh K.; SEKULIC, Dusan P.. **Fundamentals of Heat Exchanger Design.** Hoboken, New Jersey: John Wiley & Sons, 2003.

SILVA, Ramon Peruchi Pacheco da. **Analise térmica e hidrodinâmica de trocadores de calor compactos fabricados por manufatura aditiva.** 2021. 116 f. Dissertation (Master's degree) - Postgraduate Program in Engineering and Mechanical Sciences, Joinville Campus, Federal University of Santa Catarina, Joinville, 2021. Available at: https://repositorio.ufsc.br/handle/123456789/231137. Accessed on: 30 dez. 2021.

SILVA, R.P.P. da; MORTEAN. M.V.V.; PAIVA. K.V. de; BECKEDORFF. L.e.; OLIVEIRA. J.L.G.; BRANDÃO. F.G.; MONTEIRO. A.s.; CARVALHO. C.s.; OLIVEIRA. H.R.; BORGES. D.G.. Thermal and hydrodynamic analysis of a compact heat exchanger produced by additive manufacturing. **Applied Thermal Engineering**. [S.L.], v. 193, p. 116973, jul. 2021. Elsevier BV. http://dx.doi.org/10.1016/j.applthermaleng.2021.116973.

TASCHECK, Bruna Larissa. **Numerical analysis of hydrodynamic characteristics of a plate and shell heat exchanger (PSHE)**. 2019. 102 f. Dissertation (Master's degree) - Postgraduate Program in Engineering and Mechanical Sciences, Joinville Campus, Federal University of Santa Catarina, Joinville, 2019. Available at: https://repositorio.ufsc.br/handle/123456789/220053. Accessed on: 13 oct. 2021.

THULUKKANAM, K.. **Heat exchanger design handbook: Mechanical Engineering.** 2. ed. New York: Crc Press, 2013. 1260 p.

TU, Jiyuan; YEOH, Guan-Heng; LIU, Chaoqun. **Computational Fluid Dynamics: A practical approach.** 3. ed. Oxford, United Kingdom: Elsevier, 2018. 477 p.

WHITE, Martin T.; BIANCHI, Giuseppe; CHAI, Lei; TASSOU, Savvas A.; SAYMA, Abdulnaser I.. Review of supercritical CO: math xmlns. **Applied Thermal Engineering**, [S.L.], v. 185, p. 116447, fev. 2021. Elsevier BV. http://dx.doi.org/10.1016/j.applthermaleng.2020.116447.

WILCOX, David C.. **Turbulence modeling for CFD**. 3. ed. San Diego: DCW Industries, 2006. 515 p.

ZILIO, G.; TEIXEIRA, M.J.; MORTEAN, M.V.V.; BRANDÃO, F.G.; PONTIN, T.T.; OLIVEIRA, J.L.G.; PAIVA, K.V.. Structural analysis of compact heat exchanger samples fabricated by additive manufacturing. **International Journal of Pressure Vessels and Piping**, [S.L.], v. 199, p. 104714, out. 2022. Elsevier BV. http://dx.doi.org/10.1016/j.ijpvp.2022.104714.

ZOHURI, Bahman. **Compact Heat Exchangers: Selection, application, design and evaluation.** Albuquerque: Springer, 2017. 559 p.

APPENDIX A – Additional Literature Review Data

Other similar papers were performed on the thermo-hydraulic performance of straight channel PCHEs and a summary of these studies is shown in Table 15, in chronological order. A list of heat transfer and friction factor correlations for PCHEs with semicircular straight channels is displayed in Table 16.

Table 15 – Representative thermo-hydraulic performance studies of straight-channel PCHEs.

Reference	Description	Configuration	Parameters	Measured characteristics
Mylavarapu et al. (2009)	Alloy 617; He-He in cc; N	$n = 120$; $D_h = 1.22$ mm; $A_H = 0.188$ m^2; $A_C = 0.168$ m^2	$\dot{m} = 15.\ 40.\ 80$ kg/h $T_{H.in} = 900$ °C; $T_{C.in} = 540$ °C $P_{out} = 3$ MPa	Pressure drop; Overall heat-transfer coefficient.
Li et al. (2011)	CO_2–H_2O; E + N	-	$P_H = 7.5$–10 MPa $T_H = 10$–90 ∘C	Heat transfer correlation with property ratio correction terms was developed.
Kruizenga et al. (2011)	CO_2–H_2O; E	-	$P_H = 7.5$–8.1 MPa $T_H = 17$–67 ∘C	Using film temperature could improve the prediction of heat transfer coefficients.
Kruizenga et al. (2012)	CO_2–H_2O; E + N	-	$P = 7.5$–10.2 MPa $T_H = 31$–43 ∘C	A peak of heat transfer coefficient occurred at bulk temperature near the T_{pc}.
Figley et al. (2013)	Alloy 617; He-He in cc; N	$l_c = 0.247$ m; $n = 20$; $D_h = 1.22$ mm; $A = 0.0127$ m^2	$\dot{m} = 10$–80 kg/h $T_{H.in} = 1173$ K; $T_{C.in} = 813$ K $P_{out} = 3$ MPa	Heat load; Overall heat-transfer coefficient; Thermal effectiveness.
Mylavarapu et al. (2014)	Alloy 617; He-He in cc; E + N	$n = 120$; $D_h = 1.22$ mm; $A_H = 0.188$ m^2; $A_C = 0.168$ m^2	$\dot{m} = 10$–49 kg/h $T_{H.in} = 208$–790 °C; $T_{C.in} = 85$–390 °C $P_{in} = 1$–2.7 MPa	Pressure factor; Nusselt number; Cross-section and rough inlet profile resulted in a lower critical Reynolds.

Seo et al. (2015)	SUS304L; H_2O-H_2O in cc and p; E	D_h = 0.6685 mm; A_H = 26.037 mm^2; A_C = 34.716 mm^2	$Re_{.H}$ = 100–850 $Re_{.C}$ = 100–550 $T_{H.in}$ = 40–50 °C; $T_{C.in}$ = 20 °C	Pressure drop; Pressure factor; Heat-transfer rate; Overall heat-transfer coefficient.
Chen et al. (2016)	Alloy 617; He-He in cc; E + N	n = 120; D_h = 1.22 mm; A_H = 0.188 m^2; A_C = 0.168 m^2	$\dot{m}$ = 22–39 kg/h $T_{H.in}$ = 199–450 °C P_{in} = 1–2.7 MPa	Local temperature; Pressure factor; Nusselt number.
Aneesh et al. (2016)	Alloy 617; He-He in cc; E + N	l_c = 247.2 mm; p_c = 3.6 mm; d_c = 1 mm; D_h = 1.22 mm	$\dot{m}$ = 15–55 kg/h $T_{H.in}$ = 973–1173 °C; $T_{C.in}$ = 613–1013 °C P_{in} = 1–9 MPa	Local temperature and velocity profiles; Thermal–hydraulic performance.
Li et al. (2016)	CO_2; N	-	P = 7.5–8.5 MPa T = 5–95 ∘C	A PDF-based physically improved semiempirical correlation was developed.
Jeon et al. (2016)	SS 304; CO_2-LNG; N	Varied	T_H = 650 ∘C; T_C = 239 ∘C P_H = 0.1 MPa; P_C = 13.6 MPa	Channel cross-sectional shape would not obviously affect the thermal performance.
Chu et al. (2017)	SUS304L; CO_2-H_2O in c; E	l_c = 150 mm; p_c = 4 mm; w_c = 2.8 mm; d_c = 1.4 mm	$\dot{m}$ = 150–650 kg/h $T_{H.in}$ = 310–375 K $P_{H\cdot in}$ = 8–11 MPa	Pressure drop; Pressure factor; Heat-transfer rate; Nusselt number.
Kim et al. (2017)	SUS304L; LNG-CO_2 in c. p and cc; N	l_c = 0.05–1.2 m; p_c = 3 mm; d_c = 0.5–2.5 mm	$T_{H.in}$ = 500 °C; $T_{C.in}$ = 450 °C	Heat-transfer capacity; Heat-transfer effectiveness.
Lance et al. (2017)	H_2O; E	-	P = 0.1 MPa T_{in} = 40.6 ∘C	Flow mal-distribution due to the header was non-negligible.
Zhao et al. (2017)	s-N_2 in; N	l_c = 520 mm; w_c = 2 mm; h_c = 1.75 mm; d = 1.5 mm	$T_{C.in}$ = 113–130 K; P_C = 4.5–8 MPa	Overall heat transfer coefficient; Pressure drops; Efficiency; Average Nusselt number and Fanning friction factor;
Liu et al. (2018)	CO_2-CO_2; T + N	l = 500 mm; w = 2.4 mm; h = 3 mm; d = 2 mm	T_H = 127 ∘C; T_C = 27 ∘C P = 10 MPa; v = 4 m/s	Fin efficiency was improved with higher fin thermal conductivity and thicker fin.

Ren et al. (2019)	Alloy 617; CO_2–H_2O; N	l = 560 mm; w = 4 mm; h = 4.4 mm; d = 2.8 mm	P_H = 7.5–8.1 MPa T_H = 40–100 ◦C; T_C = 10–50 ◦C	Heat-transfer capacity; Overall heat-transfer coefficient.
Zhang et al. (2019)	SS 316L; CO_2– CO_2; N	l = 160 mm; D_h = 0.9776 mm	T_H = 87 ◦C; T_C = 27 ◦C P_H = 21 MPa; P_C = 8 MPa	Thinner thermal boundary layer results in local heat transfer improvement.
Zhang et al. (2019)	CO_2; N	l = 30 mm	P = 7.5–8.5 MPa	Buoyancy plays a leading role in deteriorated heat transfer but not the flow acceleration.
Chu et al. (2019)	sCO_2; N	n = 40; d = 2.12 mm; R = 6 mm; l = 20 mm.	T_{in} = 200 ◦C $Re_{in} = (2.85–28.9) \times 10^5$	Hyperbolic inlet header was found to reduce flow non-uniformity effectively.
Chai and Tassou (2019)	CO_2-CO_2; N	l = 272 mm; D_h = 2 mm	T = 100–450 ◦C P = 7.5–15 MPa	The local heat transfer decreased quickly near the inlet section due to the entrance effect.
Marchionni et al. (2019)	CO_2-CO_2; N	-	T_H = 253–350 ◦C; T_C = 41–87.5 ◦C P_H = 7.5–10.4 MPa; P_C = 12–20 MPa	Thermal expansion is non-negligible in the start-up process.
Ma et al. (2019)	CO_2-CO_2; N	l = 1000 mm; D_h = 2 mm	T_H = 227.7–267.7 ◦C; T_C = 88.7 ◦C P_H = 7.7 MPa; P_C = 35.86 MPa	The equilibration time was shortened with the increase of mass flow rate.
Cui et al. (2019)	CO_2-CO_2; T + N	-	T_H = 60–87 ◦C; T_C = 25–52 ◦C P_H = 8 MPa; P_C = 8–10 MPa	The uneven degree of HTC was presented by an overall distribution non-uniformity.

cc: counter-current flow; c: cross-flow; p: parallel-flow; E: experimental research; N: numerical simulation; T: theoretical analysis; SS: stainless steel; n: total number of channels.

Source: Adapted from Chai and Tassou (2020) and Liu et al. (2020).

Table 16 – Summary of heat transfer correlations for straight channel PCHEs.

Reference	**Fluid**	**Applicability range**	**Correlations**
Mylavarapu et al. (2014)	Helium	$2300 \leq Re \leq 5 \times 10^6$ $0.5 \leq Pr \leq 2000$	$Nu = \frac{(f/2)(Re-1000)Pr}{1+12.7(Pr^{2/3}-1)\sqrt{f/2}}$. $f = \frac{1}{4}\left(\frac{1}{1.82\ log\ Re-1.64}\right)^2$
		$2300 \leq Re \leq 3100$	$Nu = 3.5239\left(\frac{Re}{1000}\right)^4 - 45.148\left(\frac{Re}{1000}\right)^3 + 212.13\left(\frac{Re}{1000}\right)^2 - 427.45\left(\frac{Re}{1000}\right) + 316.08$
Seo et al. (2015)	Water	$100 < Re \leq 850$	$Nu = 0.7203Re^{0.1775}Pr^{1/3}(\mu/\mu_W)^{0.14}$. $f = 1.3383Re^{-0.5003}$
Meshram et al. (2016)	CO_2	$500K < T_{b.\ hot} < 630K$	$Nu = 0.0493Re^{0.77}Pr^{0.55}$. $f = 0.8386Re^{-0.5985} + 0.00295$
		$600K < T_{b.\ hot} < 730K$	$Nu = 0.0514Re^{0.76}Pr^{0.55}$. $f = 0.8385Re^{-0.5978} + 0.00331$
		$400K < T_{b.\ cold} < 500K$	$Nu = 0.0718Re^{0.71}Pr^{0.55}$. $f = 0.8657Re^{-0.5755} + 0.00405$
		$500K < T_{b.\ cold} < 600K$	$Nu = 0.0661Re^{0.743}Pr^{0.55}$. $f = 0.8796Re^{-0.5705} + 0.00353$
		Diameter variation:	
		$500K < T_{b.\ hot} < 630K$	$Nu = 0.0685Re^{0.705}(D_{ch}/2)^{-0.122}$. $f = 0.0648Re^{-0.254}(D_{ch}/2)^{-0.0411}$
		$400K < T_{b.\ cold} < 500K$	$Nu = 0.0117Re^{0.843}(D_{ch}/2)^{0.0405}$. $f = 0.0759Re^{-0.241}(D_{ch}/2)^{0.089}$
Chen et al. (2016)	Helium	$1200 \leq Re \leq 1850$	$Nu = (0.01352 \pm 0.0094)Re^{(0.80058 \pm 0.0921)}$
		$1850 < Re \leq 2900$	$Nu = (3.6361 \times 10^{-4} \pm 7.855 \times 10^{-5})Re^{(1.2804 \pm 0.0273)}$
		$1200 \leq Re \leq 1850$	$Nu = (0.047516 \pm 0.015662)Re^{(0.633151 \pm 0.044606)}$
		$1850 < Re \leq 2900$	$Nu = (3.680123 \times 10^{-4} \pm 1.184389 \times 10^{-4})Re^{(1.282182 \pm 0.042068)}$

Source: Adapted from Huang et al. (2019) and White et al. (2020).

APPENDIX – Preliminary Study of the Chaotic Channels

CHAOTIC CHANNELS

METHODOLOGY

This study aimed to enhance the thermal-hydraulic performance of compact heat exchangers by developing a three-dimensional geometry capable of inducing chaotic advection. Three-dimensional geometry can induce chaotic advection without the need to increase the heat exchanger area. For each geometry studied here, the thermal performance was characterized by evaluating the local and average Nusselt numbers. And the hydrodynamic performance was characterized by calculating the local and average Poiseuille numbers. The ratio between the average Poiseuille number and the average Nusselt number was used to compare the hydrodynamic and thermal performances. The lower this ratio, the better the relationship between heat transfer intensification and pressure drop reduction.

Computational Domain

The PCHE usually contains large quantities of hot and cold channels leading to a very high computational cost. Therefore, numerical investigation based on the minimum periodic domain composed of hot and cold branches was the common choice of most of the works carried out on the subject. However, in this study, only one cold branch channel of each 3D geometry will be studied as seen in Figure 41. For all geometries, the hydraulic diameter (Dh) is equal to 3 mm, and the total unfolded length (L), counting the three periods, is fixed at 83.72 mm. The V-shape channel (a) has a rectangular cross-section with an aspect ratio of 2 (4.50 mm × 2.25 mm), while the other channels have a circular cross-section. The chaotic circular channel (b) inclines 55° to the horizontal, as is the upper part of the inclined V-circular channel (d). The V-circular (c) and inclined V-circular (d) channels were developed from the V-shape channel, changing its cross-section from rectangular to circular.

The chaotic circular channel was developed by the Thermal Fluid Flow (T2F) team of the Federal University of Santa Catarina based on the Joinville campus to manufacture a prototype through 3-D additive manufacturing, known as selective laser melting (SLM). And the circular cross-section was aimed at reducing fouling along the channel, thus facilitating the cleaning.

Figure 41 – Chaotic channels studied.

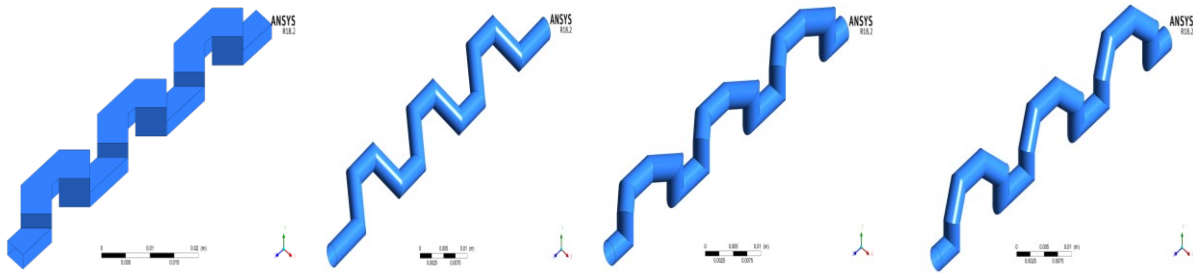

(a) (b) (c) (d)

Source: Author (2022).

For each geometry, the thermal performance was characterized by evaluating the local and average Nusselt number (Nu_m), and the hydrodynamic performance was characterized by calculating the local and average Poiseuille number (Po_m). The ratio between Nu_m and Po_m (Po_m/Nu_m) was used to compare the hydrodynamic and thermal performance. To perform the calculations planes were positioned as shown in Figure 42.

Figure 42 – Location of the planes to calculate Nu and f.

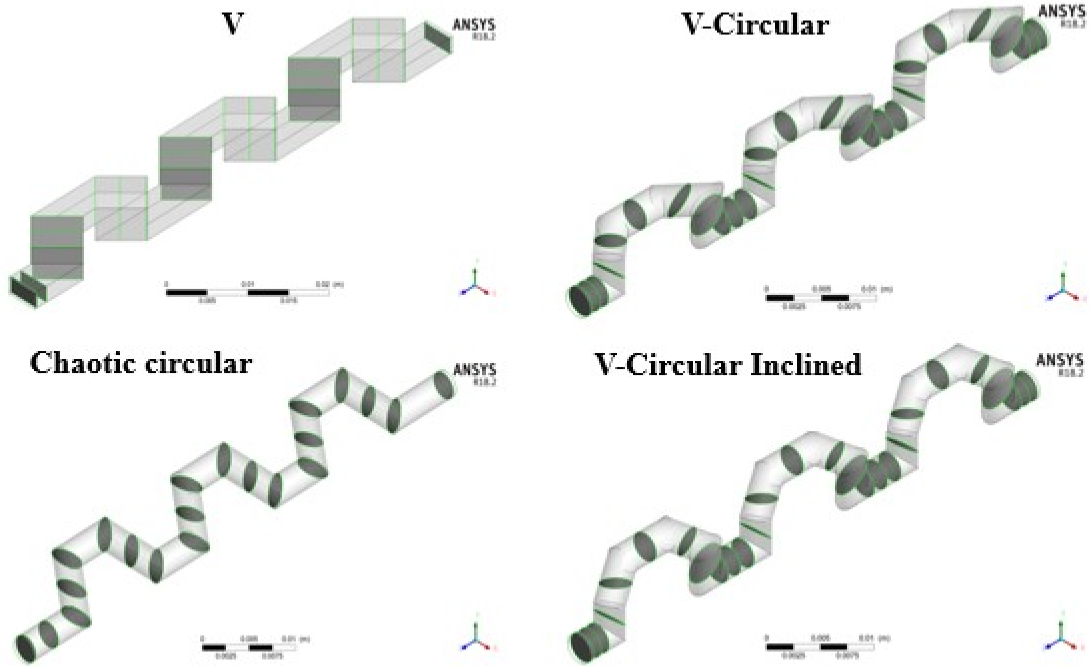

Source: Author (2022).

Boundary Conditions and Solver Settings

The problem under investigation was treated through numerical simulation, where the computational domain was created by ANSYS Meshing software with the development of the hexahedral mesh through the MultiZone method. After introducing the boundary conditions presented in Table 17, were performed the calculations by the commercial software ANSYS CFX 18.2 based on the finite volume method.

Table 17 – Geometric features and boundary conditions.

Geometric features	**Lasbet et al. 2007**	**Current study**
Hydraulic diameter	1.33 mm	3.00 mm
Unfolded length of channel	54.00 mm	83.72 mm
Height x Width - V channel with rectangular cross-section	2.00 mm x 1.00 mm	4.50 mm x 2.25 mm
Boundary conditions	**Lasbet et al. 2007**	**Current study**
Reynolds number analyzed	200	200
Work fluid	Water	Water
Inlet		
Velocity [m/s]	0.134	0.134 0.060
Temperature [K]	300	300
Outlet		
Static pressure [Pa]	0	0
Wall (no slipping and roughness)		
Heat Flux [W/m^2]	10,000	10,000

Source: Author (2022).

The Shear Stress Transport model (SST), based on the Navier-Stokes equations (RANS), was selected to investigate turbulence in 3D channels (Re = 1,000 and 10,000). The simulation was run until reaching convergence criteria below 10^{-8} or 3,000 iterations.

RESULTS

Mesh Independence and Model Validation

To have precision and consistency of the predicted results the new 3D channel configurations were simulated, with the conditions described in Lasbet et al. (2007) for an initial comparison of results. The other three channel configurations are not present in the cited article, and only the V configuration is analyzed. The mesh selected after the mesh independence test has about 2568050 elements. To validate the computational model, the numerical modeling of the V-shape channel presented in the study by Lasbet et al. (2007) was performed and showed an error of 2.42%. The results were also compared with the numerical simulation of Castelain et al. (2016), showing an error of 4.67%, which indicates the high prediction accuracy of the present simulation method and presents the results found in the validation process of the numerical model with Re = 200. The estimated Nu values for the V-shape channel are close to those indicated in the original article. The Nu_m value for the straight rectangular channel showed a slightly larger difference, as shown in Table 18.

Table 18 – Numerical model validation result.

Source	Nu_m	$Po_m = f.Re$	Po_m/Nu_m
V-shape Channel			
Lasbet *et al.*, (2007)	13.10	89.00	6.80
Castelain *et al.*, (2016)	14.03	88.40	6.30
Current study	12.62	84.84	6.72
Straight Rectangular Channel			
Lasbet *et al.*, (2007)	3.00	62.00	20.70
Castelain *et al.*, (2016)	3.03	62.00	20.46
Current study	3.78	63.44	16.78

Source: Author (2022).

Figure 43 shows the average Nusselt number (b) and average Poiseuille number (c) calculated from Equations (31) and (33), respectively, in the planes positioned along the channels.

Figure 43 – Average Nusselt number (a) and average Poiseuille number (b) along the channels.

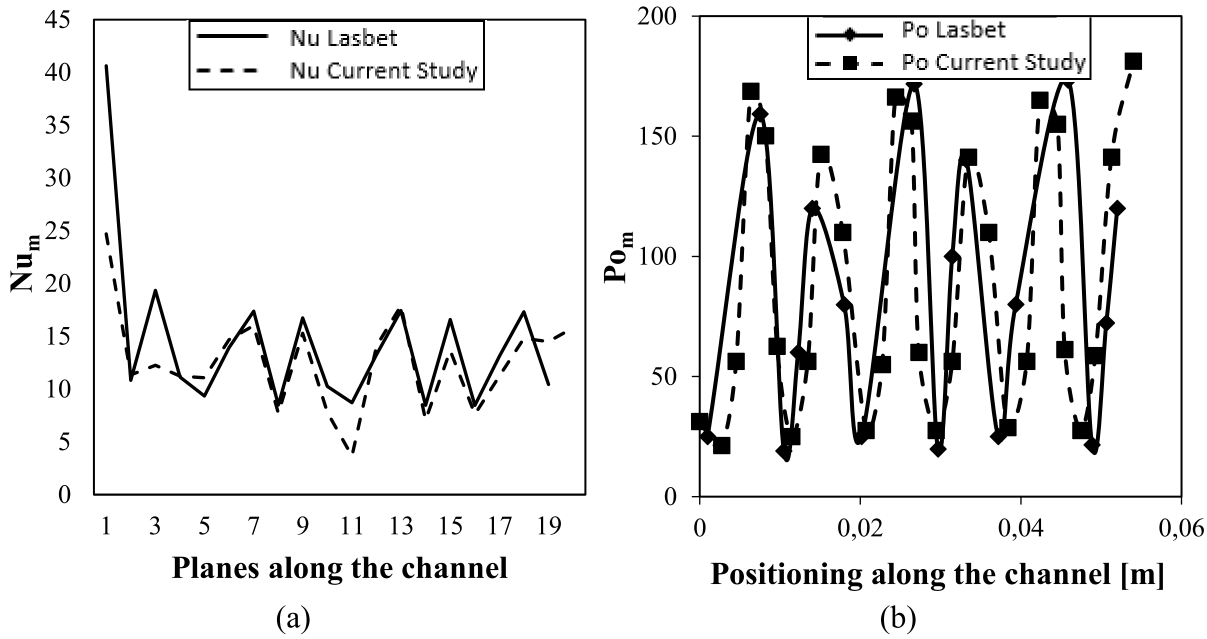

Source: Author (2022).

Channel Configuration Comparison

Table 19 shows the thermal-hydraulic behavior of the four 3D channel configurations. Due to the chaotic nature of their flows, all channels studied present Nu_m greater than the straight cylindrical channel (8.03), the current configuration of the analyzed exchanger.

Table 19 – Data on the thermo-hydraulic behavior of the studied channels.

Re	**200**			
Channel geometry	Nu_m	$Po_m = f.Re$	Po_m/Nu_m	ΔP **[Pa]**
V	15	145	9.6	37
Chaotic Circular	8	134	16.7	34
V-Circular	23	203	8.8	51
V-Circular Inclined	21	167	8.3	42

Source: Author (2022).

The V channel presents the second lowest Nu_m, the lowest pressure drop for the laminar and turbulent regime, and the highest pressure drops for the transition regime. The Circular Chaotic channel though showing the lowest Nu_m, behaves oppositely to the V channel concerning pressure drop, with the highest pressure drop for the laminar and fully turbulent regime and the lowest pressure drop for the transition regime. And for both channel configurations, the Po_m/Nu_m ratio decreases as the Reynolds number increases. V-Circular and V-Circular Inclined channels, on the other hand, exhibit a tiny difference in the decimal place for the Nu_m. But for the pressure drop, the V-Circular Inclined showed lower results. By comparison, Figure 44 demonstrates the Nu_m distribution in the four 3D channels, plus the straight rectangular and circular channels, for Reynolds of 200.

Figure 44 – Average *Nu* distribution for *Re* = 200 for the different channel configurations.

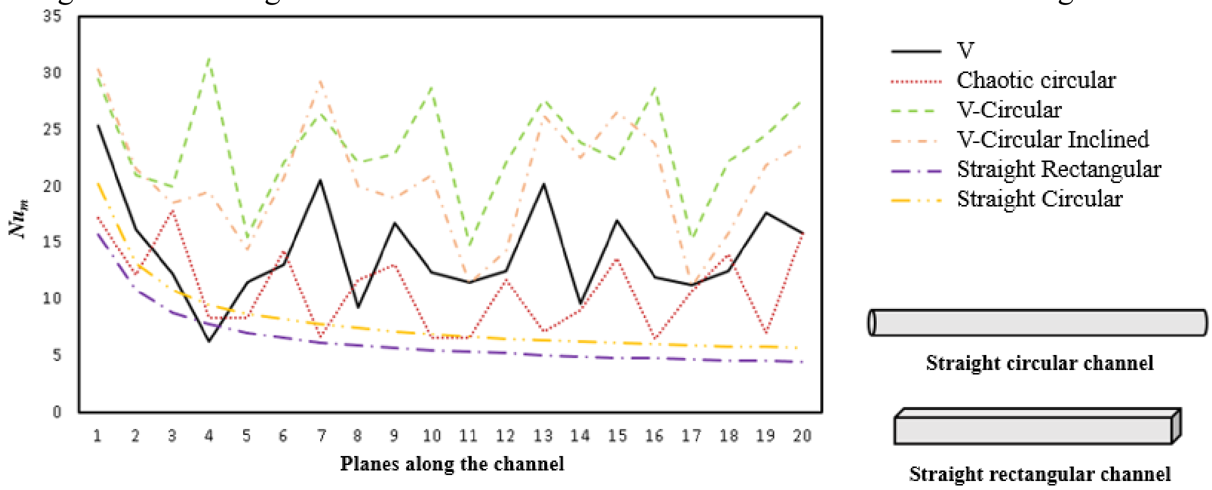

Source: Author (2022).

CONCLUSIONS

In this numerical investigation of chaotic channels, it became evident that the channels configurations identified as V-Circular and V-Circular Inclined present a good heat exchange and pressure drop ratio (Po_m/Nu_m) given by 8.8 and 8.3 respectively, with the V-Circular Inclined channel presenting the best result of the study. These values are comparable to the range of values found for the V channel indicated by literature data. However, the manufacturing process can be complex, potentially clogging the channel. The Circular Chaotic channel exhibited lower results than the V channel but higher than straight channels. By having slopes with more open angles, the Circular Chaotic channel becomes easier to fabricate and may be a viable option in the future. Further testing is required to verify these hypotheses through sample fabrication.

APPENDIX C – Numerical Results

Table 20 – Experimental data used in the numerical study.

Test	Re_h	Re_c	$T_{h,in}$ [°C]	$T_{h,out}$ [°C]	$T_{c,in}$ [°C]	$T_{c,out}$ [°C]	$\dot{m}_h$ [Kg/s]	$\dot{m}_c$ [Kg/s]	q_h [W]	q_c [W]	$P_{h,in}$ [Pa]	ΔP_h [Pa]	$P_{c,in}$ [Pa]	ΔP_c [Pa]
T40C1	1570	1745	40.2498	40.1348	22.6440	31.6051	0.2511	0.0088	120.76	79.15	108256.30	2030.10	100298.20	624.70
T40C3	1580	3327	40.0802	39.9163	22.3963	31.6854	0.2535	0.0168	173.81	156.45	108491.30	2059.90	102619.80	2331.00
T40C5	1587	5457	40.2221	39.9767	22.4369	31.5493	0.2542	0.0275	260.86	251.71	108412.40	2028.20	108561.30	6786.60
T40C7	1598	7918	40.2350	39.9287	23.4635	31.5060	0.2561	0.0400	328.00	322.81	108593.90	2058.30	119154.00	14649.30
T40C9	1576	9944	40.2411	39.9150	25.6268	31.9579	0.2526	0.0504	344.54	320.27	108418.70	2032.10	130589.00	22888.70
T50C1	1933	1670	50.1113	49.9642	24.5815	39.0274	0.2597	0.0085	159.64	123.70	108671.30	2214.30	100288.60	599.50
T50C3	1901	3053	50.1265	49.9113	24.1734	37.7602	0.2554	0.0155	229.86	212.18	108367.30	2159.00	102170.30	2001.30
T50C5	1876	5367	50.1576	49.8137	24.2239	37.6382	0.2522	0.0273	362.63	368.21	108162.10	2115.40	108514.10	6765.60
T50C7	1874	7716	50.1698	49.7322	26.2854	37.9560	0.2521	0.0394	461.34	462.10	108195.20	2125.60	118903.30	14441.10
T50C9	1850	9882	50.1843	49.6974	28.9118	38.4828	0.2489	0.0507	506.76	487.40	108050.70	2085.20	131415.70	23438.90
T60C1	2332	1685	60.1074	59.9061	23.3110	43.8928	0.2673	0.0086	225.06	178.62	108798.60	2155.80	100393.20	646.00
T60C3	2305	3039	60.1792	59.8866	23.2017	42.5230	0.2641	0.0155	323.09	301.81	108452.60	2094.50	102260.30	2032.20
T60C5	2324	5310	60.2183	59.7559	23.7738	42.7276	0.2665	0.0272	515.40	517.90	108689.60	2134.60	108533.90	6732.30
T60C7	2321	7420	60.2987	59.7137	26.2696	43.1721	0.2660	0.0381	650.90	647.96	108673.80	2111.80	117720.60	13530.80
T60C9	2288	9881	60.3067	59.6180	29.2578	43.6289	0.2625	0.0510	755.97	737.01	108374.70	2061.20	132213.90	23937.00
T70C1	2760	1724	70.0306	69.7885	23.3659	49.1124	0.2743	0.0089	278.07	230.14	108503.20	2078.20	100431.60	700.30
T70C3	2746	3170	70.0510	69.6695	22.5513	47.4537	0.2731	0.0163	436.18	408.07	108345.50	2056.40	102572.60	2278.00
T70C5	2739	4887	70.0803	69.5110	23.2103	47.6748	0.2726	0.0252	649.81	618.89	108314.50	2056.70	107209.00	5742.60
T70C7	2753	7543	70.1248	69.3524	25.6742	47.8697	0.2743	0.0390	886.95	869.60	108475.10	2085.90	118775.10	14282.30

T70C9	2755	9879	70.1734	69.2730	28.8979	48.2908	0.2745	0.0513	1034.78	999.85	108501.60	2097.50	132775.10	24269.00
T80C1	3145	1736	79.9821	79.7037	24.1286	55.0613	0.2744	0.0090	320.47	280.93	108762.60	2082.30	100486.90	744.80
T80C3	3138	3175	80.0153	79.5689	22.4181	52.5182	0.2740	0.0164	512.93	497.14	108741.60	2095.50	102680.40	2355.90
T80C5	3101	5413	80.0544	79.3339	23.1394	52.5304	0.2711	0.0280	819.18	828.48	108504.80	2074.10	109315.60	7297.10
T80C7	3077	7755	80.0370	79.0822	25.0422	52.3230	0.2694	0.0402	1079.02	1104.28	108399.20	2060.40	120132.90	15244.10
T80C9	3046	9584	79.8282	78.7276	27.6328	52.3892	0.2677	0.0499	1235.44	1242.71	108208.20	2038.70	131361.50	23247.60

Source: Adapted from Silva et al. (2021).

Table 21 – Circular channel mesh characteristics.

Mesh	Element	Time [h]	Test	Heat transfer rate [W]		Pressure drop [Pa]		Near wall y^+	
				Hot	Cold	Hot	Cold	Hot	Cold
1	570720 (core) 2916 (core corners) 758052 (hot branch) 774192 (cold branch)	06:30	T60C1	213.9340	213.9300	1337.0872	666.4732	1.959 – 4.539	2.352 – 4.645
			T60C5	499.4220	499.4210	1330.3472	5582.1875	1.955 – 4.530	5.673 – 9.521
			T60C9	602.5980	602.6000	1296.8870	17532.1296	1.933 – 4.485	9.841 – 15.741
2	1206380 (core) 2916 (core corners) 1990036 (hot branch) 2117732 (cold branch)	08:00	T60C1	232.7580	232.7580	1423.3754	721.6535	0.952 – 5.374	1.542 – 5.718
			T60C5	572.6290	572.6300	1416.1853	5653.2013	0.954 – 5.364	2.815 – 11.927
			T60C9	718.4960	718.4890	1373.0210	16902.5696	0.983 – 5.374	3.718 – 19.139
3	2455556 (core) 2916 (core corners) 1990036 (hot branch) 2117732 (cold branch)	15:00	T60C1	232.3980	232.3990	1423.3754	717.9209	0.952 – 5.374	1.553 – 5.707
			T60C5	571.6050	571.6040	1416.1853	5614.9636	0.954 – 5.364	2.838 – 11.895
			T60C9	716.9410	716.9420	1380.4449	17040.4073	0.960 – 5.315	4.450 – 18.122
4	1206380 (core) 2916 (core corners) 3930783 (hot branch) 4245212 (cold branch)	27:00 or 04:30 (cluster)	T60C1	221.3200	221.3080	1387.3371	691.0664	0.105 – 2.283	0.223 – 2.711
			T60C5	521.6720	521.6820	1380.6370	5121.8377	0.106 – 2.280	0.269 – 5.393
			T60C9	713.7850	713.7800	1347.3566	17146.2522	0.164 – 2.283	0.352 – 8.334
5	1206380 (core) 2916 (core corners) 5540043 (hot branch) 5982092 (cold branch)	37:30	T60C1	221.6290	221.6160	1386.3515	692.1138	0.178 – 2.325	0.175 – 2.412
			T60C5	521.7380	521.7540	1379.6715	5116.1381	0.179 – 2.321	0.250 – 4.851
			T60C9	713.8400	713.8190	1346.4615	17109.9102	0.182 – 2.302	0.156 – 7.399

Source: Author (2022).

Table 22 – Semicircular channel mesh characteristics.

Mesh	Element	Time [h]	Test	Heat transfer rate [W]		Pressure drop [Pa]		Near wall y^+	
				Hot	Cold	Hot	Cold	Hot	Cold
1	518616 (core) 2916 (core corners) 595728 (hot branch) 705936 (cold branch)	05:30	T60C1	206.2270	206.2240	1193.0872	541.5377	2.808 – 28.630	1.246 – 36.750
			T60C5	491.6990	491.6990	1187.0172	4352.7978	2.801 – 28.559	2.598 – 101.324
			T60C9	628.9100	628.9090	1156.8973	13928.4084	2.769 – 28.207	4.221 – 178.527
2	989996 (core) 2916 (core corners) 2146466 (hot branch) 2301810 (cold branch)	10:00	T60C1	212.4610	211.8720	1226.4308	560.6220	0.381 – 23.161	0.584 – 27.026
			T60C5	497.9650	498.0430	1220.6709	4498.4050	0.397 – 23.166	0.678 – 75.821
			T60C9	635.0270	634.3030	1189.6808	14298.1902	0.427 – 22.835	1.607 – 134.203
3	4440576 (core) 2916 (core corners) 2146466 (hot branch) 2301810 (cold branch)	10:30 or 03:40 (cluster)	T60C1	211.2190	211.5410	1226.3607	560.5590	0.387 – 23.181	0.584 – 27.026
			T60C5	495.7300	496.5900	1220.4210	4497.7550	0.679 – 23.064	0.603 – 75.615
			T60C9	635.3240	634.3320	1189.4906	14298.1902	0.685 – 22.815	1.314 – 133.902
4	989996 (core) 2916 (core corners) 3126326 (hot branch) 3444980 (cold branch)	12:30 or 03:00 (cluster)	T60C1	212.6370	212.1800	1224.0806	559.1890	0.243 – 23.446	0.534 – 26.921
			T60C5	498.2500	498.2640	1217.8609	4477.4453	0.265 – 23.418	1.112 – 75.531
			T60C9	633.4100	634.2880	1189.7711	14298.1902	0.685 – 22.786	1.314 – 133.902
5	989996 (core) 2916 (core corners) 3575278 (hot branch) 3877118 (cold branch)	03:30 (cluster)	T60C1	212.2340	211.8680	1226.3808	560.6230	0.676 – 23.127	0.393 – 26.945
			T60C5	497.7890	498.0780	1220.1808	4498.4050	0.679 – 23.083	0.602 – 75.615
			T60C9	635.1640	634.3410	1189.4606	14298.1902	0.685 – 22.828	1.315 – 133.902
6	989996 (core) 2916 (core corners) 3970549 (hot branch) 4317886 (cold branch)	05:00 (cluster)	T60C1	214.1800	213.0790	1268.9512	576.8014	0.165 – 17.754	0.220 – 19.805
			T60C5	497.7970	498.0640	1220.4210	4498.4050	0.679 –23.055	0.603 – 75.615
			T60C9	635.0310	634.3330	1189.4105	14298.1902	0.686 – 22.804	1.314 – 133.902

Source: Author (2022).

Table 23 – Single channels mesh characteristics.

Mesh	Element	Time [h]	Test	Nu Hot	Nu Cold	Pressure drop [Pa] Hot	Pressure drop [Pa] Cold	Near wall y^+ Hot	Near wall y^+ Cold
C-1	2703417	02:40	T60C1	13.2070	5.0860	1249.1322	853.5457	0.139 – 1.648	0.055 – 2.020
			T60C5	13.1500	13.5910	1249.1322	4207.9222	0.139 – 1.648	0.229 – 3.866
			T60C9	12.9380	25.9330	1211.8121	13635.1798	0.157 – 1.628	0.307 – 6.224
C-2	4132447	04:05	T60C1	13.1660	5.0970	1248.3720	853.0279	0.148 – 1.547	0.072 – 1.900
			T60C5	13.1120	13.5930	1248.3820	4230.9212	0.148 – 1.547	0.258 – 3.702
			T60C9	12.8980	25.8660	1211.0919	13580.6704	0.165 – 1.527	0.566 – 5.998
CD-1	2703417	02:17	T60C1	13.2750	5.1190	1358.2820	941.9141	0.044 – 2.122	0.082 – 2.400
			T60C5	13.2750	13.7410	1358.2820	4669.2994	0.044 – 2.122	0.242 – 4.962
			T60C9	13.0050	26.4910	1317.8819	15175.8560	0.066 – 2.096	0.452 – 7.757
CD-2	4567572	04:00	T60C1	13.2390	5.1170	1358.4119	942.0300	0.028 – 2.687	0.060 – 2.158
			T60C5	13.2250	13.7710	1356.1819	4619.7812	0.025 – 2.800	0.138 – 3.963
			T60C9	12.9720	26.4700	1318.0818	15260.0587	0.049 – 2.808	0.132 – 6.345
VI-1	3992392 (cold branch) 3532146 (hot branch)	03:30	T60C1	25.7340	8.5610	4804.6758	4600.1082	0.043 – 3.447	0.038 – 4.577
			T60C5	25.7340	22.9560	4804.6758	25138.2707	0.043 – 3.447	0.168 – 9.986
			T60C9	25.3200	46.6070	4646.2056	73836.3757	0.052 – 3.402	0.404 – 15.932
VI-2	4434760 (cold branch) 4852975 (hot branch)	04:30 or 01:10 (cluster)	T60C1	24.8970	8.3920	4853.4060	4562.4584	0.018 – 2.669	0.026 – 2.982
			T60C5	25.0210	21.6250	4966.2858	25268.7669	0.026 – 2.786	0.086 – 6.361
			T60C9	24.5390	42.7750	4732.7556	74159.7742	0.033 – 2.653	0.241 – 10.080

1: initial refine, 2: more refined, C: circular, CD: circular deformed, and VI: chaotic circular V-shaped.

Source: Author (2022).

Table 24 – The numerical result of the complete core with circular channels.

Test	$T_{h,in}$ [°C]	$T_{h,out}$ [°C]	$T_{c,in}$ [°C]	$T_{c,out}$ [°C]	$\dot{m}_h$ [Kg/s]	$\dot{m}_c$ [Kg/s]	q_h [W]	q_c [W]	$P_{h,in}$ [Pa]	ΔP_h [Pa]	$P_{c,in}$ [Pa]	ΔP_c [Pa]
T40C1	40.2500	40.1450	22.6440	34.8720	0.12557	0.00440	108.0830	108.0850	1255.1800	1255.1953	687.5560	687.5734
T40C3	40.0080	39.9090	22.3960	32.9430	0.12675	0.00839	178.1540	178.1470	1274.1500	1274.1655	2087.4300	2087.4774
T40C5	40.2220	39.9760	22.4370	31.6320	0.12708	0.01376	256.7290	256.7190	1279.4700	1279.4856	5091.2900	5091.3864
T40C7	40.2350	39.9330	23.4630	31.1030	0.12804	0.01999	317.9660	317.9580	1295.0300	1295.0458	10332.0000	10332.1647
T40C9	40.2410	39.9270	25.6260	31.5130	0.12631	0.02519	326.7610	326.7590	1267.0600	1267.0755	16298.2000	16298.4379
T50C1	50.1110	49.9680	24.5810	42.4000	0.12985	0.00426	152.4790	152.4750	1324.5900	1324.6063	665.0660	665.0832
T50C3	50.1270	49.8910	24.1730	39.9380	0.12771	0.00777	246.4550	246.4440	1289.6700	1289.6858	1857.8300	1857.8737
T50C5	50.1580	49.7980	24.2240	37.6810	0.12611	0.01366	372.2300	372.2200	1263.8400	1263.8554	5104.1900	5104.2873
T50C7	50.1700	49.7360	26.2850	37.3360	0.12607	0.01970	449.1930	449.1810	1263.2000	1263.2154	10211.4000	10211.5645
T50C9	50.1840	49.7140	28.9110	37.7420	0.12446	0.02534	482.0980	482.0970	1237.4600	1237.4750	16766.0000	16766.2452
T60C1	60.1070	59.9050	23.3110	48.8170	0.13363	0.00432	221.3200	221.3080	1387.3200	1387.3371	691.0480	691.0664
T60C3	60.1790	59.8550	23.2020	45.6030	0.13204	0.00777	350.1210	350.1090	1360.7700	1360.7868	1882.5900	1882.6347
T60C5	60.2180	59.7410	23.7730	42.7420	0.13323	0.01360	521.6720	521.6820	1380.6200	1380.6370	5121.7400	5121.8377
T60C7	60.2990	59.7250	26.2690	42.3200	0.13302	0.01907	626.8050	626.7830	1377.1000	1377.1170	9693.1700	9693.3296
T60C9	60.3070	59.6460	29.2570	42.4730	0.13123	0.02550	713.7850	713.7800	1347.3400	1347.3566	17146.0000	17146.2522
T70C1	70.0310	69.7750	23.3660	55.3940	0.13716	0.00445	286.2810	286.2660	1447.0900	1447.1080	737.7810	737.8010
T70C3	70.0510	69.6350	22.5510	50.9000	0.13655	0.00815	464.7730	464.7720	1436.6800	1436.6978	2073.5200	2073.5684
T70C5	70.0800	69.5150	23.2100	48.0870	0.13632	0.01258	631.6950	631.7110	1432.7600	1432.7778	4490.3500	4490.4387
T70C7	70.1250	69.3870	25.6740	46.5550	0.13714	0.01948	831.6210	831.5940	1446.7500	1446.7680	10186.7000	10186.8678
T70C9	70.1730	69.3270	28.8970	46.6690	0.13724	0.02563	955.8870	955.8790	1448.4600	1448.4780	17458.8000	17459.0591
T80C1	79.9820	79.6740	24.1280	62.2090	0.13722	0.00451	344.9570	344.9420	1448.1200	1448.1380	767.2620	767.2830
T80C3	80.0150	79.5120	22.4180	56.5890	0.13698	0.00821	564.3240	564.3340	1444.0200	1444.0379	2129.1800	2129.2294
T80C5	80.0540	79.3110	23.1390	52.3380	0.13554	0.01401	826.7700	826.7750	1419.5200	1419.5376	5530.0100	5530.1145
T80C7	80.0370	79.0890	25.0420	50.5550	0.13472	0.02012	1049.2100	1049.1700	1405.6500	1405.6674	10930.1000	10930.2795
T80C9	79.8280	78.7580	27.6320	50.3340	0.13384	0.02495	1177.7000	1177.6900	1390.8400	1390.8572	16662.4000	16662.6520

Source: Author (2022).

Table 25 – The numerical result of the complete core with semicircular channels.

Test	$T_{h,in}$ [°C]	$T_{h,out}$ [°C]	$T_{c,in}$ [°C]	$T_{c,out}$ [°C]	$\dot{m}_h$ [Kg/s]	$\dot{m}_c$ [Kg/s]	q_h [W]	q_c [W]	$P_{h,in}$ [Pa]	ΔP_h [Pa]	$P_{c,in}$ [Pa]	ΔP_c [Pa]
T40C1	40.2500	40.1500	22.6440	34.3230	0.12557	0.00440	103.1940	103.2930	1104.6500	1104.6507	558.9710	558.9729
T40C3	40.0800	39.9200	22.3960	32.3440	0.12675	0.00839	168.1500	168.1400	1122.1600	1122.1609	1771.3100	1771.3140
T40C5	40.2220	39.9880	22.4370	31.2460	0.12708	0.01376	246.6880	246.0740	1127.1400	1127.1406	4472.5000	4472.5047
T40C7	40.2350	39.9530	23.4630	30.6320	0.12804	0.01999	298.2680	298.1920	1141.2900	1141.2907	8909.2800	8909.2802
T40C9	40.2410	39.9560	25.6270	31.0070	0.12631	0.02519	298.4180	297.9610	1115.5100	1115.5107	13587.6000	13587.5907
T50C1	50.1110	49.9760	24.5820	41.6220	0.12985	0.00426	145.7090	145.8950	1168.5600	1168.5610	539.2260	539.2279
T50C3	50.1270	49.9060	24.1730	39.0310	0.12771	0.00777	232.1370	232.3990	1136.3000	1136.3007	1566.4900	1566.4938
T50C5	50.1580	49.8160	24.2240	37.0790	0.12611	0.01366	355.7640	355.7930	1112.5700	1112.5707	4483.2700	4483.2748
T50C7	50.1700	49.7670	26.2850	36.6070	0.12607	0.01970	419.4940	419.5470	1112.2900	1112.2907	8829.1600	8829.1607
T50C9	50.1840	49.7640	28.9120	36.8450	0.12446	0.02534	433.6720	432.8670	1088.4400	1088.4407	13977.7000	13977.6904
T60C1	60.1070	59.9150	23.3110	47.7150	0.13363	0.00432	212.4610	211.8720	1226.4300	1226.4308	560.6200	560.6220
T60C3	60.1790	59.8760	23.2020	44.3180	0.13204	0.00777	330.2810	330.2370	1202.1000	1202.1006	1586.4100	1586.4139
T60C5	60.2180	59.7670	23.7740	41.8720	0.13323	0.01360	497.9650	498.0430	1220.6700	1220.6709	4498.4000	4498.4050
T60C7	60.2990	59.7660	26.2700	41.2890	0.13302	0.01907	585.6520	586.6690	1216.7900	1216.7909	8423.0200	8423.0216
T60C9	60.3070	59.7230	29.2580	41.0000	0.13123	0.02550	635.0270	634.3030	1189.6800	1189.6808	14298.2000	14298.1902
T70C1	70.0310	69.7880	23.3660	54.0110	0.13716	0.00445	274.9020	274.0760	1282.1000	1282.1007	599.6370	599.6391
T70C3	70.0510	69.6620	22.5510	49.2810	0.13655	0.00815	439.5430	438.5000	1272.4400	1272.4407	1752.2300	1752.2342
T70C5	70.0800	69.5460	23.2100	46.9130	0.13632	0.01258	603.4770	602.2990	1268.8100	1268.8107	3930.4300	3930.4352
T70C7	70.1250	69.4410	25.6740	45.1490	0.13714	0.01948	777.0660	775.8260	1281.7800	1281.7807	8841.7400	8841.7411
T70C9	70.1730	69.4290	28.8980	44.6180	0.13724	0.02563	847.1450	845.8920	1283.3700	1283.3707	14566.2000	14566.1902
T80C1	79.9820	79.6900	24.1290	60.5790	0.13722	0.00451	331.3830	330.3860	1283.0500	1283.0507	624.0740	624.0762
T80C3	80.0150	79.5440	22.4180	54.6540	0.13698	0.00821	533.9690	532.7130	1279.2500	1279.2507	1799.3700	1799.3743
T80C5	80.0540	79.3500	23.1390	51.0110	0.13554	0.01401	791.1840	789.6910	1256.5400	1256.5407	4862.3800	4862.3851
T80C7	80.0370	79.1630	25.0420	48.7360	0.13472	0.02012	976.3200	974.7040	1243.7000	1243.7007	9462.6900	9462.6904
T80C9	79.8280	78.8820	27.6330	47.8240	0.13384	0.02495	1049.5300	1047.8600	1229.9900	1229.9907	13979.3000	13979.2918

Source: Author (2022).

Table 26 – Pressure drop by plane of the hot branch for complete core with circular channels.

Test	**Circular - Hot branch**												
	$P_{h,in}$ **[Pa]**	$P_{h,P1}$ **[Pa]**	$P_{h,P2}$ **[Pa]**	$P_{h,P3}$ **[Pa]**	$P_{h,P4}$ **[Pa]**	$P_{h,out}$ **[Pa]**	ΔP_h **[Pa]**	**in - P1**	**P1 - P2**	**P2 - P3**	**P3 - P4**	**P4 - out**	ΔP_h **[Pa]**
T40C1	1255.1800	1250.1200	1017.1100	-25.5230	5.6260	-0.0153	1255.1953	5.0600	233.0100	1042.6330	-31.1490	5.6413	1255.1953
T40C3	1274.1500	1269.0200	1031.6900	-25.9340	5.7060	-0.0155	1274.1655	5.1300	237.3300	1057.6240	-31.6400	5.7215	1274.1655
T40C5	1279.4700	1274.3300	1035.7900	-26.0500	5.7290	-0.0156	1279.4856	5.1400	238.5400	1061.8400	-31.7790	5.7446	1279.4856
T40C7	1295.0300	1289.8300	1047.7400	-26.3870	5.7950	-0.0158	1295.0458	5.2000	242.0900	1074.1270	-32.1820	5.8108	1295.0458
T40C9	1267.0600	1261.9600	1026.2500	-25.7810	5.6760	-0.0155	1267.0755	5.1000	235.7100	1052.0310	-31.4570	5.6915	1267.0755
T50C1	1324.5900	1319.2800	1070.4400	-27.0270	5.9200	-0.0163	1324.6063	5.3100	248.8400	1097.4670	-32.9470	5.9363	1324.6063
T50C3	1289.6700	1284.4900	1043.6300	-26.2710	5.7720	-0.0158	1289.6858	5.1800	240.8600	1069.9010	-32.0430	5.7878	1289.6858
T50C5	1263.8400	1258.7500	1023.7700	-25.7110	5.6630	-0.0154	1263.8554	5.0900	234.9800	1049.4810	-31.3740	5.6784	1263.8554
T50C7	1263.2000	1258.1100	1023.2800	-25.6970	5.6600	-0.0154	1263.2154	5.0900	234.8300	1048.9770	-31.3570	5.6754	1263.2154
T50C9	1237.4600	1232.4600	1003.4800	-25.1380	5.5500	-0.0150	1237.4750	5.0000	228.9800	1028.6180	-30.6880	5.5650	1237.4750
T60C1	1387.3200	1381.7900	1118.5400	-28.3840	6.1850	-0.0171	1387.3371	5.5300	263.2500	1146.9240	-34.5690	6.2021	1387.3371
T60C3	1360.7700	1355.3400	1098.1900	-27.8100	6.0730	-0.0168	1360.7868	5.4300	257.1500	1126.0000	-33.8830	6.0898	1360.7868
T60C5	1380.6200	1375.1100	1113.4000	-28.2390	6.1570	-0.0170	1380.6370	5.5100	261.7100	1141.6390	-34.3960	6.1740	1380.6370
T60C7	1377.1000	1371.6100	1110.7100	-28.1630	6.1420	-0.0170	1377.1170	5.4900	260.9000	1138.8730	-34.3050	6.1590	1377.1170
T60C9	1347.3400	1341.9500	1087.8900	-27.5200	6.0160	-0.0166	1347.3566	5.3900	254.0600	1115.4100	-33.5360	6.0326	1347.3566
T70C1	1447.0900	1441.3600	1164.2800	-29.6740	6.4360	-0.0180	1447.1080	5.7300	277.0800	1193.9540	-36.1100	6.4540	1447.1080
T70C3	1436.6800	1430.9800	1156.3200	-29.4500	6.3930	-0.0178	1436.6978	5.7000	274.6600	1185.7700	-35.8430	6.4108	1436.6978
T70C5	1432.7600	1427.0800	1153.3200	-29.3650	6.3760	-0.0178	1432.7778	5.6800	273.7600	1182.6850	-35.7410	6.3938	1432.7778
T70C7	1446.7500	1441.0200	1164.0200	-29.6670	6.4350	-0.0180	1446.7680	5.7300	277.0000	1193.6870	-36.1020	6.4530	1446.7680
T70C9	1448.4600	1442.7200	1165.3300	-29.7040	6.4420	-0.0180	1448.4780	5.7400	277.3900	1195.0340	-36.1460	6.4600	1448.4780
T80C1	1448.1200	1442.3800	1165.0600	-29.6960	6.4410	-0.0180	1448.1380	5.7400	277.3200	1194.7560	-36.1370	6.4590	1448.1380
T80C3	1444.0200	1438.2900	1161.9300	-29.6080	6.4230	-0.0179	1444.0379	5.7300	276.3600	1191.5380	-36.0310	6.4409	1444.0379
T80C5	1419.5200	1413.8800	1143.1900	-29.0790	6.3200	-0.0176	1419.5376	5.6400	270.6900	1172.2690	-35.3990	6.3376	1419.5376
T80C7	1405.6500	1400.0600	1132.5700	-28.7800	6.2620	-0.0174	1405.6674	5.5900	267.4900	1161.3500	-35.0420	6.2794	1405.6674
T80C9	1390.8400	1385.3000	1121.2300	-28.4600	6.2000	-0.0172	1390.8572	5.5400	264.0700	1149.6900	-34.6600	6.2172	1390.8572

Source: Author (2022).

Table 27 – Pressure drop by plane of the cold branch for complete core with circular channels.

Test	Circular - Cold branch												
	$P_{c,in}$ [Pa]	$P_{c,P5}$ [Pa]	$P_{c,P6}$ [Pa]	$P_{c,P7}$ [Pa]	$P_{c,P8}$ [Pa]	$P_{c,out}$ [Pa]	ΔP_c [Pa]	in - P5	P5 - P6	P6 - P7	P7 - P8	P8 - out	ΔP_c [Pa]
T40C1	687.5560	683.5910	544.0480	4.8570	3.8490	-0.0174	687.5734	3.9650	139.5430	539.1910	1.0080	3.8664	687.5734
T40C3	2087.4300	2076.5300	1583.7700	27.5270	9.7540	-0.0474	2087.4774	10.900	492.7600	1556.2430	17.7730	9.8014	2087.4774
T40C5	5091.2900	5066.4500	3777.2000	90.1530	20.6770	-0.0964	5091.3864	24.840	1289.250	3687.0470	69.4760	20.773	5091.3864
T40C7	10332.000	10286.100	7657.4000	215.285	36.8640	-0.1647	10332.165	45.900	2628.700	7442.1150	178.421	37.029	10332.165
T40C9	16298.200	16232.100	12200.700	368.332	52.9630	-0.2379	16298.438	66.100	4031.400	11832.368	315.369	53.201	16298.438
T50C1	665.0660	661.2680	529.3330	4.5150	3.7520	-0.0172	665.0832	3.7980	131.9350	524.8180	0.7630	3.7692	665.0832
T50C3	1857.8300	1848.1600	1421.4900	23.3110	8.8840	-0.0437	1857.8737	9.6700	426.6700	1398.1790	14.4270	8.9277	1857.8737
T50C5	5104.1900	5079.5200	3801.2400	90.5020	20.8230	-0.0973	5104.2873	24.670	1278.280	3710.7380	69.6790	20.920	5104.2873
T50C7	10211.400	10166.200	7586.7500	212.742	36.6820	-0.1645	10211.565	45.200	2579.450	7374.0080	176.060	36.847	10211.565
T50C9	16766.000	16698.700	12588.200	382.117	54.5810	-0.2452	16766.245	67.300	4110.500	12206.083	327.536	54.826	16766.245
T60C1	691.0480	687.1850	552.0480	4.8530	3.8970	-0.0184	691.0664	3.8630	135.1370	547.1950	0.9560	3.9154	691.0664
T60C3	1882.5900	1872.9500	1447.5600	23.7610	9.0500	-0.0447	1882.6347	9.6400	425.3900	1423.7990	14.7110	9.0947	1882.6347
T60C5	5121.7400	5097.3000	3832.3200	91.1500	20.9870	-0.0977	5121.8377	24.440	1264.980	3741.1700	70.1630	21.085	5121.8377
T60C7	9693.1700	9650.2900	7224.7300	200.594	35.2420	-0.1596	9693.3296	42.880	2425.560	7024.1360	165.352	35.402	9693.3296
T60C9	17146.000	17078.100	12923.300	394.545	55.9400	-0.2522	17146.252	67.900	4154.800	12528.755	338.605	56.192	17146.252
T70C1	737.7810	733.7400	590.4120	5.4660	4.1490	-0.0200	737.8010	4.0410	143.3280	584.9460	1.3170	4.1690	737.8010
T70C3	2073.5200	2063.1300	1597.0800	27.1940	9.8940	-0.0484	2073.5684	10.390	466.0500	1569.8860	17.3000	9.9424	2073.5684
T70C5	4490.3500	4468.9400	3382.9000	77.1210	18.8340	-0.0887	4490.4387	21.410	1086.040	3305.7790	58.2870	18.923	4490.4387
T70C7	10186.700	10142.400	7625.8300	213.597	36.7590	-0.1678	10186.868	44.300	2516.570	7412.2330	176.838	36.927	10186.868
T70C9	17458.800	17390.500	13209.100	405.401	57.1180	-0.2591	17459.059	68.300	4181.400	12803.699	348.283	57.377	17459.059
T80C1	767.2620	763.1270	615.5250	5.8100	4.3230	-0.0210	767.2830	4.1350	147.6020	609.7150	1.4870	4.3440	767.2830
T80C3	2129.1800	2118.6700	1646.0400	28.2190	10.1540	-0.0494	2129.2294	10.510	472.6300	1617.8210	18.0650	10.203	2129.2294
T80C5	5530.0100	5504.4200	4168.8300	100.916	22.3530	-0.1045	5530.1145	25.590	1335.590	4067.9140	78.5630	22.458	5530.1145
T80C7	10930.100	10883.700	8219.2700	233.301	39.0260	-0.1795	10930.280	46.400	2664.430	7985.9690	194.275	39.206	10930.280
T80C9	16662.400	16597.200	12630.600	385.504	55.1740	-0.2520	16662.652	65.200	3966.600	12245.096	330.330	55.426	16662.652

Source: Author (2022).

Table 28 – Pressure drop by plane of the hot branch for complete core with semicircular channels.

Test	Semicircular - Hot branch												
	$P_{h,in}$ [Pa]	$P_{h,P1}$ [Pa]	$P_{h,P2}$ [Pa]	$P_{h,P3}$ [Pa]	$P_{h,P4}$ [Pa]	$P_{h,out}$ [Pa]	ΔP_h [Pa]	in - P1	P1 - P2	P2 - P3	P3 - P4	P4 - out	ΔP_h [Pa]
T40C1	1104.6500	1099.8200	878.2750	-28.7390	4.7120	-0.0007	1104.6507	4.8300	221.5450	907.0140	-33.4510	4.7127	1104.6507
T40C3	1122.1600	1117.2700	891.6200	-29.2360	4.6520	-0.0009	1122.1609	4.8900	225.6500	920.8560	-33.8880	4.6529	1122.1609
T40C5	1127.1400	1122.2400	895.2480	-29.4070	4.7110	-0.0006	1127.1406	4.9000	226.9920	924.6550	-34.1180	4.7116	1127.1406
T40C7	1141.2900	1136.3300	906.0860	-29.7930	4.8430	-0.0007	1141.2907	4.9600	230.2440	935.8790	-34.6360	4.8437	1141.2907
T40C9	1115.5100	1110.6500	886.6650	-29.0500	4.6570	-0.0007	1115.5107	4.8600	223.9850	915.7150	-33.7070	4.6577	1115.5107
T50C1	1168.5600	1163.5100	926.8160	-30.5970	4.8480	-0.0010	1168.5610	5.0500	236.6940	957.4130	-35.4450	4.8490	1168.5610
T50C3	1136.3000	1131.3600	902.3870	-29.6620	4.8320	-0.0007	1136.3007	4.9400	228.9730	932.0490	-34.4940	4.8327	1136.3007
T50C5	1112.5700	1107.7200	884.3090	-28.9650	4.7400	-0.0007	1112.5707	4.8500	223.4110	913.2740	-33.7050	4.7407	1112.5707
T50C7	1112.2900	1107.4400	883.9520	-28.9660	4.7460	-0.0007	1112.2907	4.8500	223.4880	912.9180	-33.7120	4.7467	1112.2907
T50C9	1088.4400	1083.6800	865.9360	-28.2700	4.5750	-0.0007	1088.4407	4.7600	217.7440	894.2060	-32.8450	4.5757	1088.4407
T60C1	1226.4300	1221.1700	970.7420	-32.2590	5.0170	-0.0008	1226.4308	5.2600	250.4280	1003.0010	-37.2760	5.0178	1226.4308
T60C3	1202.1000	1196.9300	952.1140	-31.5470	5.0560	-0.0006	1202.1006	5.1700	244.8160	983.6610	-36.6030	5.0566	1202.1006
T60C5	1220.6700	1215.4400	966.1400	-32.0860	5.0180	-0.0009	1220.6709	5.2300	249.3000	998.2260	-37.1040	5.0189	1220.6709
T60C7	1216.7900	1211.5700	963.4080	-32.0250	5.1000	-0.0009	1216.7909	5.2200	248.1620	995.4330	-37.1250	5.1009	1216.7909
T60C9	1189.6800	1184.5500	942.7420	-31.2220	4.8770	-0.0008	1189.6808	5.1300	241.8080	973.9640	-36.0990	4.8778	1189.6808
T70C1	1282.1000	1276.6500	1012.6000	-33.8730	5.2400	-0.0007	1282.1007	5.4500	264.0500	1046.4730	-39.1130	5.2407	1282.1007
T70C3	1272.4400	1267.0300	1005.3000	-33.5920	5.2080	-0.0007	1272.4407	5.4100	261.7300	1038.8920	-38.8000	5.2087	1272.4407
T70C5	1268.8100	1263.4100	1002.5500	-33.4870	5.1960	-0.0007	1268.8107	5.4000	260.8600	1036.0370	-38.6830	5.1967	1268.8107
T70C7	1281.7800	1276.3300	1012.3600	-33.8630	5.2390	-0.0007	1281.7807	5.4500	263.9700	1046.2230	-39.1020	5.2397	1281.7807
T70C9	1283.3700	1277.9100	1013.5600	-33.9090	5.2440	-0.0007	1283.3707	5.4600	264.3500	1047.4690	-39.1530	5.2447	1283.3707
T80C1	1283.0500	1277.5900	1013.3200	-33.9000	5.2430	-0.0007	1283.0507	5.4600	264.2700	1047.2200	-39.1430	5.2437	1283.0507
T80C3	1279.2500	1273.8000	1010.4400	-33.7900	5.2310	-0.0007	1279.2507	5.4500	263.3600	1044.2300	-39.0210	5.2317	1279.2507
T80C5	1256.5400	1251.1800	993.2660	-33.1310	5.1550	-0.0007	1256.5407	5.3600	257.9140	1026.3970	-38.2860	5.1557	1256.5407
T80C7	1243.7000	1238.3800	983.5510	-32.7590	5.1120	-0.0007	1243.7007	5.3200	254.8290	1016.3100	-37.8710	5.1127	1243.7007
T80C9	1229.9900	1224.7200	973.1780	-32.3620	5.0650	-0.0007	1229.9907	5.2700	251.5420	1005.5400	-37.4270	5.0657	1229.9907

Source: Author (2022).

Table 29 – Pressure drop by plane of the cold branch for complete core with semicircular channels.

Test	Semicircular - Cold branch												
	$P_{c,in}$ [Pa]	$P_{c,P5}$ [Pa]	$P_{c,P6}$ [Pa]	$P_{c,P7}$ [Pa]	$P_{c,P8}$ [Pa]	$P_{c,out}$ [Pa]	ΔP_c [Pa]	in - P5	P5 - P6	P6 - P7	P7 - P8	P8 - out	ΔP_c [Pa]
T40C1	558.9710	555.2170	442.0100	6.8350	2.9910	-0.0019	558.9729	3.7540	113.2070	435.1750	3.8440	2.9929	558.9729
T40C3	1771.3100	1761.0500	1357.3500	28.1300	5.9360	-0.0040	1771.314	10.2600	403.7000	1329.220	22.1940	5.9400	1771.314
T40C5	4472.5000	4449.8300	3390.2300	82.8110	10.0080	-0.0047	4472.5047	22.6700	1059.600	3307.419	72.8030	10.0127	4472.5047
T40C7	8909.2800	8868.2100	6693.7600	184.5580	13.7030	-0.0002	8909.2802	41.0700	2174.450	6509.202	170.8550	13.7032	8909.2802
T40C9	13587.600	13528.200	10153.300	309.2870	16.6750	0.0093	13587.591	59.4000	3374.900	9844.013	292.6120	16.6657	13587.591
T50C1	539.2260	535.6250	428.6690	6.5100	2.9360	-0.0019	539.2279	3.6010	106.9560	422.1590	3.5740	2.9379	539.2279
T50C3	1566.4900	1557.3700	1208.0400	24.2710	5.5430	-0.0038	1566.4938	9.1200	349.3300	1183.7690	18.7280	5.5468	1566.4938
T50C5	4483.2700	4460.7500	3410.2000	83.2320	10.0510	-0.0048	4483.2748	22.5200	1050.550	3326.9680	73.1810	10.0558	4483.2748
T50C7	8829.1600	8788.6900	6655.8500	182.7620	13.6950	-0.0007	8829.1607	40.4700	2132.840	6473.0880	169.0670	13.6957	8829.1607
T50C9	13977.700	13917.200	10473.700	320.6190	16.9660	0.0096	13977.691	60.5000	3443.500	10153.081	303.6530	16.9564	13977.691
T60C1	560.6200	556.9600	447.3900	6.8490	3.0300	-0.0020	560.6220	3.6600	109.5700	440.5410	3.8190	3.0320	560.6220
T60C3	1586.4100	1577.3200	1229.0600	24.7060	5.5970	-0.0039	1586.4139	9.0900	348.2600	1204.3540	19.1090	5.6009	1586.4139
T60C5	4498.4000	4476.0800	3436.4000	83.8670	10.0600	-0.0050	4498.4050	22.3200	1039.6800	3352.5330	73.8070	10.0650	4498.4050
T60C7	8423.0200	8384.6100	6380.9500	173.2670	13.3600	-0.0016	8423.0216	38.4100	2003.6600	6207.6830	159.9070	13.3616	8423.0216
T60C9	14298.200	14237.100	10754.400	330.5830	17.0440	0.0098	14298.190	61.1000	3482.700	10423.817	313.5390	17.0342	14298.190
T70C1	599.6370	595.8120	479.5440	7.4680	3.1890	-0.0021	599.6391	3.8250	116.2680	472.0760	4.2790	3.1911	599.6391
T70C3	1752.2300	1742.4400	1360.7500	27.9230	5.9540	-0.0042	1752.2342	9.7900	381.6900	1332.8270	21.9690	5.9582	1752.2342
T70C5	3930.4300	3910.7700	3018.6800	72.1810	9.4130	-0.0052	3930.4352	19.6600	892.0900	2946.4990	62.7680	9.4182	3930.4352
T70C7	8841.7400	8802.1300	6721.9400	184.1150	13.5470	-0.0011	8841.7411	39.6100	2080.190	6537.8250	170.5680	13.5481	8841.7411
T70C9	14566.200	14504.800	10998.100	339.2000	17.0480	0.0098	14566.191	61.4000	3506.700	10658.900	322.1520	17.0382	14566.191
T80C1	624.0740	620.1630	500.4060	7.8530	3.2940	-0.0022	624.0762	3.9110	119.7570	492.5530	4.5590	3.2962	624.0762
T80C3	1799.3700	1789.4700	1402.3900	28.8850	6.0680	-0.0043	1799.3743	9.9000	387.0800	1373.5050	22.8170	6.0723	1799.3743
T80C5	4862.3800	4839.0500	3741.1700	92.3180	10.4160	-0.0051	4862.3851	23.3300	1097.880	3648.8520	81.9020	10.4211	4862.3851
T80C7	9462.6900	9421.1500	7216.5700	200.2560	13.8250	-0.0004	9462.6904	41.5400	2204.580	7016.3140	186.4310	13.8254	9462.6904
T80C9	13979.300	13920.700	10600.700	322.8980	16.5010	0.0082	13979.292	58.6000	3320.000	10277.802	306.3970	16.4928	13979.292

Source: Author (2022).